A Study of Passive Scalar Mixing in Turbulent Boundary Layers using Multipoint Correlators

A Thesis
Presented to
The Academic Faculty

by

Ronald J. Miller

In Partial Fulfillment
of the Requirements for the Degree
Master of Science in
Civil and Environmental Engineering

School of Civil and Environmental Engineering
Georgia Institute of Technology
December 2005

A Study of Passive Scalar Mixing in Turbulent Boundary Layers using Multipoint Correlators

Approved by:

Dr. Donald R. Webster, Advisor
School of Civil and Environmental Engineering
Georgia Institute of Technology

Dr. Philip J. W. Roberts
School of Civil and Environmental Engineering
Georgia Institute of Technology

Dr. Terry W. Sturm
School of Civil and Environmental Engineering
Georgia Institute of Technology

Date Approved: 28 November 2005

ACKNOWLEDGEMENTS

I would like to thank my advisor, Dr. Donald R. Webster, for this opportunity. His suggestions and guidance has provided a learning experience that will serve me well throughout my career. I sincerely appreciate the comments provided by my committee members, Dr. Philip J. W. Roberts and Dr. Terry W. Sturm. I would like to thank L. Prasad Dasi for initial technical support and the data collection. I would also like to thankfully acknowledge the financial support provided by the National Science Foundation.

For personal support, I would like to thank my wife, Gabrielle. I am eternally grateful for her constant support and understanding throughout all my new ventures. I would also like to thank fellow graduate students in the EFM&WR program for always giving me a good laugh.

TABLE OF CONTENTS

LIST OF TABLES

LIST OF FIGURES

LIST OF VARIABLES

A_n	Mean velocity profile constant in a turbulent boundary layer.
C_N	Scalar field correlation function of N instantaneous measurement points.
C_n	Universal constant in the n^{th} order velocity structure function.
χ	Scalar variance dissipation rate.
χ_r	Local average scalar variance dissipation rate.
D	Nozzle diameter, injection length scale.
d	Pipe diameter, separation distance of the points describing the three-point configuration.
δ	Boundary layer thickness.
δ_ν	Viscous length scale.
ε	Kinetic energy dissipation rate.
ε_r	Local average kinetic energy dissipation rate.
ε_T	Turbulent diffusion coefficient.
η	Kolmogorov length scale.
η_B	Batchelor length scale.
η_{oc}	Obukhov-Corrsin length scale.
$f(\chi, w)$	Shape factor of the three-point correlation function.
H	Uniform open channel flow depth.
H_N	Hopf operator.
H_n	Universal constant in the n^{th} order scalar structure function.
κ	Molecular diffusivity of the passive scalar; von Karman's constant.
l_L	Integral length scale.
$\dot{m}$	Passive scalar mass flowrate.
n	Order of the structure function, number of scalar field measurements throughout time and space.
N	Number of instantaneous images captured of the fluctuating scaling field.
ν	Kinematic viscosity.
P	Instantaneous pressure, Probability.

φ	Orientation angle of the three-point configuration with respect to the mean scalar gradient.
Π	Wake strength parameter.
R	Global size variable of the three-point configuration.
r	Magnitude of the separation vector between points.
Re	Reynolds number.
ρ	Fluid density.
S	Sample space variable corresponding to Θ, structure function.
s	Standard deviation of the three-point correlation function.
s_e	Standard error of the three-point correlation function.
Sc	Schmidt number.
t	Time.
τ_k	Kolmogorov time scale.
$\tau(l)$	Inertial subrange time scale.
τ_w	Wall shear stress.
Θ	Instantaneous concentration.
$\langle\Theta\rangle$	Average concentration.
θ	Instantaneous concentration fluctuation.
$\langle\Delta\theta_r^n\rangle$	Passive scalar structure function.
$\tilde{\theta}$	Standard deviation of the scalar fluctuations.
$\langle\theta^2\rangle$	Variance of the scalar fluctuations.
U	Instantaneous velocity.
$\langle U\rangle$	Average velocity.
U_∞	Free stream velocity.
u_k	Kolmogorov velocity scale.
$u(l)$	Inertial subrange velocity scale.
u	Instantaneous velocity fluctuation.
u^+	Mean velocity normalized by wall shear velocity.
$\langle\Delta u_r^n\rangle$	Velocity structure function.
$\tilde{u}$	Standard deviation of the velocity fluctuations.

u_*	Wall shear velocity.
$w\left(\frac{y}{\delta}\right)$	Wake function.
x	Streamwise coordinate direction.
Y	Separation distance for the three-point correlation function.
y^+	Wall-normal displacement normalized by the viscous length scale.
y	Wall-normal coordinate direction.
z	Transverse coordinate direction.
ζ_3	Scaling exponent of the global size variable.

SUMMARY

This study analyzes a turbulent passive scalar field using two-point and three-point correlations of the fluctuating scalar field. Multipoint correlation functions are investigated because they retain scaling property information and simultaneously probe the concentration field for the spatial structure of the scalar filaments. Thus, multipoint correlation functions provide unique information about the spatial properties of the concentration filaments. The concentration field is created by the iso-kinetic release of a high Schmidt number dye into a fully developed turbulent boundary layer of an open channel flow. The concentration fields were previously measured using the planar laser-induced fluorescence technique.

The two-point correlations of the fluctuating scalar field indicate that as the scalar field evolves downstream, the anisotropic influence of the tracer injection method diminishes, and the scalar field becomes dominated by the mean velocity shear. As the scalar filaments align with the mean velocity gradient, the elliptical shape associated with the contours of the correlation function tilts in the direction of the mean velocity gradient. As a result, the two-point correlation contours of the concentration fluctuations indicate that anisotropic conditions (i.e. the tilted, asymmetric, elliptical shape) develop as a consequence of the mean velocity shear.

Three-point correlations of the fluctuating scalar field are calculated based on configuration geometries defined by previous researchers. The first configuration follows Mydlarski & Warhaft (1998), which employs two cold-wire measurements and Taylor's frozen turbulence hypothesis. The three-point correlation contours of the concentration fluctuations associated with the cold-wire measurements exhibit a symmetric characteristic V-shape. Similar symmetric properties are observed in the current study. The symmetry associated with well-correlated points is represented by concentric, circular contours, which indicates universal

behavior of the fluctuating scalar field for these points. The contours with smaller values retain symmetric properties but develop a concave-sided hexagonal shape that resembles the characteristic V-shape reported in previous research. The second set of configurations follows on recent theoretical predictions, which indicate that the three-point correlation of the fluctuating scalar field is dependent on the size, shape, and orientation of the triangle created by the three points. The current study analyzes two geometric configurations (isosceles and collinear). The geometric configurations are defined to ensure that the influence of the shape remains constant as the configuration is rotated, translated, and dilated. As the isosceles configuration is rotated, the value of the three-point correlation function remains unchanged. However, as the collinear configuration is rotated, the three-point correlation function varies. Therefore, the influence of the orientation angle between the three-point configuration and the mean concentration gradient varies depending on the specified geometry. Additionally, the scaling exponent in the inertial-convective regime is calculated to determine the dependence of the correlation function on the size of the triangle pattern. The scaling exponent remains independent of the orientation angle between the three-point configuration and the mean concentration gradient. At intermediate downstream distances, the scaling exponent appears dependent on the injection length scale and independent of the Reynolds number.

CHAPTER I

INTRODUCTION

Turbulent mixing occurs in many engineering applications as well as the natural environment. In many cases, the mixed scalar quantity is passive, which means the scalar has no effect on the velocity field. Typical examples include pollutant discharge in natural waters (or air), transport of chemicals sensed by foraging organisms, and fuel injection into a combustion engine. In each case, the ability to predict local peak concentration levels is of primary importance in order to avoid hazardous conditions, sense prey, or optimize efficiency. Previous research has provided a framework to predict the average downstream concentration values based on models such as eddy diffusivity. However, the rapid mixing rate associated with turbulent flows can lead to concentration fluctuations that are significantly greater than the predicted average. Turbulent eddies stretch and fold the scalar field, which results in large fluctuations in the value of the scalar quantity. The large fluctuations randomly occur in spatio-temporal bursts and consequently are described as intermittent. The intermittency makes the scalar fields difficult to predict, or even describe. Multipoint correlations of the fluctuating scalar field have recently been investigated in hopes that their behavior provides insight into the intermittent behavior of the turbulent passive scalar field.

In the current study, the turbulent passive scalar field was developed through the isokinetic point release of a high Schmidt number dye ($Sc \simeq 1000$) into the inertial layer of a fully developed open channel turbulent boundary layer. Images of the instantaneous concentration field were captured using planar laser-induced fluorescence (PLIF). Data were collected for three Reynolds numbers (Re = 5000, 10000, and 20000) and three nozzle diameters ($D = 2.2\ mm$, $4.7\ mm$, and $9.4\ mm$). Figure 1.1 provides a sample visualization of the passive scalar field mixing in the open channel turbulent boundary layer for Re = 10000 and $D = 4.7\ mm$.

Turbulent flows are notoriously difficult to describe and predict, but some fundamental

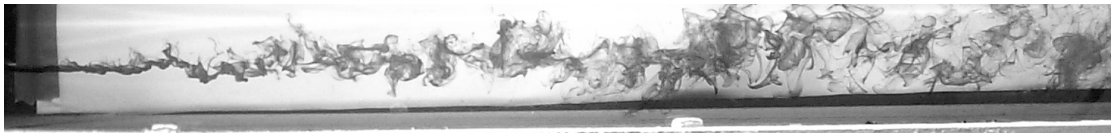

Figure 1.1: Flow visualization image of the turbulent passive scalar field in the fully developed open channel turbulent boundary layer (Dasi, 2004).

advances have been made. Kolmogorov (1941) used Richardson's (1922) concept of the energy cascade to develop a phenomenological model that examines the small-scale behavior of the turbulent velocity field (K41 theory). Obukhov (1949) and Corrsin (1951) applied this phenomenological model to the passive scalar field (KOC argument). The model is based on the assumption that isotropic conditions exist at the smallest scales of any turbulent flow field. The assumption of local (i.e. small-scale) isotropy leads to dimensional arguments that dictate specific functional forms of the velocity and passive scalar structure functions. The functional form requires that the value of each structure function should be proportional to $r^{n/3}$ (where r describes the distance between the measurement points and n indicates the order of the statistics). Note that this functional form is valid only for r in the inertial range for the velocity field and r in the inertial-convective regime for the passive scalar field. Subsequent experimental results of higher order statistics ($n \geq 3$) indicates that the scaling exponent, $n/3$, does not follow the phenomenological predictions. Thus, the anomalous behavior of the scaling exponent indicates that the assumption of local isotropy is violated at the smallest scales.

Therefore, if the scaling exponent does not follow phenomenological predictions, is there a universal value? If so, what is the value? If not, what is the behavior of the scaling exponent? The lack of validation of the KOC argument has encouraged researchers to examine alternative perspectives in order to better understand the possible universal characteristics of turbulent passive scalar fields. Traditionally, research efforts focused on measurements

at one or two points in space and the independent visual identification of scalar filaments. The analysis of multipoint correlations of the fluctuating scalar field has become one avenue of investigation. The multipoint correlation function measures the correlation of the instantaneous concentration fluctuations at several points in space. The advantage of multipoint correlators is that they probe the scalar field for the spatial orientation of scalar filaments and simultaneously retain scaling exponent properties, in analogy with the structure functions described above. Figure 1.2 illustrates a three-point configuration on a turbulent passive scalar field. Note that points A, B, and C allow probing for the spatial orientation of the scalar filaments (i.e. the identification of spatial structures). Therefore, multipoint correlators naturally extend previous research methods and provide a framework to examine the intermittent behavior associated with the scalar field.

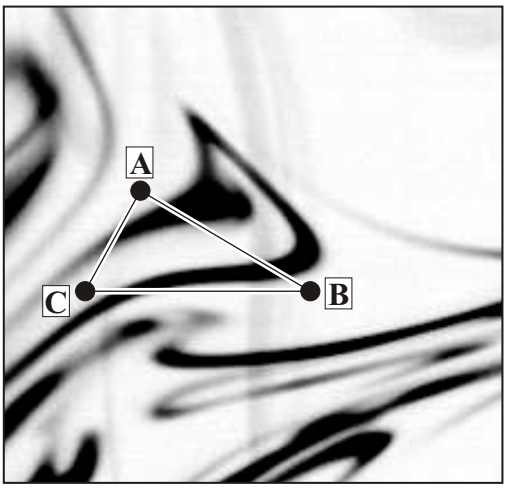

Figure 1.2: The three-point correlation compares the concentration fluctuations and reveals the spatial orientation of the scalar filaments relative to the geometry and orientation of the points.

The purpose of this study is to employ multipoint correlation functions to examine the

small-scale behavior of the passive scalar field in a turbulent boundary layer (shear flow). To date, the Mydlarski & Warhaft (1998) study (non-shear flow) is the only experimental data that has been reported for multipoint correlation functions to complement the theoretical efforts of Shraiman & Siggia (1996) and others. The two-point correlations of the fluctuating scalar field are analyzed to estimate the scalar filament size and develop a contour map of the fluctuating scalar field. The three-point correlation functions of the fluctuating scalar field are examined to determine the scaling exponent properties, extract geometric relationships of the scalar filaments, and evaluate the small-scale structure of the concentration field. Chapter 2 reviews the classical turbulence theory associated with the passive scalar field. In addition, new theoretical predictions (Shraiman & Siggia, 1996, 2000), as well as current experimental results (Mydlarski & Warhaft, 1998), are included to explain the impetus for the current study. Chapter 3 briefly describes the experimental facility and outlines the methods used to analyze the turbulent passive scalar field. Chapter 4 contains the experimental results. Chapter 5 summarizes the pertinent results and discusses additional avenues of investigation.

CHAPTER II

LITERATURE REVIEW

2.1 Turbulent Flows

2.1.1 Flow Classification

In 1883, Osborne Reynolds collected experimental data that provided a framework to differentiate laminar flow and turbulent flow. The experiment consisted of injecting a neutrally buoyant dye into a smooth, horizontal pipe. For low flowrates, the dye streakline remained well defined and smooth, which is described as laminar. As the flowrate increased, the dye streakline began to exhibit intermittent behavior characterized by fluctuations in time and space. Due to the intermittent fluctuations, this flow was described as transitional (i.e. a state between laminar and turbulent). Once the flowrate exceeded a certain value, the dye streakline was rapidly mixed throughout the pipe cross-section in a random manner. This observed flow is classified as turbulent flow. Reynolds determined that the transition from laminar flow to turbulent flow occurred at a critical value of the parameter that is now referred to as the Reynolds number. The Reynolds number is defined as $Re = \langle U \rangle d/\nu$, where $\langle U \rangle$ is the average cross-sectional velocity, d is the pipe diameter, and ν is the kinematic viscosity of the fluid. The Reynolds number describes the ratio of inertial forces to viscous forces. Accordingly, laminar flow occurs when the viscous forces are dominant and turbulent flow occurs when the inertial forces are dominant. Most flows that occur in nature and engineering applications are classified as turbulent. As a result, research efforts have focused on predicting turbulent flow behavior.

Although the Reynolds number provides a quantitative parameter for flow classification, the transition from laminar to turbulent does not always occur exactly at the predicted Reynolds number. As a result, characterizations are used in conjunction with the Reynolds number for flow classification. Laminar flow is characterized as a smooth, quiescent flow.

Passive scalar mixing in laminar flow occurs exclusively through molecular diffusion. Although turbulent flow eludes a precise definition, several characteristics describe turbulent motions including:

- Unpredictability: Turbulent flows are random and chaotic.
- Nonlinearity: The nonlinear terms in the governing Navier Stokes equations lead to vortex stretching and the production of turbulence.
- Diffusivity: Mixing in turbulent flows occurs on a macroscopic level as well as the molecular level. Accordingly, there is a rapid diffusion rate associated with turbulence.
- Vorticity: Turbulent flows contain fluctuating vortex structures called eddies. The size of these structures range from the order of the flow size (large structures) to the size of the dissipating eddies (small structures). As a result, there is a large continuous range of structure sizes that exist in turbulent flows.
- Dissipation: Turbulent flows produce increasingly larger gradients of velocity that are eventually dissipated by viscosity. Therefore, all turbulent flows are dissipative. As a result of the dissipative property, energy must be continuously supplied to maintain turbulence. The energy supply is provided by the large-scale flow and eddy structures.

2.1.2 Turbulent Boundary Layers

Transport and mixing of the passive scalar field for the present study occurs in a turbulent boundary layer over a smooth surface. The boundary layer is comprised of an inner region and an outer region, each of which exhibit unique characteristics of the mean velocity field. Therefore, an understanding of the velocity field in each region is required to examine the passive scalar field.

The inner region extends from $y/\delta = 0$ to roughly $y/\delta = 0.1$ (where y describes the distance from the wall surface and δ represents the boundary layer thickness). This region is divided into several distinct layers including the viscous sublayer, the buffer zone, and the logarithmic overlap layer. The shear stress at the wall dictates the flow characteristics

in the inner region. The viscous effects associated with the presence of the wall can be described in terms of a characteristic velocity scale called the wall shear velocity:

$$u_* = \sqrt{\frac{\tau_w}{\rho}} \tag{2.1}$$

where τ_w is the wall shear stress. Furthermore, the wall shear velocity can be used to define a characteristic length scale called the viscous length scale:

$$\delta_\nu = \frac{\nu}{u_*} \tag{2.2}$$

The mean velocity, $\langle U \rangle$, and the distance from the wall surface, y, can be normalized by the wall shear velocity and the viscous length scale, respectively. These non-dimensional terms are called wall units and are typically denoted u^+ and y^+:

$$u^+ = \frac{\langle U \rangle}{u_*} \qquad \text{and} \qquad y^+ = \frac{u_* y}{\nu} \tag{2.3}$$

Due to the influence of the wall, the components of the mean velocity profile in the inner region are called the *law of the wall*.

The viscous sublayer is a thin region that extends from the wall surface to $y^+ \simeq 5$. Due to the close proximity of the wall, the turbulent fluctuations are dampened by viscosity. Therefore, the flow in the viscous sublayer is considered laminar. As a result, the shear stress is constant, and the mean velocity profile is represented by the linear equation:

$$u^+ = y^+ \tag{2.4}$$

The buffer zone is located above the viscous sublayer and extends to approximately $y^+ \simeq 30$. The buffer zone joins the viscous flow regime to the turbulent flow regime. Large velocity gradients exist in this layer; therefore, turbulence production reaches a maximum value. The mean velocity profile is characterized by an asymptotic approach to the profile in the logarithmic overlap layer.

The logarithmic overlap layer extends from approximately $y^+ \simeq 30$ to $y/\delta \simeq 0.2$ (note that the logarithmic overlap layer is also referred to as the inertial layer). Therefore, the overlap layer begins in the inner region and terminates in the outer region. The overlap layer contained in the inner region is characterized by combined viscous and turbulent shear

stresses. Prandtl's research on turbulent boundary layers and von Karman's similarity hypothesis for turbulence led to the following definition of the mean velocity profile in the inner region:

$$u^+ = \frac{1}{\kappa} \ln\left(y^+\right) + A_1 \tag{2.5}$$

where von Karman's constant is $\kappa = 0.41$ and $A_1 = 5.2$. Equation 2.5 incorporates the viscous shear stress associated with the wall and the turbulent shear stress associated with the free stream flow. Thus, the *law of the wall* defined by equation 2.5 completely describes the mean velocity profile in the inner region.

The outer region extends from $y^+ \simeq 50$ to $y/\delta = 1$ and consists of the logarithmic overlap layer and the defect layer. As the distance from the wall increases, the viscous effects diminish and the turbulent stresses dominate. The turbulent stresses lead to a drag on the free stream flow that results in a velocity defect. Therefore, it is appropriate to redefine equation 2.5 in terms of the velocity defect. In addition, the distance from the wall is normalized using the boundary layer thickness. The resulting equation is called the *velocity defect law*:

$$\frac{U_\infty - \langle U \rangle}{u_*} = -\frac{1}{\kappa} \ln\left(\frac{y}{\delta}\right) + A_2 \tag{2.6}$$

where A_2 is a flow dependent constant and U_∞ is the free stream velocity of the flow. Equations 2.5 and 2.6 apply equally for the interval $\delta_\nu \ll y \ll \delta$.

The defect layer is located above the logarithmic overlap region and extends from $y/\delta \simeq 0.2$ to $y/\delta = 1$. The mean velocity profile in the defect layer deviates from the logarithmic predictions in equation 2.6. Coles (1956) derived the mean velocity profile throughout the entire boundary layer by analyzing existing data. Coles (1956) illustrated that the mean velocity profile can be represented by combining the *law of the wall* and the *law of the wake*. Thus, the velocity defect law is transformed to:

$$\frac{U_\infty - \langle U \rangle}{u_*} = \frac{1}{\kappa} \left\{ -\ln\left(\frac{y}{\delta}\right) + \Pi \left[2 - w\left(\frac{y}{\delta}\right)\right] \right\} \tag{2.7}$$

where Π is a flow dependent variable called the *wake strength parameter*, and $w(y/\delta)$ is the *wake function*. Analysis of experimental data results in the following approximation for the

wake function:

$$w\left(\frac{y}{\delta}\right) = 2\sin^2\left(\frac{\pi}{2}\frac{y}{\delta}\right) \tag{2.8}$$

The velocity defect law represented by equation 2.7 is valid for $y^+ \simeq 50$ to $y/\delta = 1$, which describes the mean velocity profile of almost the entire turbulent boundary layer. The profiles of the mean velocity distribution in a turbulent boundary layer are summarized in Figure 2.1.

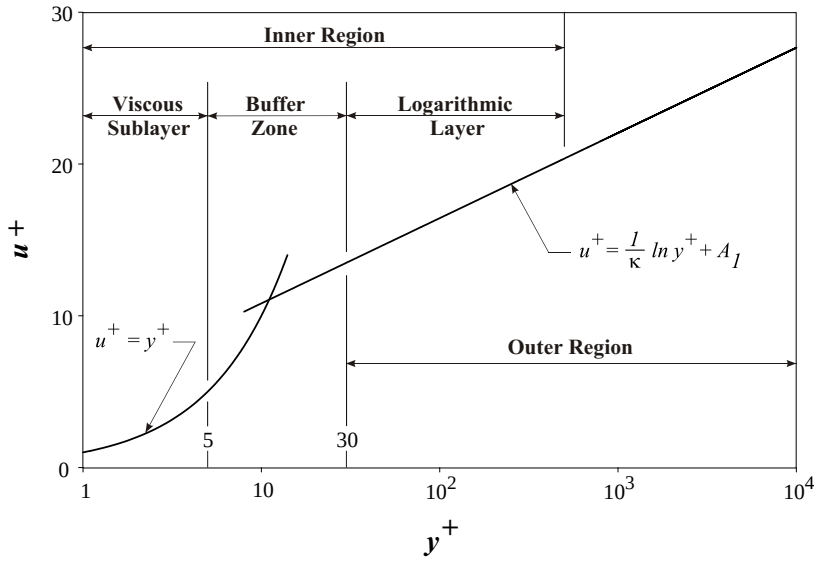

Figure 2.1: The mean velocity profile for a turbulent boundary layer plotted in terms of inner variables.

2.1.3 Statistical Description of Turbulent Flows

Classical fluid mechanic theory provides equations that govern laminar and turbulent flows. Solving the governing equations for given boundary conditions provides deterministic fields for each flow variable. The flow field variables include the velocity field, $U_i(x_i, t)$, the pressure field, $P(x_i, t)$, and the passive concentration field, $\Theta(x_i, t)$. Neglecting body forces, for an incompressible fluid with constant density and kinematic viscosity, the governing

equations are defined as:

$$\frac{\partial U_i}{\partial x_i} = 0 \tag{2.9}$$

$$\frac{DU_i}{Dt} = -\frac{1}{\rho}\frac{\partial P}{\partial x_i} + \nu\frac{\partial^2 U_i}{\partial x_j \partial x_j} \tag{2.10}$$

$$\frac{D\Theta}{Dt} = \kappa\frac{\partial^2 \Theta}{\partial x_j \partial x_j} \tag{2.11}$$

where κ is the molecular diffusion coefficient of the scalar quantity in the surrounding media. Although equations 2.9, 2.10 and 2.11 govern any flow, unpredictable solutions occur for turbulent flows. Turbulent flow solutions are inherently random and not deterministic. The unpredictability associated with turbulent flows exists because turbulent flows are hypersensitive to perturbations. Perturbations, or minute disturbances, exist in every flow and cannot be completely removed from the system. The disturbances can be a result of boundary conditions, initial conditions, or fluid inhomogeneities. Although the perturbations also exist in laminar flow, the laminar flow solutions are predictable because the flow is not sensitive to the disturbances. The hypersensitivity of turbulent flows to perturbations is exhibited by the inherent randomness of the solutions.

2.1.3.1 Random Variables

The unpredictable nature of turbulent flow requires that the instantaneous flow variables are analyzed as random variables. Therefore, in order to obtain a quantitative analysis of the turbulent flow field, statistical methods must be used. The theory required to analyze random variables will be developed in the context of the instantaneous concentration, Θ, because the present study focuses on a passive scalar field. The continuous set of all possible concentration values is called the sample space, S. Due to the random nature of Θ, developing a method to estimate an exact concentration value within the sample space is impossible. However, it is feasible to develop techniques to assess a range of possible concentration values. Assuming that the range of values is contained within S, a subset of the sample space can be defined. If the subset contains an upper limit, S_U, and a lower

limit, S_L, then a subset, S_S, can be defined as follows:

$$S_S = \{S_L \leq \Theta \leq S_U\} \tag{2.12}$$

The probability that the concentration value is contained within S_S is mathematically described as:

$$P\{S_S\} = P\{S_L \leq \Theta \leq S_U\} = \int_{S_L}^{S_U} f(S)dS \tag{2.13}$$

where $f(S)$ is a continuous function called the probability density function (PDF). The PDF completely describes the random variable, Θ.

If the PDF of Θ is known, then subsequent statistical parameters of the random variable can be defined. The expected value (or mean value) of Θ is defined as:

$$\langle\Theta\rangle = \int_{-\infty}^{+\infty} Sf(S)dS \tag{2.14}$$

For turbulent flows, Reynolds introduced a decomposition to define the instantaneous concentration as the summation of the mean value and the fluctuating component. Using Reynolds decomposition, the instantaneous concentration can be represented by:

$$\Theta = \langle\Theta\rangle + \theta \tag{2.15}$$

Additional statistical parameters include the variance and the standard deviation. The variance of the scalar fluctuations provides a measure of the departure from the expected concentration value and is mathematically described as:

$$var(\Theta) = \langle\theta^2\rangle = \int_{-\infty}^{+\infty} (S - \langle\Theta\rangle)^2 f(S)dS \tag{2.16}$$

The standard deviation of the scalar fluctuations is the square root of the variance:

$$sdev(\Theta) = \tilde{\theta} = \langle\theta^2\rangle^{1/2} \tag{2.17}$$

For notational convenience, the standard deviation of the scalar fluctuations is denoted $\tilde{\theta}$.

2.1.3.2 Random Fields

In addition to the random behavior, Θ is also a function of space and time, i.e. $\Theta = \Theta(x_i, t)$ (where the subscript i takes on a value of 1, 2, or 3 to represent the streamwise,

wall-normal, and transverse directions, respectively). For this reason, the instantaneous concentration is more precisely classified as a random field. The statistical parameters defined in equations 2.14, 2.16 and 2.17 are also valid for $\Theta(x_i, t)$. Analogous to equation 2.15, the instantaneous concentration field can be defined using Reynolds decomposition:

$$\Theta(x_i, t) = \langle \Theta(x_i, t) \rangle + \theta(x_i, t) \tag{2.18}$$

In order to completely characterize the random concentration field, the PDF of Θ is required at all points in space for each instant in time (i.e. a joint PDF of the random field, $\Theta(x_i, t)$, must be known). However, simplifications can be made if the concentration field is statistically stationary, statistically homogeneous, or isotropic. Statistically stationary means that the concentration field statistics (e.g. $\langle \Theta(x_i, t) \rangle$, $\langle [\theta(x_i, t)]^2 \rangle$, and $\tilde{\theta}(x_i, t)$) remain constant with respect to time. Statistically homogeneous implies that the field statistics are independent of coordinate system translations. If the statistics are independent of coordinate system rotations as well as translations, then the concentration field is isotropic. Therefore, if the field is statistically independent of space and time, then a joint PDF is required only for one arbitrary point in space at any instant in time. Due to the statistical independence, this joint PDF applies to all points in space for each instant in time.

However, the field statistics associated with turbulent flows are rarely independent of *both* space and time. Recent research indicates that the scalar field is fundamentally anisotropic, even in the presence of an isotropic velocity field (Holzer & Siggia, 1994). Additionally, the scalar field in a turbulent boundary layer is statistically stationary but not statistically homogeneous (i.e. $\langle \Theta(x_i) \rangle$, $\langle [\theta(x_i)]^2 \rangle$, $\tilde{\theta}(x_i)$) (Rahman & Webster, 2005). In general, a joint PDF for a random field requires a large amount of detailed information that is impossible to ascertain for a turbulent flow field. Thus, obtaining a joint PDF is not a tractable method of analyzing the random concentration field.

2.1.3.3 Ensemble Average

The ensemble average can be used to develop the statistics necessary to analyze the scalar field in the absence of the joint PDF. This process requires N independent repeated measurements obtained under the same conditions. Recognizing that the scalar field is

statistically stationary in a turbulent boundary layer, it is possible to redefine equations 2.14, 2.16 and 2.17 in terms of an ensemble average. The resulting equations for the average concentration field, the variance of the scalar fluctuations, and the standard deviation of the scalar fluctuations are illustrated in equations 2.19, 2.20, and 2.21, respectively.

$$\langle \Theta(x_i) \rangle = \frac{1}{N} \sum_{n=1}^{N} \Theta^n(x_i, t) \tag{2.19}$$

$$var(\Theta(x_i)) = \frac{1}{N} \sum_{n=1}^{N} [\Theta^n(x_i, t) - \langle \Theta(x_i) \rangle]^2 = \langle [\theta(x_i)]^2 \rangle \tag{2.20}$$

$$sdev(\Theta(x_i)) = \langle [\theta(x_i)]^2 \rangle^{1/2} = \tilde{\theta}(x_i) \tag{2.21}$$

where $\Theta^n(x_i, t)$ represents the n^{th} instantaneous measurement at the x_i position. The ensemble average equations explicitly denote the variable dependence on space and time. Future references will omit the dependence notation for convenience. However, it is implicitly assumed that variables describing the velocity and scalar fields are functions of space and time.

A final definition regarding ensemble averages is the standard deviation of the velocity fluctuations. This definition is necessary to examine the similarity hypotheses developed by Kolmogorov. These hypotheses form the foundation to evaluate the small-scale behavior of turbulent flows. The standard deviation of the velocity fluctuations is defined as:

$$sdev(U) = \sqrt{\frac{1}{N} \sum_{n=1}^{N} [U^n - \langle U \rangle]^2} = \tilde{u} \tag{2.22}$$

2.1.4 Small-Scale Behavior of Turbulent Flows

Kolmogorov (1941) developed a phenomenological model to examine the small-scale motions in turbulent flows (this model is commonly referred to as the K41 theory, which stands for Kolmogorov 1941). The model is based on Richardson's description of the energy cascade, which states that kinetic energy is transferred from the largest eddies to the smallest eddies (Richardson, 1922). The implication is that all the energy is initially contained in the largest eddies and the smallest eddies dissipate the energy to heat. The rate at which

energy is transferred from the largest eddies is proportional to the kinetic energy of the large-scale turbulence ($\sim \tilde{u}^2$) divided by the turnover time of the largest eddies ($l_L/\tilde{u}$). The resulting energy dissipation rate, ε, is therefore approximately estimated by:

$$\varepsilon \sim \frac{\tilde{u}^3}{l_L} \tag{2.23}$$

where $\tilde{u}$ is the standard deviation of the velocity fluctuations, and l_L is the size of the largest eddies. However, Richardson's description of the energy cascade model remains incomplete. For example, the model does not indicate the size of the dissipating eddies or a method to evaluate the functional behavior of the velocity and time scales. K41 theory is comprised of three hypotheses to address these limitations. The three hypotheses include the hypothesis of local isotropy, the first similarity hypothesis, and the second similarity hypothesis. The hypothesis of local isotropy states that isotropy exists at the smallest scales of all turbulent flows if the Reynolds number is "sufficiently high". Isotropic behavior implies that the small-scale statistics are universal in all turbulent flows. This universality leads to the first similarity hypothesis, which states that ε and ν are the only variables responsible for the statistical similarity of the small-scale motions in all turbulent flows that have a "sufficiently high" Reynolds number. Since the small-scale motions are only dependent on ε and ν, dimensional arguments suggest the following definitions:

$$\eta \sim \left(\frac{\nu^3}{\varepsilon}\right)^{1/4} \tag{2.24}$$

$$u_k \sim (\varepsilon\nu)^{1/4} \tag{2.25}$$

$$\tau_k \sim \left(\frac{\nu}{\varepsilon}\right)^{1/2} \tag{2.26}$$

Equations 2.24, 2.25, and 2.26, respectively, represent the length scale, velocity scale, and time scale of the smallest motions in any turbulent flow. Collectively, these equations are referred to as the Kolmogorov scales.

A consequence of the "sufficiently high" Reynolds number criterion is the existence of an intermediate eddy structure size, l, that is significantly larger than the smallest eddies and significantly smaller than the largest eddies ($l_L \gg l \gg \eta$). The result is a range of

eddy sizes called the inertial subrange. Eddies within the inertial subrange are responsible for the transfer of energy from the largest to the smallest scales but remain independent of viscosity. Therefore, the second similarity hypothesis states that ε is the only variable responsible for the statistical similarity of the motions within the inertial subrange. Thus, for a given length scale, l, within the inertial subrange, the velocity and time scales can be defined:

$$u(l) \sim (\varepsilon l)^{1/3} \tag{2.27}$$

$$\tau(l) \sim \left(\frac{l^2}{\varepsilon}\right)^{1/3} \tag{2.28}$$

The implications of the hypotheses formulated by Kolmogorov (1941) extend beyond defining the dissipating scales and the functional dependence of the velocity and time scales. These hypotheses also lead to specific scaling behavior associated with velocity structure functions.

2.1.4.1 Velocity Structure Functions

Additional consequences of the K41 theory can be observed by analyzing the velocity structure functions. In mathematical terms, the velocity structure functions are defined as:

$$\langle \Delta u_r^n \rangle = \langle [u(x+r,t) - u(x,t)]^n \rangle \tag{2.29}$$

Equation 2.29 provides an additional measure of the small-scale universality. K41 theory predicts that Δu_r^n is a function of only ε and r (for r in the inertial subrange). Therefore, dimensional analysis dictates the following functional form:

$$\langle \Delta u_r^n \rangle = C_n (\varepsilon r)^{n/3} \tag{2.30}$$

where C_n are universal constants. Experimental data collected by Anselmet et al. (1984) illustrates that for higher order statistics ($n \geq 3$) the experimental results do not agree with the K41 predictions. The anomalous scaling is a result of the fluctuating intermittent dissipation rate. In order to account for the anomalous scaling, Kolmogorov (1962) and Obukhov (1962) independently developed the refined similarity hypotheses (RSH). The RSH continues to assume local isotropic behavior and universality at the small scales. However, the

RSH established a local average dissipation rate, ε_r, to account for the spatial intermittency. Thus, in the spirit of the first similarity hypothesis, the statistics in the dissipative range are functions of only ε_r and ν. Similarly, the second similarity hypothesis predicts that the statistics in the inertial subrange are functions of only ε_r. The RSH captures the velocity structure function behavior better than K41 theory. However, anomalous scaling is still observed for the higher-order statistics. The anomalous behavior leads to the accepted belief that real turbulence is not locally isotropic (i.e. the anisotropic conditions persist to the smallest scales of any turbulent flow). Therefore, the fundamental assumption associated with the K41 theory and the RSH is inconsistent.

2.2 Passive Scalar Mixing

2.2.1 Conservative Passive Scalar Mixing

2.2.1.1 Turbulent Scalar Advective-Diffusion Equation

Homogenization of the scalar field is achieved much more rapidly in a turbulent flow than in a laminar flow. The rapid blending rate associated with a turbulent flow field can be explained by establishing specific definitions for the terms *mixing* and *stirring*. *Stirring* is the process that refers to the stretching and folding of the passive scalar field. *Mixing* involves stirring in addition to molecular diffusion. These processes work together to create a homogeneous scalar field. *Stirring* produces large gradients that facilitate the molecular diffusion process.

The turbulent scalar advective-diffusion equation can be derived by substituting the Reynolds decomposition of the concentration field and velocity field (i.e. $\Theta = \langle\Theta\rangle + \theta$, $U = \langle U\rangle + u$) into equation 2.11. Assuming that the molecular diffusion coefficient is constant in space, the resulting equation for the mean concentration is:

$$\frac{D\Theta}{Dt} = \frac{\partial}{\partial x_j}\left[\kappa\frac{\partial\Theta}{\partial x_j} - \langle u_j\theta\rangle\right] \tag{2.31}$$

where κ is the molecular diffusion coefficient, $\kappa\partial\Theta/\partial x_j$ represents the flux of mean concentration due to molecular diffusion, and $\langle u_j\theta\rangle$ describes the turbulent flux due to the correlation between u_j and θ. In general, the turbulent fluxes are much greater than the molecular diffusion fluxes. The turbulent flux is responsible for rapidly stirring the scalar

field. Although the turbulent fluxes are essential for rapid mixing, the molecular diffusion process is fundamentally important at the smallest scales because it transforms the large scalar gradients into a homogeneous mixture.

2.2.1.2 The Concentration Field of a Continuous Point Source

Inaccurate predictions of peak downstream concentration levels of a scalar quantity emitted from a point source have instigated the need to study concentration fluctuations. Most studies prior to the 1980s focused on predicting average concentration levels. However, concentration fluctuations can lead to downstream values that are significantly different than the average predictions. Therefore, to obtain peak values downstream, it is necessary to understand the behavior of the concentration fluctuations.

Analyzing the mean concentration field provides insight to the behavior of the passive scalar fluctuations. In the case of a uniform turbulent flow, the mean concentration field can be mathematically described as:

$$\langle \Theta(x_i) \rangle = \frac{\dot{m}}{4\pi\varepsilon_T x} exp\left(-\frac{(y^2+z^2)\langle U \rangle}{4\pi\varepsilon_T x}\right) \tag{2.32}$$

where $\dot{m}$ describes the passive scalar mass flowrate and ε_T is the turbulent diffusion coefficient. The assumptions associated with equation 2.32 include:

- The origin of the coordinate system is located at the point of the iso-kinetic release where x is the streamwise direction and y and z are the wall-normal and transverse directions, respectively
- The turbulent diffusion is isotropic and hence ε_T applies equally in each coordinate direction
- In the streamwise direction, the advective flux is much greater than the diffusive flux
- The equation is only valid for distances far from the point release, $x \gg \frac{2\varepsilon_T}{\langle U \rangle}$

Equation 2.32 indicates that the magnitude of the mean concentration decreases in the streamwise direction, and that the maximum values occur along the plume centerline (i.e. $y = z = 0$). Figure 2.2 illustrates the salient properties associated with mean concentration

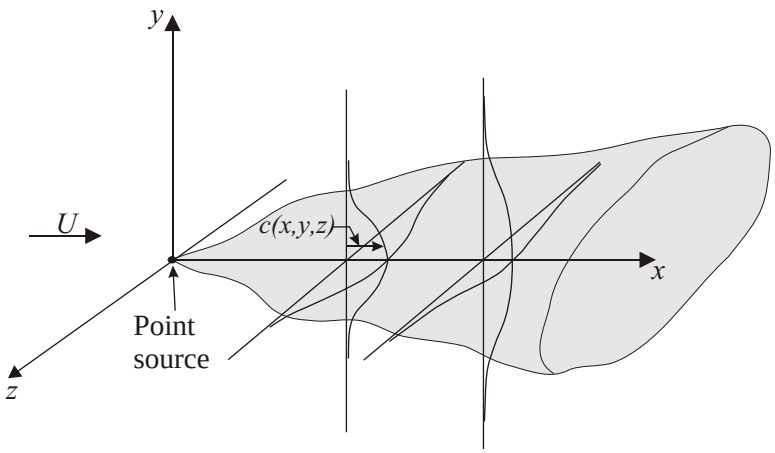

Figure 2.2: An illustration of the mean concentration field for a continuous point release (Roberts & Webster, 2002).

field. Webster et al. (2003) analyzed the vertical profiles of the mean concentration at various downstream distances for a point source released in a turbulent boundary layer. They reported that as the distance from the point release increased, the vertical profile became more uniform and the peak concentration decreased. This behavior is consistent with equation 2.32 and indicated that the plume is becoming more homogeneous. Webster et al. (2003) noted that the vertical profiles of mean concentration deviated from the predicted Gaussian profile due to the presence of the bed. Although observations of the mean concentration field are important, the instantaneous scalar field remains unresolved.

The profiles of the standard deviation of the scalar fluctuations have similar shapes as the profiles for the mean concentration. The magnitude decreases in the streamwise direction and the maximum values occur along the plume centerline. Although the behavior is similar, significant deviations occur throughout time and space. Physical arguments suggest that the scalar fluctuations should be zero at the release point. As the distance from the release point increases, the scalar fluctuations increase to a maximum value, and then decrease because

the scalar field becomes more homogeneous (i.e. less concentration fluctuation). Webster et al. (2003) noted that although the profiles appear similar, the standard deviation profile has a larger magnitude for locations within a few channel depths of the release. This difference is a result of intermittency (i.e. large concentration fluctuations above a relatively small mean value). Although this intermittent behavior describes the large-scale fluctuations, the intermittency persists to the smallest scales and eventually leads to the anomalous scaling behavior associated with the phenomenology arguments.

2.2.2 Small-Scale Behavior of Passive Scalar Mixing in Turbulent Flows

The phenomenological model developed by Kolmogorov (1941), K41 theory, was applied to the passive scalar field by Obukhov (1949) and Corrsin (1951) to create the Kolmogorov-Obukhov-Corrsin (KOC) argument. Similar to the K41 theory, the KOC argument is based on the assumption that the cascade of scalar variance from large scales to small scales occurs universally. As a result, the small-scale statistics of the passive scalar field are implicitly assumed to be isotropic.

Obukhov (1949) and Corrsin (1951) derived a length scale that described the approximate eddy size at which scalar fluctuations are dissipated by molecular diffusion. The Obukhov-Corrsin length scale is defined as:

$$\eta_{oc} \sim \left(\frac{\kappa^3}{\varepsilon}\right)^{1/4} \tag{2.33}$$

This length scale is analogous to Kolmogorov's length scale that describes the approximate eddy size at which kinetic energy is dissipated by viscosity. The ratio of these length scales leads to a non-dimensional term called the Schmidt number, Sc.

$$\frac{\eta}{\eta_{oc}} = \left(\frac{\nu^3/\varepsilon}{\kappa^3/\varepsilon}\right)^{1/4} = \left(\frac{\nu}{\kappa}\right)^{3/4} = Sc^{3/4} \tag{2.34}$$

The Schmidt number is the ratio of the kinematic viscosity of the fluid to the molecular diffusivity of the passive scalar. Therefore, the Schmidt number is only a function of fluid properties. Batchelor (1959) illustrated that the Obukhov-Corrsin length scale is only accurate for $Sc \ll 1$. Batchelor (1959) used dimensional arguments to define a length scale that properly described the scale corresponding to dissipation of the scalar variance for large Sc.

The length scale is now called the Batchelor length scale:

$$\eta_B \sim \left(\frac{\nu\kappa^2}{\varepsilon}\right)^{1/4} = \eta Sc^{-1/2} \tag{2.35}$$

K41 theory is based on a "significantly high" Reynolds number, which creates an inertial subrange for the velocity field. If the inertial subrange exists and the Schmidt number is large, three different ranges develop for the passive scalar structure functions. The inertial-convective range, $l_L \gg l \gg \eta$, consists of negligible viscous and diffusive effects. The viscous-convective range occurs when viscous effects are important, but molecular diffusivity is not important (i.e. $\eta \gg l \gg \eta_B$). The viscous-diffusive regime occurs at length scales on the order of η_B, which indicates that both viscosity and diffusivity are important.

The passive scalar structure function is defined as:

$$\langle \Delta\theta_r^n \rangle = \langle [\theta(x+r,t) - \theta(x,t)]^n \rangle \tag{2.36}$$

When the scalar field statistics are independent of viscosity and diffusivity (i.e. in the inertial-convective range), dimensional arguments indicate that the scalar structure functions are dependent only on the scalar variance dissipation rate, χ, and the energy dissipation rate, ε. Hence the scalar structure function assumes the following form:

$$\langle \Delta\theta_r^n \rangle = H_n \left(\chi^{1/2}\varepsilon^{-1/6} r^{1/3}\right)^n \tag{2.37}$$

where H_n are universal constants and the scalar variance dissipation rate is defined as $\chi = 2\kappa\langle(\partial\theta/\partial x_j)^2\rangle$.

Experimental analysis of the higher order statistics associated with the passive scalar structure functions exhibit anomalous scaling behavior. The anomalous scaling is a result of intermittent fluctuations in χ and ε. Similar to the development of the RSH, the deviation from predicted scaling resulted in the refined similarity hypotheses as applied to passive scalar fields (RSHP). The RSHP formed two conditional volume averages, χ_r and ε_r, to incorporate the intermittent fluctuation effects. Although RSHP captures the scaling behavior better than the KOC argument, it remains unable to accurately predict higher order statistics.

Recent experimental work indicates that the properties of the scalar statistics are a result of the mixing process (Shraiman & Siggia, 2000). Deviations from the predicted phenomenology arguments are a result of intermittency, which describes large scalar field fluctuations at small scales. These significant scalar fluctuations emerge in the time records of concentration as gradual ramp increases followed by sudden cliff decreases, which are consequently named ramp-cliff structures (refer to Figure 2.3). The ramp-cliff structures are responsible for the anomalous scaling behavior of the passive scalar statistics. Although the conventional theory indicates that the cascade process tends to generate local isotropy, research indicates that anisotropic behavior persists due to the ramp-cliff structures. Thus, the fundamental assumption of isotropic behavior does not apply to the passive scalar field. Therefore, other methods must be developed to analyze passive scalar mixing in turbulent flows.

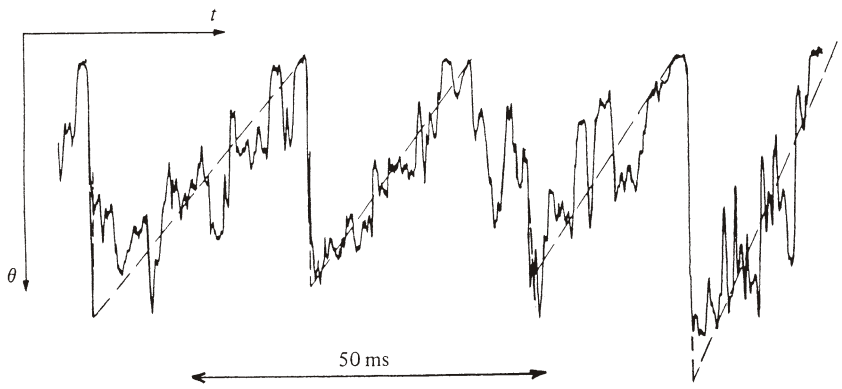

Figure 2.3: Ramp-cliff structures observed in a heated jet by Sreenivasan et al. (1979).

2.3 Multipoint Correlators

2.3.1 Introduction to Multipoint Correlators

Random turbulent motions tend to stretch and fold filaments of the passive scalar field, resulting in an unpredictable and irregular concentration field. The scalar field can be evaluated through a spatial analysis of the instantaneous concentration fluctuations averaged over time. Traditional research efforts focused on measuring concentration fluctuations at

two points in space and the visual identification of scalar filaments (i.e. spatial structures) (Shraiman & Siggia, 2000). The present study focuses on analyzing concentration fluctuations of several points in space and hence developing multipoint statistics. In addition to retaining the scaling exponent properties, multipoint correlators simultaneously probe the scalar field for the spatial orientation of the scalar filaments.

Correlation functions provide a spatial analysis of the fluctuating scalar field averaged over time. In general, the correlation function associated with N instantaneous measurement points of the scalar field is:

$$C_N = \langle \theta(r_A, t)\theta(r_B, t)...\theta(r_N, t)\rangle = \langle \theta_A \theta_B ... \theta_N \rangle \tag{2.38}$$

where $A, B, ..., N$ represent the location in space of the measurement points. Thus, for $N = 2$, equation 2.38 represents the two-point correlation function, $C_2 = \langle \theta_A \theta_B \rangle$. Similarly, $N = 3$ describes the three-point correlation function, $C_3 = \langle \theta_A \theta_B \theta_C \rangle$.

Early research of fluctuating passive scalar fields utilized two-point correlation functions. Tavoularis & Corrsin (1981) analyzed two-point scalar field statistics using a nearly homogeneous turbulent shear flow in the presence of a mean temperature gradient. They observed that the two-point correlation contours in the plane parallel to the mean velocity gradient have a characteristic asymmetric tilted oval shape (refer to Figure 2.4). The characteristic shape is most likely a result of the mean shear. In addition, Tavoularis & Corrsin (1981) reported that the two-point correlation contours in turbulent boundary layers and open channels exhibit comparable characteristic shapes that are distorted due to inhomogeneity. Although two-point statistics can be used to evaluate the basic physics of the scalar field, the presence of ramp-cliff structures requires the analysis of higher-order statistics.

Ramp-cliff structures have been observed in shear flows (Sreenivasan et al., 1979), grid turbulence (Mydlarski et al., 1998), and numerical simulations (Holzer & Siggia, 1994). As discussed previously, the anomalous scaling behavior of the passive scalar field is due to the presence of the ramp-cliff structures. Experimental analysis of the scalar field using second-order statistics yields agreement with the predictions outlined in the KOC argument and the RSHP. Therefore, the assumption of local isotropy appears valid, and the presence

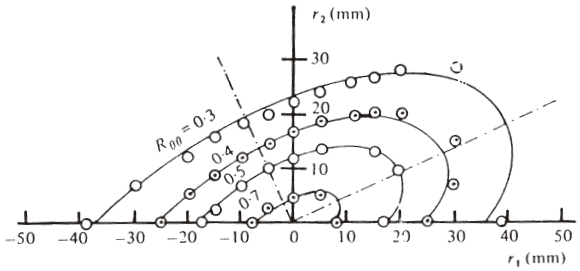

Figure 2.4: Characteristic shape of the two-point correlation contours of the fluctuating scalar field observed by Tavoularis & Corrsin (1981).

of the ramp-cliff structures cannot be detected. The third-order statistics are the lowest-order that illustrate the anisotropic effect of the ramp-cliff structures (Shraiman & Siggia, 2000). Thus, small-scale effects associated with the ramp-cliff structures must be evaluated using third-order statistics because their morphology is manifested in higher-order statistics (Mydlarski & Warhaft, 1998).

2.3.2 Current Research

Shraiman & Siggia (1996, 2000) have pioneered the theoretical foundation of multipoint correlators using the Hopf equation to derive the three-point correlation function. It is no longer necessary to assume local isotropic behavior at the small scales; therefore, the theory developed by Obukhov and Corrsin (KOC theory) is no longer employed. Shraiman & Siggia (1996) employed Kraichnan's (1968) model of a random velocity field that was considered Gaussian white-in-time. White-in-time implies that the velocity field randomly fluctuates with a correlation time significantly smaller than the time scales associated with the convective and diffusive regimes. Shraiman & Siggia (1996) noted that the velocity field is not white, and therefore derived the three point Hopf equations in the following form (Shraiman & Siggia, 1996, Mydlarski et al., 1998, Shraiman & Siggia, 2000):

$$\frac{\partial}{\partial t}\langle\theta(r_1,t)\theta(r_2,t)...\theta(r_N,t)\rangle = H_N\langle\theta(r_1,t)\theta(r_2,t)...\theta(r_N,t)\rangle + I_N(r_1,r_2,...r_N,t) \quad (2.39)$$

where H_N is the Hopf operator, $H_N = -\sum_{i\neq j}\left(D^{\gamma}_{ab}(r_i - r_j) + \kappa\delta_{ab}\right)\partial^a_i\partial^b_j$, I_N represents inhomogeneous source terms dependent on lower order correlators, ∂^a_i is the partial derivative

in the i direction at point a, γ is a scaling index, and D_{ab}^{γ} is a symmetric tensor that varies proportionally to $|r|^{2-\gamma}$. The general solution to equation 2.39 is of the form:

$$C_N = H_N^{-1} I_N + \sum_j a_j \Psi_{N,j} \tag{2.40}$$

where the inhomogeneous solution is represented by $H_N^{-1} I_N$ and the homogeneous solution is given by $\sum_j a_j \Psi_{N,j}$. In the inertial subrange, each solution presented in equation 2.40 can be fully described using scaling exponents. Dimensional analysis yields good agreement with KOC theory for the inhomogeneous solutions. However, the scaling exponents associated with the homogeneous solutions are non-trivial and must be evaluated as nonlinear eigenvalues. Shraiman & Siggia (1996) conclude that the three-point correlation function derived from the Hopf equation is symmetric.

The theoretical predictions must be verified using experimental data. Mydlarski & Warhaft (1998) have analyzed three-point correlations of a nearly homogeneous and isotropic turbulent flow field. The point configuration was developed using two cold wire probes and Taylor's frozen turbulence hypothesis. The resulting coordinate system is depicted in Figure 2.5(a). The prime coordinate system shown in Figure 2.5(b) is introduced because the symmetric properties reported by Mydlarski & Warhaft (1998) occur about the line $x_2 = 2x_1$. Figure 2.6 illustrates the symmetric results, which are independent of the Reynolds number. The physical significance of the three-point correlations of the concentration fluctuations is that the spatial orientation of the scalar filaments can be revealed using the geometry and orientation of the points (refer to Figure 1.2). Mydlarski & Warhaft (1998) also conclude that the observed symmetry is a result of the ramp-cliff structures. Since the ramp-cliff structures appear in shear flows as well as non-shear flows, they speculate that the symmetric behavior may indeed be universal to all turbulent flows (with a mean scalar gradient). Shraiman & Siggia (1996) indicate that shear flows may provide a more realistic picture of turbulent flows because shear flows contain steady large-scale shear that affects the inertial and dissipative regimes.

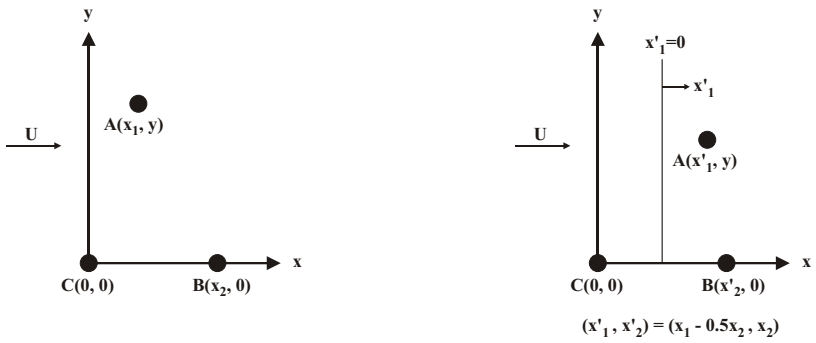

(a) Coordinate System (b) Rotated Coordinate System

Figure 2.5: Coordinate system for the three-point correlation of the concentration fluctuations developed by Mydlarski & Warhaft (1998).

2.4 Contributions of Current Research

The purpose of the present work is to analyze the passive scalar field in a turbulent boundary layer using multipoint correlation functions. The three-point correlations of the fluctuating scalar field are examined to determine the scaling exponent properties, extract geometric relationships of the scalar filaments, and evaluate the small-scale structure of the concentration field. The results of this research are expected to aid in predicting the mixing and transport of the turbulent passive scalar field.

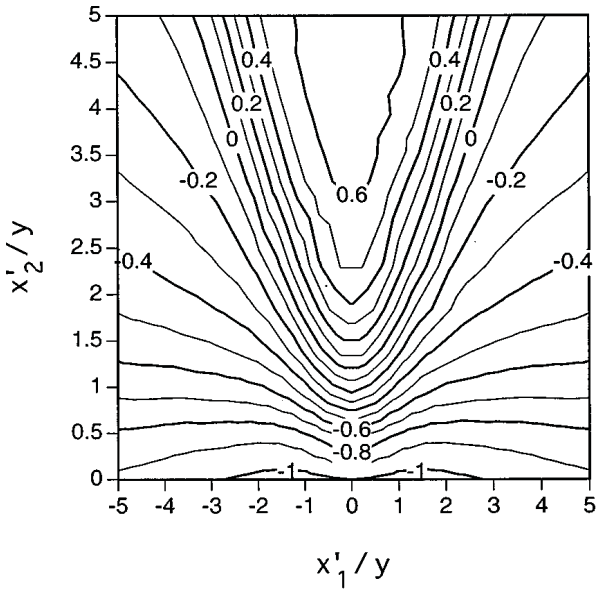

Figure 2.6: Symmetric properties of the three-point correlation of the concentration fluctuations in the rotated coordinate system observed by Mydlarski & Warhaft (1998). Contour levels correspond to the normalized three-point correlation function.

CHAPTER III

METHODS

3.1 Experimental Facility

The concentration field data analyzed in the current study was collected by L. Prasad Dasi. Full details associated with the experimental setup and scalar field visualization technique are described in Dasi (2004). To provide the context for the data, the experimental characteristics are summarized in this section.

3.1.1 Flow Facility

3.1.1.1 Flow Field

The turbulent boundary layer was developed in a rectangular, smooth-bed, tilting flume located in the Environmental Fluid Mechanics Laboratory at Georgia Tech. The flume is 1.07 m wide ($W = 1.07\ m$) and 24.4 m long. Data were collected for three Reynolds numbers ($Re = \langle U \rangle H/\nu = 5000$, 10000, and 20000) to evaluate the effects of different velocity fields on the passive scalar mixing behavior. The flume was adjusted for each Reynolds number to create a uniform open channel flow depth of 100 mm ($H = 100\ mm$). Measurements of the passive scalar field were obtained 23 m from the channel inlet to ensure the turbulent boundary layer was fully developed. As a result, the velocity field is inhomogeneous in only the wall-normal direction.

3.1.1.2 Passive Scalar Field

The turbulent passive scalar field was developed through the iso-kinetic point release of a high Schmidt number dye ($Sc = \nu/\kappa \simeq 1000$, $\nu = 1$ x 10^{-6} m^2/s, and $\kappa \simeq 1$ x 10^{-9} m^2/s) into the inertial layer of a fully developed open channel turbulent boundary layer. The release nozzle was located along the flume centerline, 50 mm above the bed surface. A streamlined fairing was installed on the injection nozzle to minimize wake perturbations and ensure that the mixing process is a result of the turbulent boundary layer. The fluctuating

scalar field was recorded at six distances downstream from the release location: H, $2.5H$, $5H$, $10H$, $20H$, and $40H$. Three nozzle diameters were employed to examine the effects of the injection length scale on the passive scalar mixing behavior. Table 3.1 summarizes the cases observed in the current study. For Case 1, the Reynolds number varied while the

Table 3.1: Experimental cases

Case 1		Case 2	
Re	Nozzle Diameter	Re	Nozzle Diameter
5000			2.2 mm
10000	4.7 mm	10000	4.7 mm
20000			9.4 mm

injection length scale was constant. In Case 2, the Reynolds number was constant while the injection length scale varied. Table 3.2 provides the important flow characteristics reported by Dasi (2004).

Table 3.2: Characteristics of the turbulent passive scalar field.

Re	$\langle U \rangle$ (mm/s)	U_∞ (mm/s)	u_* (mm/s)	η (μm)	η_B (μm)	u_k (mm/s)	τ_k (s)	$\tilde{u}$ (mm/s)	ε (m^2/s^3)
5000	50	62.6	3.25	758	24	1.3	0.60	5.3	3.0 x 10^{-6}
10000	100	136.6	6.40	417	13	2.4	0.20	11.8	3.3 x 10^{-5}
20000	200	238.0	10.60	291	9	3.4	0.08	19.1	1.4 x 10^{-4}

3.1.2 Planar Laser-Induced Fluorescence (PLIF)

Instantaneous images of the turbulent passive scalar field were captured using planar laser-induced fluorescence (PLIF). PLIF is an optical technique designed to provide 2-D flow visualization and quantitative measurements of scalar fields. The method was based on the following procedure:

- Fluorescent tracer molecules were injected into the fluid
- A laser sheet excited the molecules to a higher energy state
- The excited molecules emitted light at a longer wavelength, which is directly proportional to the tracer concentration

- A charged coupled device (CCD) camera captured images of the emitted light
- The images were corrected and calibrated to obtain the instantaneous concentration fields

PLIF is a popular technique because a high-quality spatial resolution of the scalar field can be non-obtrusively measured.

The PLIF system consisted of a laser, sheet forming optics, imaging optics, and a CCD camera. An Argon-ion laser beam (514 nm, 5 W, Coherent Innova 90) was focused into a Gaussian beam with a $1/e^2$ waist diameter of 80 μm at the measurement location (50 mm above the flume bed) using a 6x beam expander and a 2 m focal length symmetrical convex lens. The laser sheet was formed by sweeping the Gaussian laser beam through the measurement region in 3 ms, resulting in a nearly frozen scalar field. The resulting laser sheet was formed in the streamwise−wall-normal $(x - y)$ plane along the flume centerline. The incident light emitted by the scalar field passed through filters that blocked ultraviolet and infrared light. In addition, a long-pass optical filter (Tiffen Orange 21) with a cutoff wavelength of 516 nm was used to eliminate scattered laser light. The camera CCD chip contained a rectangular pixel array of 1392 x 1024. A Nikkon MicroNikkor macro lens (200 mm) provided an image resolution of approximately 13 μm/pixel. A total of 12,000 instantaneous images were captured at the six downstream distances for each of the cases presented in Table 3.1.

The calibration procedure required capturing images of a known, uniform scalar concentration in the range 0-100 $\mu g/l$. Two hundred images were captured for each calibration concentration level. An average image pixel intensity was calculated for each given scalar concentration value. Image pixel intensities that significantly deviated from the mean were removed from the average calculation process. The removal of these records eliminated the possibility of including the affects of ambient fluid entrainment into the calibration image. The average pixel intensities were corrected for laser sheet attenuation and the least squares regression method was employed to provide the linear best-fit relationship between pixel intensity and scalar concentration. The resulting relationship provided the calibration

equation required to convert image pixel intensity to scalar concentration.

3.1.3 Concentration Measurement Region

The size of the image captured by the CCD camera is 1392 x 1024 pixels. The data analyzed in the current study is restricted to a 512 x 512 sub-region of the image. The sub-region is located below the nozzle centerline, where Dasi (2004) reported a nearly constant mean concentration gradient. As a result, the effects of a uniform mean concentration gradient on the small-scale structure of the scalar field can be evaluated. Figure 3.1 illustrates the location of the sub-image measurement region.

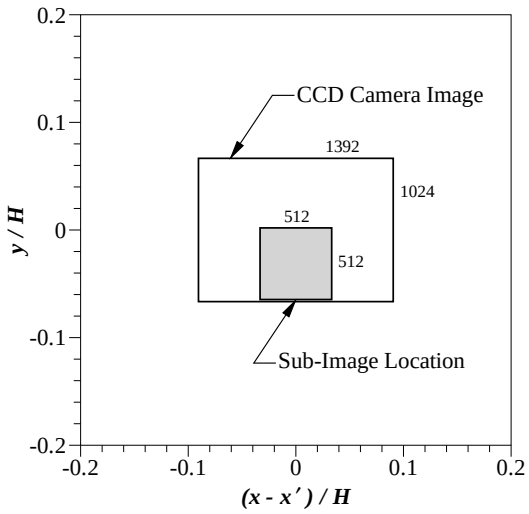

Figure 3.1: The measurement region associated with $x' = 0.1\ m$, $0.25\ m$, $0.5\ m$, $1.0\ m$, $2.0\ m$, and $4.0\ m$. The shaded region represents the sub-image location used to evaluate the effects of a constant concentration gradient on the small-scale structure of the scalar field (Dasi, 2004).

3.2 Two-Point Correlations of the Concentration Fluctuations

The purpose of this thesis is to analyze the experimental data described in the previous section. The primary focus of the analysis is two-point and multi-point correlation functions.

The procedure for calculating the two-point correlation functions is described in this section. Two-point correlation functions provide a spatial analysis of the scalar field using two points in space. As outlined in section 2.3.1, the correlation function for two unique points in space is:

$$C_2(r_i) = \langle \theta(r_A, t)\theta(r_B, t)\rangle = \langle \theta(x_i, t)\theta(x_i + r_i, t)\rangle = \langle \theta_A \theta_B \rangle \tag{3.1}$$

where r_i describes the spatial separation vector of points A and B. Note that the subscript i takes on a value of 1, 2, or 3 to represent the streamwise, wall-normal, and transverse directions, respectively. The brackets, $\langle\rangle$, typically indicate time-averaging over a long period, but the current analysis employs a combination of temporal and spatial averaging, as described below. A high correlation indicates that the samples may be part of the same filament structure. Accordingly, equation 3.1 provides a measure of the filament size for the fluctuating scalar field.

The current study analyzes the one-dimensional and two-dimensional structure of the two-point correlation function. The one-dimensional analysis is conducted independently in the streamwise, x, and wall-normal, y, directions. The one-dimensional analysis provides an estimate of the average filament size in each direction. The two-dimensional study considers separations in the streamwise and wall-normal directions simultaneously. The two-dimensional analysis results in a contour map of the two-point correlation function when plotted in $x - y$ space.

3.2.1 One-Dimensional Analysis of the Fluctuating Scalar Field

Figure 3.2 illustrates the coordinate systems used for the one-dimensional analysis of the two-point correlation calculations. The streamwise calculations begin on a fixed image with points A and B at (0,0). Point A remains at the (0,0) position and the correlation calculations continue as the x position of point B varies from $r_1 = 0$ to $r_1 = 6.643\ mm$. Then, points A and B are moved one pixel in the $+y$ direction (i.e. to position (0,0.013 mm)) and the correlation calculations are repeated. Note that at the beginning of each iteration points A and B are coincident and $\langle \theta_A^2 \rangle$ is calculated. This calculation process continues until the entire image has been traversed (i.e. up to $y = 6.643\ mm$). This

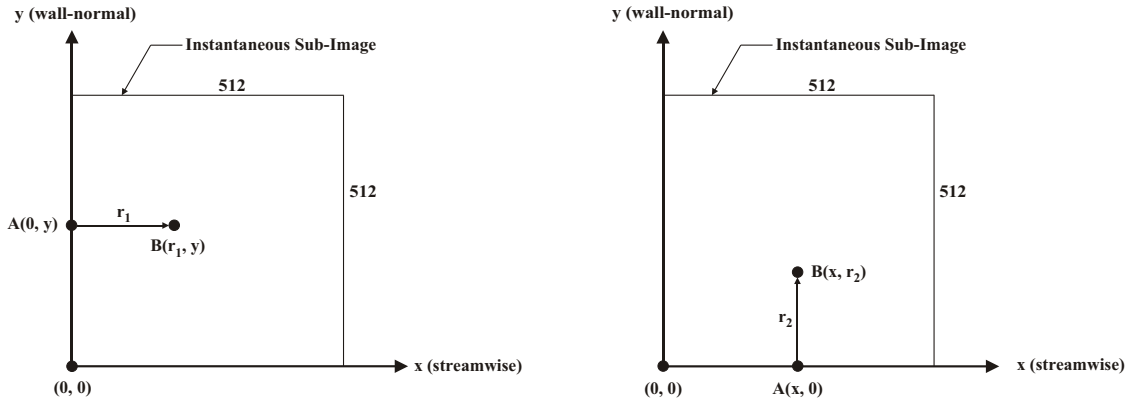

(a) Streamwise Correlations

(b) Wall-Normal Correlations

Figure 3.2: Coordinate system for the one-dimensional analysis of the two-point correlation of the concentration fluctuations.

calculation sequence is repeated for each of the 12,000 images. The resulting correlation function is therefore an average for both the time period of the record and the spatial region of the sub-image.

A similar calculation procedure is utilized for the correlation function in the wall-normal direction. The calculations begin on a fixed image with points A and B at (0,0). Point A remains at the (0,0) position and the correlation calculations occur as the y position of point B varies from $r_2 = 0$ to $r_2 = 6.643\ mm$. Then, points A and B are moved one pixel in the $+x$ direction (i.e. to position (0.013 mm,0)), and the correlation calculations repeat. At the beginning of the iteration process, points A and B are coincident and $\langle \theta_A^2 \rangle$ is calculated. The calculation process continues until the entire image has been traversed (i.e. up to $x = 6.643\ mm$). The procedure is repeated until each of the 12,000 images have been analyzed.

3.2.2 Two-Dimensional Analysis of the Fluctuating Scalar Field

Figure 3.3 illustrates the coordinate system used to analyze the two-point correlation function. Point A is initially located at the lower left corner of the dotted square depicted in Figure 3.3 and assigned the coordinates ($r_1 = 0$,$r_2 = 0$). Point B traverses the sub-image from $r_1 = -2.500\ mm$ to $r_1 = 2.500\ mm$ and $r_2 = -2.500\ mm$ to $r_2 = +2.500\ mm$ and

the correlation is calculated for each combination. The position of point A is then moved,

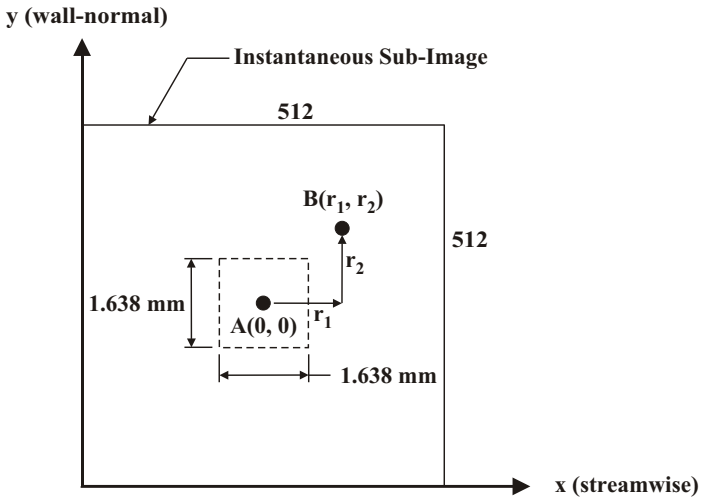

Figure 3.3: Coordinate system for the two-dimensional analysis of the two-point correlation of the concentration fluctuations.

and the correlation calculations are repeated for the new origin. This two-point correlation calculation method continues until point A has visited every point in the inner-most region of the fixed image (denoted by the dotted square in Figure 3.3). The calculation is repeated for all 12,000 images.

3.2.3 Integral Length Scale of the Scalar Field

The integral length scale describes the typical length of the largest filaments of the passive scalar field. The two-point correlation function is normalized by $\langle \theta_A^2 \rangle$ and integrated to obtain the integral length scale:

$$l_L = \int_0^{+\infty} \frac{C_2(r)}{\langle \theta_A^2 \rangle} dr \tag{3.2}$$

Hence, the integral length scale corresponds to the area under the normalized correlation function curve. For the calculation in equation 3.2, the two-point correlation function, $C_2(r)$, must be known for all separation distances, r. However, since the sub-image is finite

in size, the experimental data terminates at a separation distance of 6.643 mm. In order to overcome this limitation, the least squares regression method was employed to fit a 6^{th} order polynomial and an exponential function to the collected data points. The 6^{th} order polynomial fit the existing data points with an R-square statistic value ≥ 0.987 for each case. Thus, the polynomial provided an accurate fit to the correlation function data up to the data truncation point (i.e. 6.643 mm). The exponential function did not fit the data as well as the polynomial (the R-square statistic was much smaller, $\simeq 0.8$). However, an exponential function was fit to the collected data for separation distances greater than 3.328 mm. The resulting exponential curve matched the slope of the collected data at the truncation point better than the polynomial curve. Therefore, the integral length scale is calculated by integrating the fit polynomial curve from $r = 0$ to $r = 6.643$ mm. The slope of the exponential function at the truncation point was used to approximate the distance required for the correlation function to reach a value of 0. The triangular area estimated in this manner was added to the area under the fit polynomial curve. Figure 3.4 demonstrates the methods used to estimate the integral length scale.

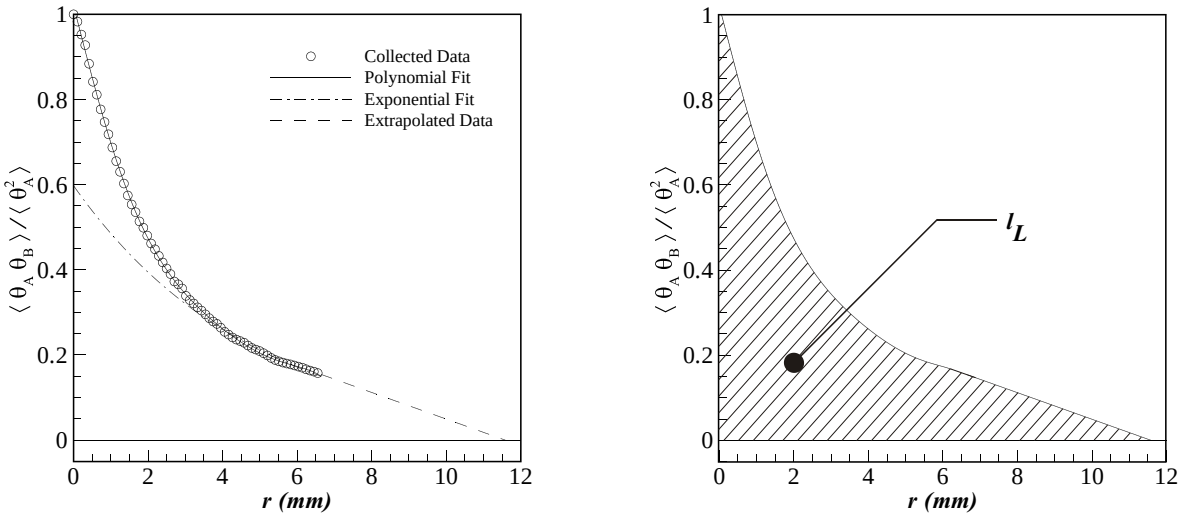

Figure 3.4: Fit curves and extrapolated data region used to estimate the integral length scale of the scalar field. The hatched region represents the area used to calculate the integral length scale.

3.3 Three-Point Correlations of the Concentration Fluctuations

Three-point correlation functions provide a spatial analysis of the scalar field using three unique points in space:

$$C_3 = \langle \theta(r_A, t)\theta(r_B, t)\theta(r_C, t)\rangle = \langle \theta_A \theta_B \theta_C \rangle \tag{3.3}$$

where A, B, and C represent the location of the measurement points. In addition to evaluating the scaling properties of the concentration field, three-point correlators simultaneously probe the field for the presence of spatial structures. Therefore, the geometry (size, shape, and orientation) of the three-point configuration affects the correlation function. The current study analyzes geometric configurations evaluated by Mydlarski & Warhaft (1998) and Celani & Vergassola (2001).

3.3.1 Three-Point Geometry Based on Mydlarski & Warhaft (1998)

Mydlarski & Warhaft (1998) used cold-wire probes in a wind tunnel to measure the three-point correlation. Two cold-wire probes were separated in the wall-normal direction. Thus, the three points consisted of simultaneous measurements from the two probes and a delayed measurement from one of the probes. Employing the Taylor frozen turbulence hypothesis converted the delayed measurement to a spatially separated measurement in the flow direction. The advantage of the current approach is that the Taylor frozen turbulence hypothesis is not needed since the planar data directly provides numerous combinations of three points. As a preliminary calculation, the Mydlarski & Warhaft (1998) configuration is examined for comparison. The coordinate system for the three point configuration evaluated by Mydlarski & Warhaft (1998) is described in section 2.3.2. Figure 3.5 illustrates the three-point geometry in the context of the current measurement region. Note that the correlations are calculated in an unrotated coordinate system and plotted in a rotated coordinate system to transform the symmetry about the line $x_2 = 2x_1$ to the vertical axis (refer to Figure 2.5).

The value of the separation distance, Y, associated with point A remains constant. The appropriate separation distance is dependent on the integral length scale. Mydlarski & Warhaft (1998) employed a ratio of the separation distance to the integral length scale

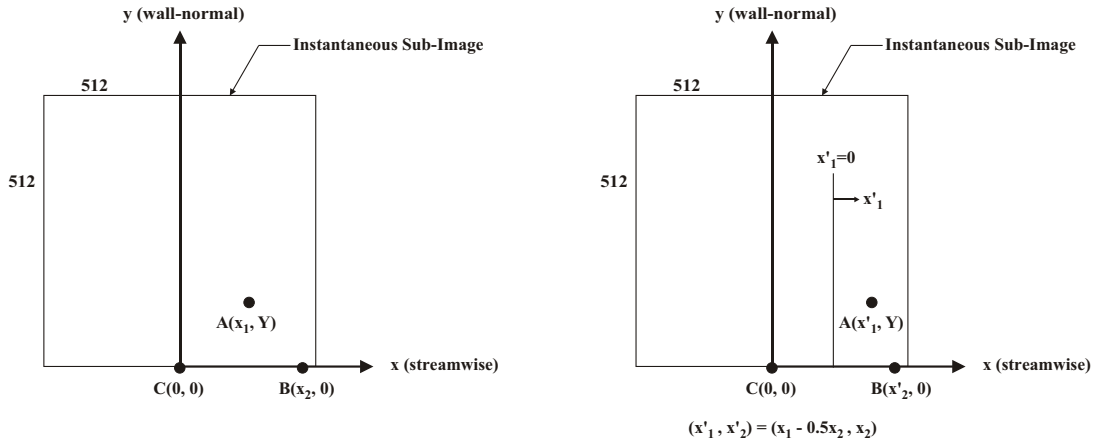

(a) Coordinate System

(b) Rotated Coordinate System

Figure 3.5: Coordinate system for the analysis of the three-point correlation of the concentration fluctuations (Mydlarski & Warhaft, 1998).

of $Y/l_L \simeq 0.05$. The wall-normal position of point B remains coincident with point C throughout the calculation process. Point C is initially located at the midpoint of the sub-image along the bottom of the measurement region (along the line $y = 0$) and assigned the coordinates (0,0). Points A and B traverse the entire sub-image from $x_1 = -3.328$ mm to $x_1 = +3.328$ mm and $x_2 = -3.328$ mm to $x_2 = +3.328$ mm and the correlation is calculated for each combination. Point C is then moved 0.013 mm in the $+y$ direction and assigned the coordinates (0,0). The correlation calculations were repeated for the new origin. This calculation method continues until point A reaches the top of the measurement region. The procedure is repeated for all 12,000 images.

3.3.2 Three-Point Geometry Based on the Shape Function

The three-point correlation function depends on the location of unique points in space. As a result, the correlation function is dependent on the size, shape, and orientation of the triangle defined by the three points. Based on a theoretical analysis, Celani & Vergassola (2001) reported that the three-point correlation function becomes:

$$C_3 = R^{\zeta_3} f(\chi, w) cos\varphi + \text{subdominant higher order terms} \tag{3.4}$$

where $f(\chi, w)$ contains the effects of different triangular shapes, φ describes the orientation of the triangle with respect to the mean scalar gradient, and ζ_3 is the scaling exponent of the global size variable, R. The global size variable provides a characteristic length of the triangle formed by the three points:

$$R = \sqrt{\frac{r_{AB}^2 r_{BC}^2 r_{CA}^2}{3}} \tag{3.5}$$

where r_{ij} is the distance between the i^{th} and j^{th} points.

The parameters associated with the shape factor, χ and w, are defined using the Euler parameterization described by Shraiman & Siggia (1998) and Pumir (1998). Using the following definitions:

$$\vec{\rho_1} = \frac{\vec{r_2} - \vec{r_1}}{\sqrt{2}} \qquad \text{and} \qquad \vec{\rho_2} = \frac{2\vec{r_3} - \vec{r_2} - \vec{r_1}}{\sqrt{6}} \tag{3.6}$$

where the spatial location of points A, B, and C are denoted as $\vec{r_1}$, $\vec{r_2}$, and $\vec{r_3}$, respectively, the parameters associated with the shape factor become:

$$\chi = \frac{1}{2} \tan^{-1} \left[\frac{2\vec{\rho_1} \bullet \vec{\rho_2}}{\vec{\rho_2}^2 - \vec{\rho_1}^2} \right] \tag{3.7}$$

and

$$w = 2\frac{|\vec{\rho_1} \times \vec{\rho_2}|}{R^2} = \frac{2(\rho_{11}\rho_{22} - \rho_{12}\rho_{21})}{R^2} \tag{3.8}$$

The definitions for χ and w are advantageous because the three-point geometric configuration is completely described by these two parameters. In addition, χ and w remain constant as the triangular configuration is translated, rotated, and dilated.

The two configurations analyzed in the current study are the isosceles triangle and collinear points depicted in Figures 3.6 and 3.7, respectively. As illustrated in the figures, each geometry is a fixed arrangement that is rotated to several orientations relative to the flow (or relative to the mean scalar gradient). As a result, the shape factor, $f(\chi, w)$, remains constant and the effects of the global size variable and the orientation of the triangle can be analyzed. The maximum value of d is limited to the global size variable being on the order of the integral length scale (i.e. $R_{max} \simeq 1.5\ mm$). Using equation 3.5, the maximum

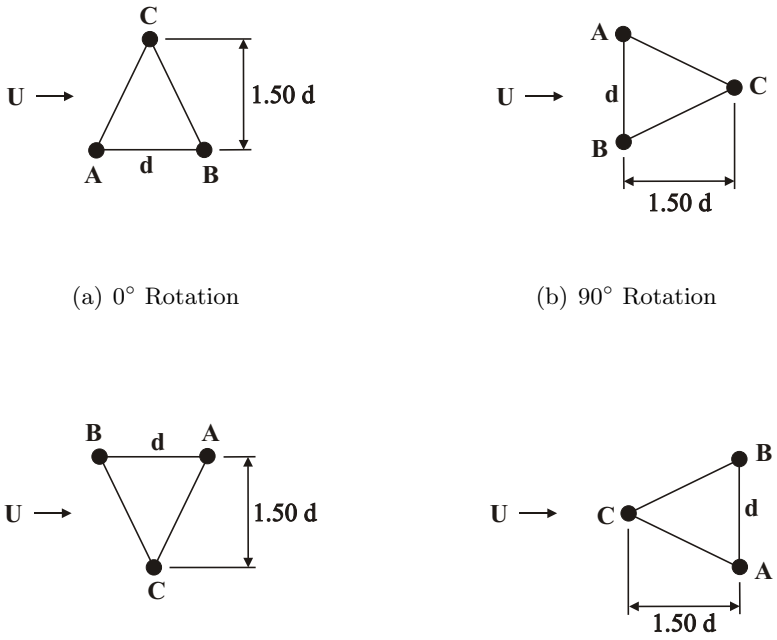

(a) 0° Rotation

(b) 90° Rotation

(c) 180° Rotation

(d) 270° Rotation

Figure 3.6: The geometry of the three-point correlation of the concentration fluctuations analyzed using the isosceles triangle configuration.

global size variable associated with the isosceles triangle configuration is:

$$R_{max} = \sqrt{8d_{max}^2} \tag{3.9}$$

where $d_{max} \simeq 0.53\ mm$ (i.e. the value of d associated with the isosceles triangle varies from $d = 0\ mm$ to $d = 0.53\ mm$). In a similar manner, the global size variable associated with the collinear three-point configuration is:

$$R_{max} = \sqrt{2d_{max}^2} \tag{3.10}$$

where $d_{max} \simeq 1.06\ mm$ (i.e. the value of d associated with the collinear configuration varies from $d = 0\ mm$ to $d = 1.06\ mm$).

Figure 3.8 (a) illustrates the coordinate system used to analyze the three-point correlation associated with both the isosceles triangle and collinear configuration. The isosceles triangle calculations begin on a fixed image where the centroid is initially located at the

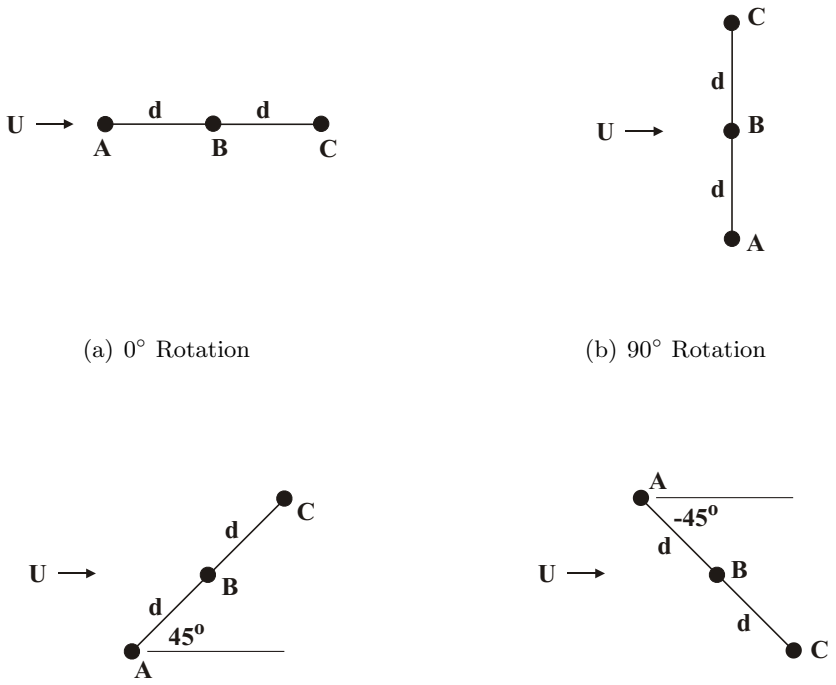

(a) 0° Rotation

(b) 90° Rotation

(c) 45° Rotation

(d) −45° Rotation

Figure 3.7: The geometry of the three-point correlation of the concentration fluctuations analyzed using the collinear configuration.

upper left corner of the dotted square depicted in Figure 3.8 (a). Points A, B, and C are moved to the appropriate positions in the measurement region such that the geometric constraints are maintained (i.e. over the range of values of d) and the correlation is calculated for each combination. The geometric constraints defined in the calculations ensure that points A, B, and C are coincident with a specific pixel location for each value of d. Then, the centroid is moved, and the correlation calculations are repeated. This calculation method continues until the origin has traversed the inner-most region of the fixed image (denoted by the dotted square in Figure 3.8 (a)). The calculation is repeated for all 12,000 images.

The collinear calculations begin by initially locating point B at the upper left corner of the dotted square depicted in Figure 3.8 (b). Points A and C are moved to the appropriate

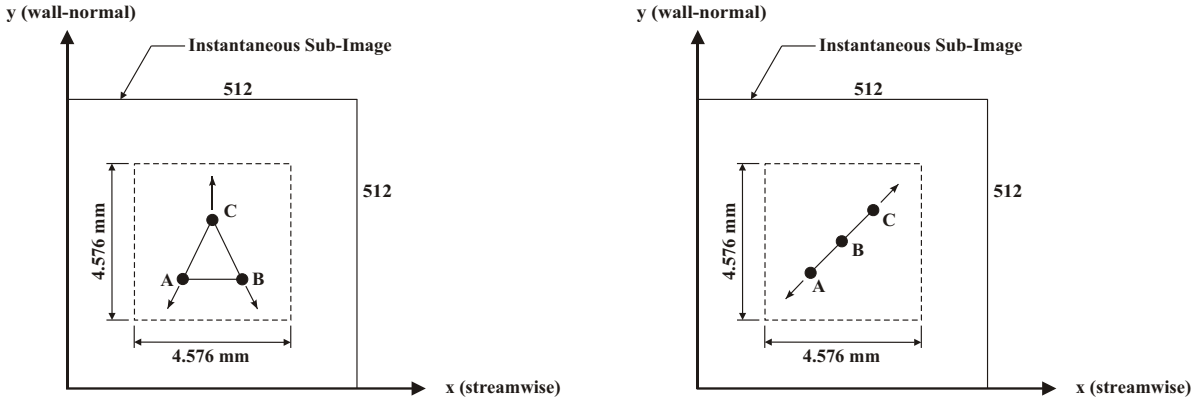

(a) Isosceles Configuration

(b) Collinear Configuration

Figure 3.8: Coordinate system of the three-point correlation function analysis based on the shape function.

positions in the measurement region such that the geometric constraints are maintained and the correlation is calculated for each combination. The geometric constraints defined in the calculations ensure that points A, B, and C are coincident with a specific pixel location for each value of d. Then, point B is moved, and the correlation calculations are repeated. This three-point calculation method continues until point B has traversed the inner-most region of the fixed image (denoted by the dotted square in Figure 3.8 (b)). The calculation is repeated for all 12,000 images.

3.4 Convergence of the Three-Point Correlations of the Concentration Fluctuations

The correlation functions analyzed in the current study are averaged over both the time period of the record and the spatial region of the sub-image. The average correlation function for any given geometric configuration must converge to a unique value. Using the geometry described in Mydlarski & Warhaft (1998), two randomly selected three-point configurations were analyzed to illustrate the number of temporal and spatial samples required for convergence. The first configuration, Configuration A, was taken from the data set associated with $Re = 10000$, $D = 4.7\ mm$, and $x = 0.5\ m$ ($\frac{x_1'}{Y} = -56.25$, $\frac{x_2'}{Y} = 37.50$,

and $Y = 0.052\ mm$). The second configuration, Configuration B, was taken from the data set associated with $Re = 20000$, $D = 4.7\ mm$, and $x = 2.0\ m$ ($\frac{x_1'}{Y} = 22.92$, $\frac{x_2'}{Y} = -12.50$, and $Y = 0.078\ mm$).

The standard error is used to assess the convergence of the mean concentration values. The standard error is defined as:

$$s_e = \frac{s}{\sqrt{n}} \tag{3.11}$$

where n represents the total number of samples collected and s is the standard deviation:

$$s = \sqrt{\frac{1}{N}\sum_{n=1}^{N}[\theta_A\theta_B\theta_C|_n - \langle\theta_A\theta_B\theta_C\rangle]^2} \tag{3.12}$$

Figures 3.9(a) and 3.9(b) illustrate the standard error associated with the average correlation function for Configuration A and Configuration B, respectively. The variable N illustrated in Figure 3.9 denotes the number of images and hence describes the time dimension of the recorded data. Each image contains approximately five hundred spatial samples. The number of samples for N number of images is approximately 500 x N ($n \simeq 500N$). Therefore, the total number of samples included in the averaging calculation is on the order of six million. The intermittent jumps in the standard error record result from isolated, high correlation value events (i.e. a large filament briefly covered the points). Note that in each case for $N > 8000$, highly correlated intermittent events have little effect on the standard error.

The standard error associated with Configurations A and B converge to values of 7.5 x 10^{-7} and 3.1 x 10^{-10}, respectively. The average correlation function corresponding to Configurations A and B equal values of 1.9 x 10^{-5} and 1.1 x 10^{-8}, respectively. Accordingly, the standard error is approximately 4% of the mean correlation value for Configuration A and 3% of the mean correlation value for Configuration B. The results indicate that the standard error of the average correlation function is less than 5%, if the total number of samples included in the calculation is on the order of six million. Table 3.3 summarizes these calculations.

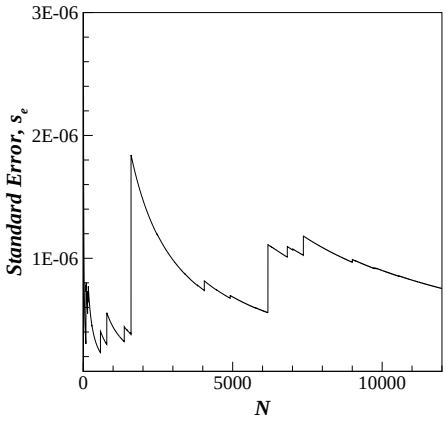

(a) Configuration A

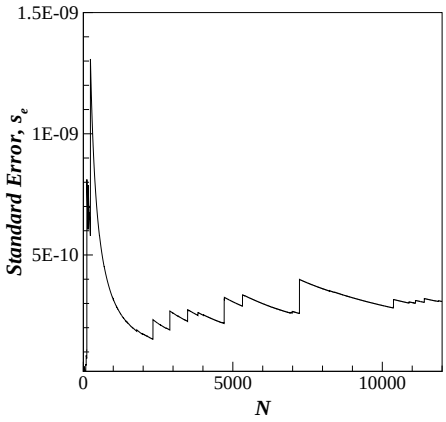

(b) Configuration B

Figure 3.9: The standard error associated with the randomly selected three-point correlation of the fluctuating scalar field.

Table 3.3: The error associated with the average three-point correlation of the concentration fluctuations.

Configuration	s_e	$\langle\theta_A\theta_B\theta_C\rangle$	$\frac{s_e}{\langle\theta_A\theta_B\theta_C\rangle}$
A	7.5 x 10^{-7}	1.9 x 10^{-5}	4%
B	3.1 x 10^{-10}	1.1 x 10^{-8}	3%

CHAPTER IV

RESULTS AND DISCUSSION

4.1 Two-Point Correlations of the Concentration Fluctuations

The calculation methods used to produce the following results are outlined in section 3.2.1 and illustrated in Figure 3.2. The two-point correlation functions in the streamwise and wall-normal directions are plotted in Figures 4.1 through 4.5 as a function of the separation distance, r. As illustrated in each figure, the streamwise correlations and the wall-normal correlations become coincident as the distance from the point release increases. This behavior indicates that the scalar field achieves independence of the streamwise and wall-normal directions as it evolves downstream. The figures also show that for small separation distances ($r < 1\ mm$), the rate at which the normalized correlation function approaches zero increases as the distance from the point release increases (i.e. $\frac{d}{dr}\left(\frac{\langle\theta_A\theta_B\rangle}{\langle\theta_A^2\rangle}\right)$) becomes increasingly negative as x increases). Therefore, as the scalar field evolves downstream, smaller separation distances are required to maintain a significant correlation between points A and B. In general, the streamwise correlation function is greater than the wall-normal correlation function. This signifies that the filament structures are stretching in the streamwise direction for greater lengths than in the wall-normal direction. This behavior is expected because the mean velocity of the turbulent boundary layer and the iso-kinetic release of the scalar occurs in the streamwise direction, and hence preferentially aligns the scalar filaments.

The effects of various Reynolds numbers for a constant injection length scale are demonstrated by comparing Figures 4.1, 4.2, and 4.3. For any specified downstream distance, the streamwise and wall-normal correlations become more coincident as the Reynolds number increases. Therefore, increasing the Reynolds number results in the scalar field achieving independence of the streamwise and wall-normal directions (i.e. becoming more isotropic)

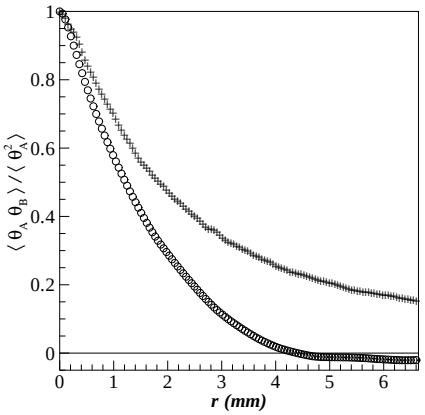

(a) $x = 0.1\ m$

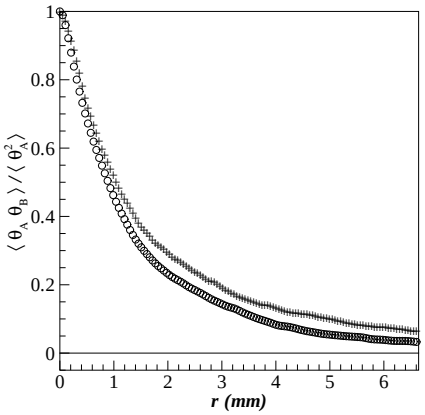

(b) $x = 0.25\ m$

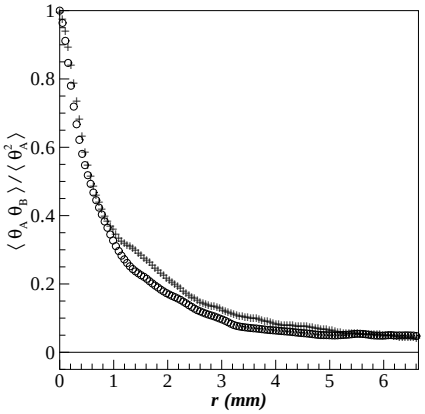

(c) $x = 0.5\ m$

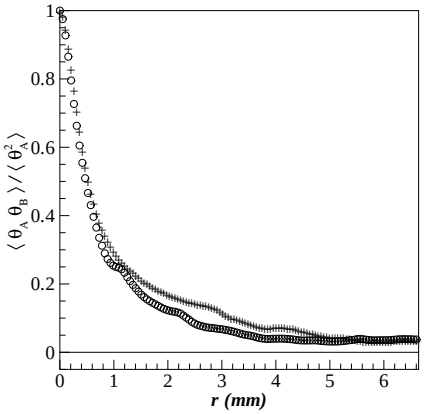

(d) $x = 1.0\ m$

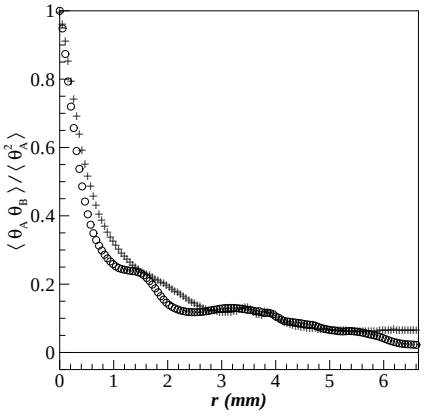

(e) $x = 2.0\ m$

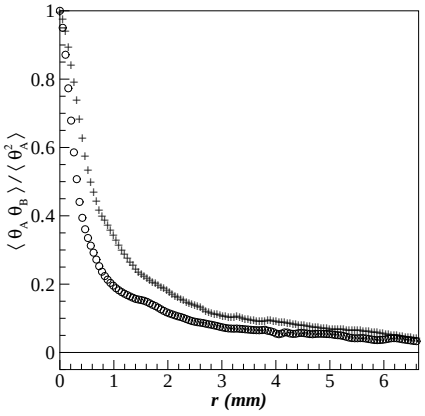

(f) $x = 4.0\ m$

Figure 4.1: Two-point correlation function of the fluctuating scalar field for $Re = 5000$ and nozzle diameter $D = 4.7\ mm$. Data shown for correlations in the streamwise direction (+) and wall-normal direction (○) at the indicated distances downstream from the point release.

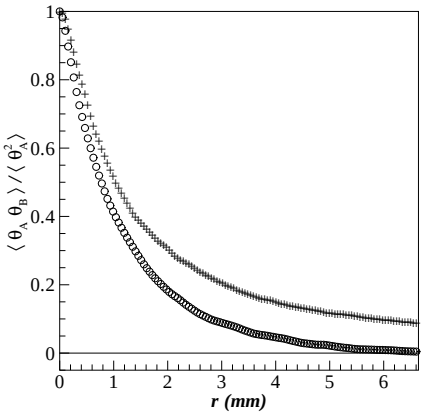

(a) $x = 0.1\ m$

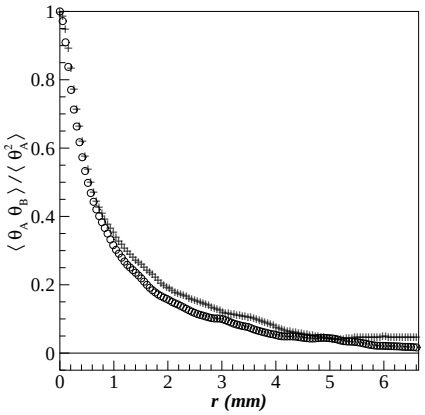

(b) $x = 0.25\ m$

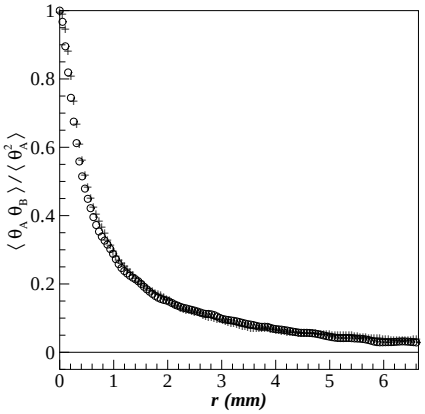

(c) $x = 0.5\ m$

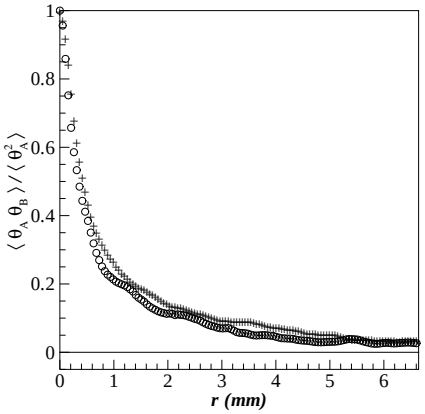

(d) $x = 1.0\ m$

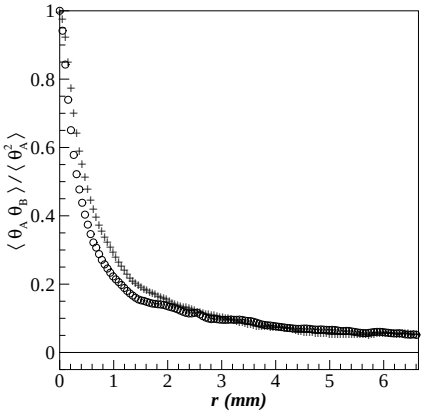

(e) $x = 2.0\ m$

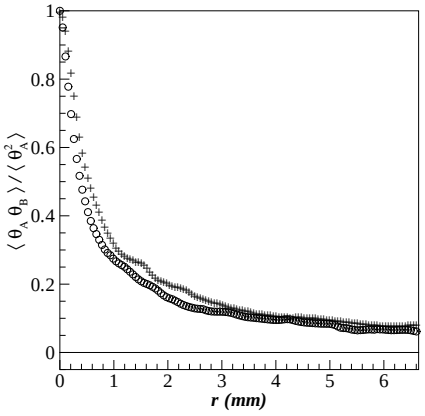

(f) $x = 4.0\ m$

Figure 4.2: Two-point correlation function of the fluctuating scalar field for $Re = 10000$ and nozzle diameter $D = 4.7\ mm$. Data shown for correlations in the streamwise direction (+) and wall-normal direction (○) at the indicated distances downstream from the point release.

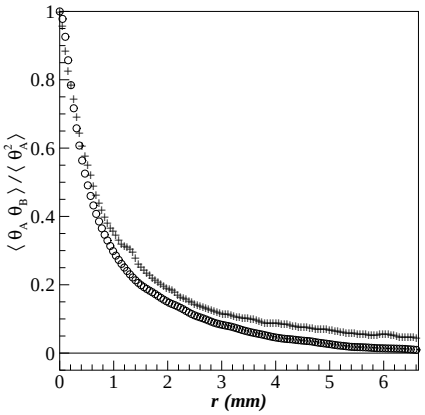

(a) $x = 0.1\ m$

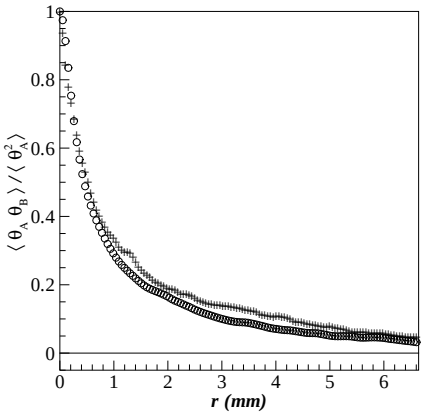

(b) $x = 0.25\ m$

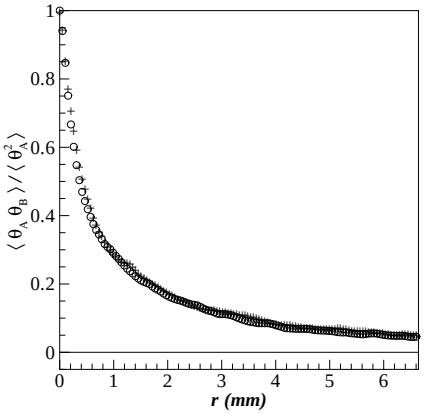

(c) $x = 0.5\ m$

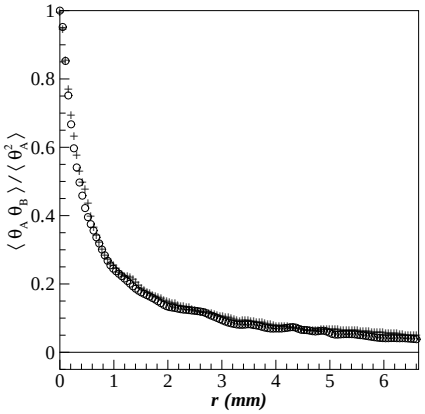

(d) $x = 1.0\ m$

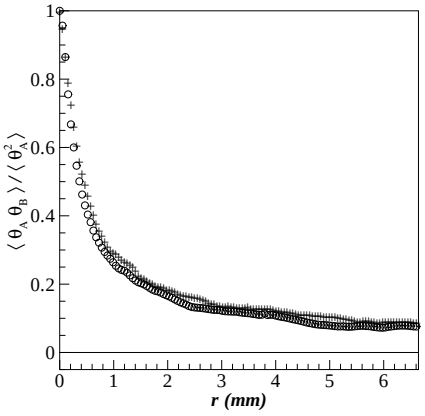

(e) $x = 2.0\ m$

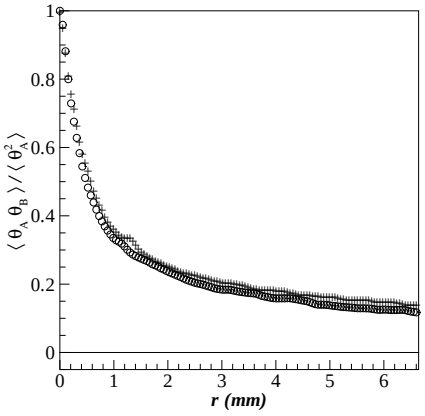

(f) $x = 4.0\ m$

Figure 4.3: Two-point correlation function of the fluctuating scalar field for $Re = 20000$ and nozzle diameter $D = 4.7\ mm$. Data shown for correlations in the streamwise direction (+) and wall-normal direction (○) at the indicated distances downstream from the point release.

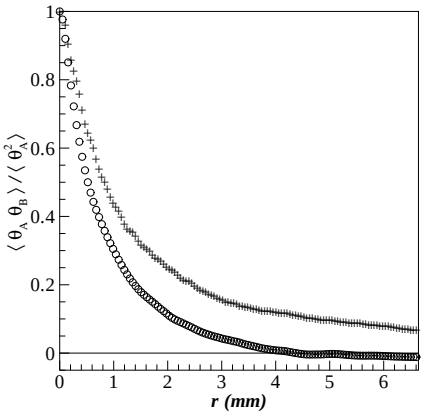

(a) $x = 0.1\ m$

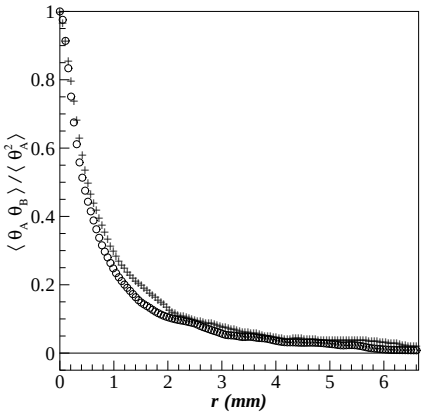

(b) $x = 0.25\ m$

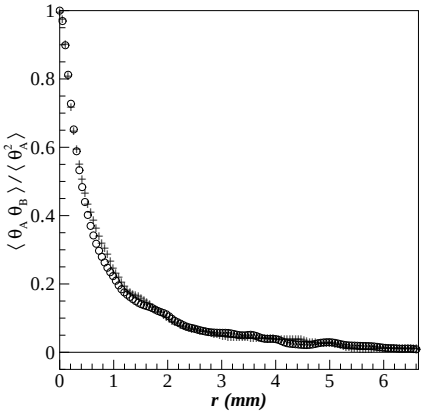

(c) $x = 0.5\ m$

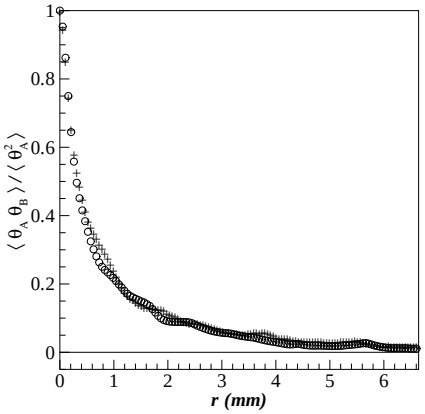

(d) $x = 1.0\ m$

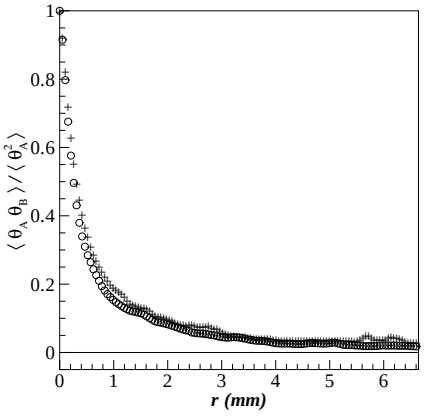

(e) $x = 2.0\ m$

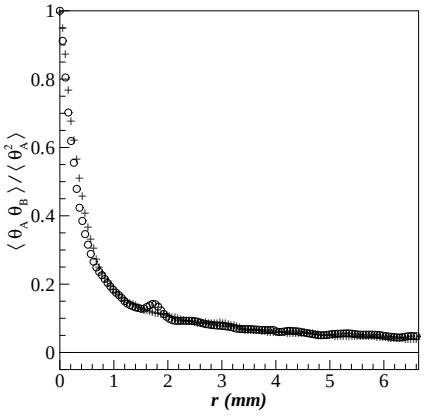

(f) $x = 4.0\ m$

Figure 4.4: Two-point correlation function of the fluctuating scalar field for $Re = 10000$ and nozzle diameter $D = 2.2\ mm$. Data shown for correlations in the streamwise direction (+) and wall-normal direction (○) at the indicated distances downstream from the point release.

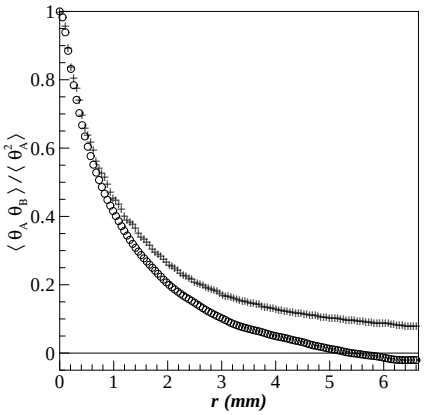

(a) $x = 0.1\ m$

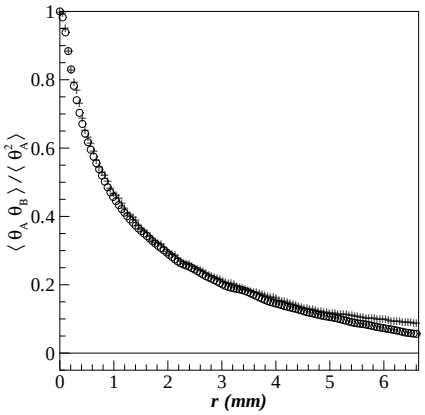

(b) $x = 0.25\ m$

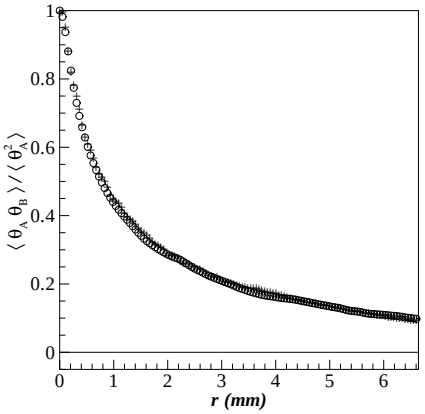

(c) $x = 0.5\ m$

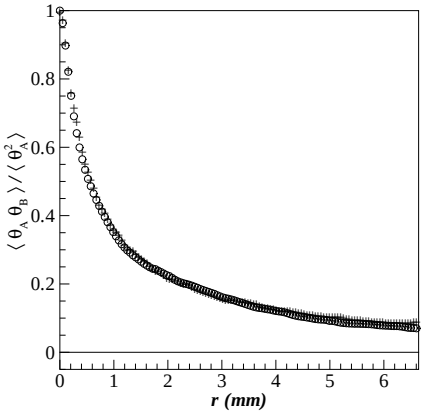

(d) $x = 1.0\ m$

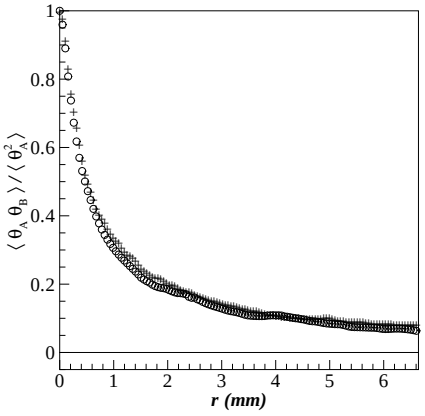

(e) $x = 2.0\ m$

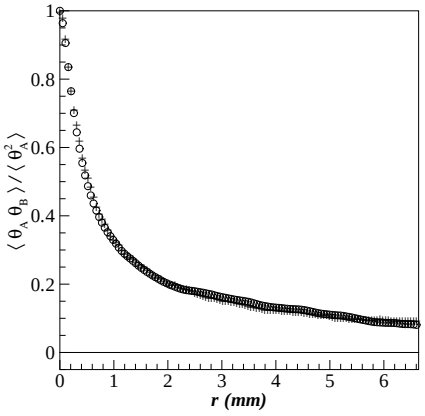

(f) $x = 4.0\ m$

Figure 4.5: Two-point correlation function of the fluctuating scalar field for $Re = 10000$ and nozzle diameter $D = 9.4\ mm$. Data shown for correlations in the streamwise direction (+) and wall-normal direction (○) at the indicated distances downstream from the point release.

closer to the point release. At downstream distances close to the point release ($x = 0.1\ m$ and $x = 0.25\ m$), the correlation functions decrease in magnitude as the Reynolds number increases. At intermediate downstream distances ($x = 0.5\ m$ and $x = 1.0\ m$), the functions are approximately equal for each Reynolds number. The correlation functions for farther downstream distances ($x = 2.0\ m$ and $x = 4.0\ m$) increase in magnitude as the Reynolds number increases. These observations can be explained by examining the turbulent scalar advective-diffusion equation (equation 2.31). As the Reynolds number increases, the turbulent flux due to the correlation between u_j and θ increases (i.e. the scalar field experiences more rapid mixing). Rapidly stirring the scalar field facilitates molecular diffusion, which leads to a homogenized scalar field. Close to the point release, rapidly stirring the scalar field decreases the magnitude of the correlation function because the effects of molecular diffusion have not been realized. The more homogeneous scalar field associated with larger Reynolds numbers becomes apparent at farther downstream distances. As the scalar field homogenizes, the tail of the two-point correlation functions increase in magnitude and approach a value of zero more slowly.

Figures 4.2, 4.4, and 4.5 illustrate the effects of various injection length scales for a constant Reynolds number. At any specified downstream distance, the streamwise and wall-normal correlations become more coincident as the nozzle diameter increases. A similar trend was previously noted for increasing Reynolds numbers. Therefore, larger injection length scales, as well as larger Reynolds numbers, tend to generate a scalar field that is independent of the streamwise and wall-normal directions closer to the point release. In addition, the correlation functions increase in magnitude as the nozzle diameter increases. This behavior is expected because as the nozzle diameter increases, the sizes of the coherent filaments associated with the scalar field also increase and a greater distance is required for the particles to become uncorrelated to the initial concentration value.

4.1.1 Integral Length Scale of the Scalar Field

The calculation methods used to produce the following results are outlined in section 3.2.3 and illustrated in Figure 3.4. The integral length scale is defined as the area under

the curves depicted in Figures 4.1 through 4.5. As a result, the foregoing observations are also reflected in this quantity. The integral length scale describes the separation distance beyond which the correlation of the concentration fluctuations is poor. Physically, it is related to the size of the filaments because samples collected from within the same filament would be well-correlated. Table 4.1 summarizes the results of the integral length scale calculations in the streamwise and wall-normal directions. Figures 4.6 and 4.7 illustrate the trends associated with the integral length scale for a constant nozzle diameter and a constant Reynolds number, respectively.

Table 4.1: Integral length scale of the scalar field in the streamwise and wall-normal directions.

$x(m)$	Direction	$Re = 5000$ $D = 4.7\ mm$ $l_L(mm)$	$Re = 10000$ $D = 2.2\ mm$ $l_L(mm)$	$Re = 10000$ $D = 4.7\ mm$ $l_L(mm)$	$Re = 10000$ $D = 9.4\ mm$ $l_L(mm)$	$Re = 20000$ $D = 4.7\ mm$ $l_L(mm)$
0.1	Streamwise	3.0	1.8	2.1	1.9	1.4
	Wall-Normal	1.5	0.9	1.2	1.2	1.0
0.25	Streamwise	1.9	1.1	1.4	2.0	1.4
	Wall-Normal	1.5	0.9	1.1	1.8	1.1
0.5	Streamwise	1.4	0.9	1.2	2.0	1.3
	Wall-Normal	1.4	0.8	1.1	2.0	1.2
1.0	Streamwise	1.2	0.9	1.1	1.8	1.3
	Wall-Normal	1.3	0.8	0.9	1.6	1.1
2.0	Streamwise	1.5	1.1	1.3	1.7	1.7
	Wall-Normal	1.1	0.7	1.1	1.4	1.4
4.0	Streamwise	1.4	1.0	1.7	1.8	2.4
	Wall-Normal	1.0	1.0	1.3	1.6	2.0

The effects of various Reynolds numbers for a constant nozzle diameter are depicted in Figure 4.6. Close to the release location ($x = 0.1\ m$), the integral length scale in the streamwise direction is greater than the integral length scale in the wall-normal direction. In addition, the integral length scale decreases as the Reynolds number increases. As previously

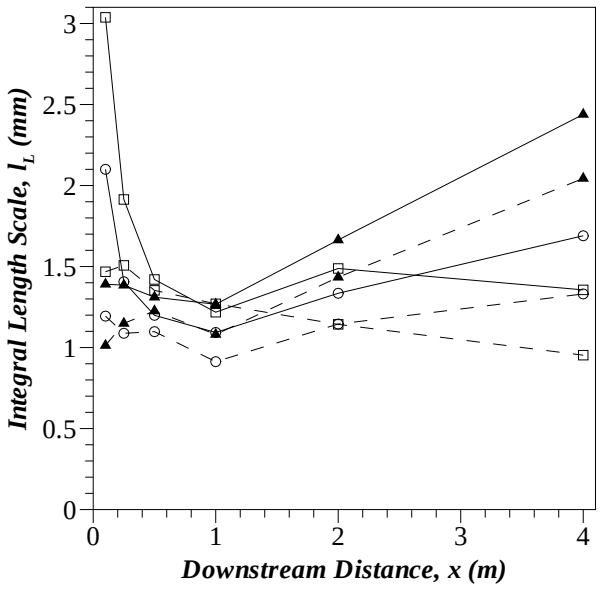

Figure 4.6: The integral length scale of the scalar field calculated from the two-point correlations of the concentration fluctuations for a constant injection length scale, $D = 4.7$ mm. Data shown for $Re = 5000$ (□), $Re = 10000$ (○), and $Re = 20000$ (▲). The solid and dotted lines represent the streamwise and wall-normal directions, respectively.

discussed, this trend exists because more rapid mixing is associated with higher Reynolds numbers and samples become uncorrelated at smaller separation distances. The streamwise and wall-normal integral length scales rapidly approach similar values that persist through downstream distances of $x = 0.5$ m and $x = 1.0$ m. Furthermore, the integral length scales associated with different Reynolds numbers also remain approximately equal for the intermediate downstream distances ($x = 0.5$ m and $x = 1.0$ m). As a result, the integral length scale appears to be a function of the nozzle diameter and independent of the different velocity fields in this region. For farther downstream distances ($x \geq 2.0$ m), the integral length scale in the streamwise direction becomes larger than the integral length scale in the wall-normal direction. However, the difference in the integral length scales remains nearly constant and the trends associated with each direction for a specified Reynolds number are nearly parallel. Note that the integral length scale begins to increase at a rate that

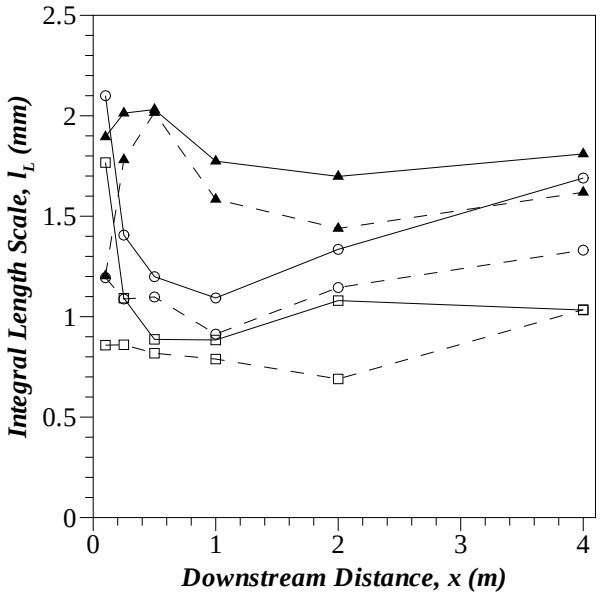

Figure 4.7: The integral length scale of the scalar field calculated from the two-point correlations of the concentration fluctuations for a constant Reynolds number, $Re = 10000$. Data shown for $D = 2.2\ mm$ (□), $D = 4.7\ mm$ (○), and $D = 9.4\ mm$ (▲). The solid and dotted lines represent the streamwise and wall-normal directions, respectively.

is dependent on the Reynolds number. As the Reynolds number increases, the rate of change associated with the integral length scale also increases, thus illustrating the affects of a homogeneous scalar field. As the scalar field homogenizes, the integral length scale increases because greater separation is required for poor correlation between samples.

Figure 4.7 illustrates the integral length scale for various nozzle diameters at a constant Reynolds number. Close to the point release ($x \leq 0.25\ m$), the integral length scale in the streamwise direction is greater than the integral length scale in the wall-normal direction. The streamwise and wall-normal integral length scales approach similar values at a downstream distance of $x = 0.5\ m$. In addition, the magnitude of the integral length scale at this location depends on the injection length scale. Note that as the nozzle diameter increases, the integral length scale also increases. Although the integral length scale associated with each direction tends to vary as the scalar field is advected farther downstream

(i.e. the streamwise integral length scale becomes greater than the wall-normal integral length scale), the relationship between the integral length scale and the injection length scale persists. Note that the largest integral length scale continues to be associated with the largest nozzle diameter. This behavior is expected because as the injection length scale increases, the filament structures associated with the resulting scalar field are also larger and hence greater separation distances are required for samples to become uncorrelated.

4.1.2 Two-Point Correlation Contours of the Fluctuating Scalar Field

The separation vector between the two points of the correlation function does not need to be aligned with the flow and wall-normal directions. In this section, the general two-point correlation function is presented for data in the plane defined by the streamwise and wall-normal directions (i.e. the $x - y$ plane), which also corresponds to the plane parallel to the mean velocity gradient. The calculation methods used to produce the following results are outlined in section 3.2.2 and illustrated in Figure 3.3. The two-point correlation contours for the $x - y$ plane are illustrated in Figures 4.8 through 4.12.

In an isotropic scalar field, the two-point correlation contours in the $x-y$ plane would be symmetric concentric circles. Near the point release ($x \leq 0.25\ m$), the scalar field becomes more anisotropic for low Reynolds numbers and smaller injection length scales (note the distinct elliptical shape of the contours in Figures 4.8 (a) & (b) and 4.11 (a) & (b)). As the Reynolds number and the injection length scale increase, the anisotropy associated with the scalar field appears less severe (note the elliptical shape of the contours in Figures 4.10 (a) & (b) and 4.12 (a) & (b) is less distinct).

At farther downstream distances ($x > 0.25\ m$), the mean velocity shear affects the scalar field and similar anisotropic conditions develop for each case. As the mean velocity shear acts on the scalar field, the two-point correlation contours develop a tilted, asymmetric elliptical shape. Tavoularis & Corrsin (1981) reported that this characteristic shape is a result of mean velocity shear. In addition, the oval shape becomes increasingly distorted as the scalar field is advected downstream. Tavoularis & Corrsin (1981) concluded that the distortion is due to the inhomogeneity of the mean velocity associated with turbulent

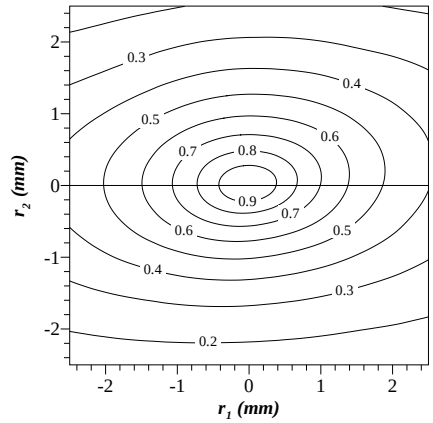

(a) $x = 0.1m$

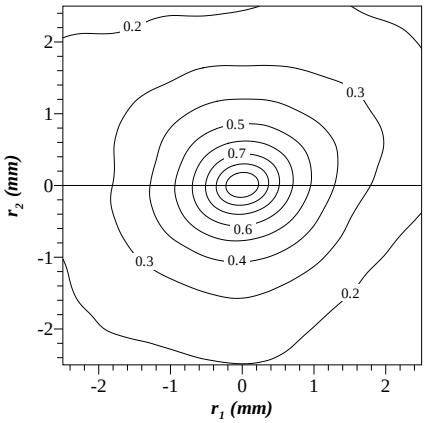

(b) $x = 0.25\ m$

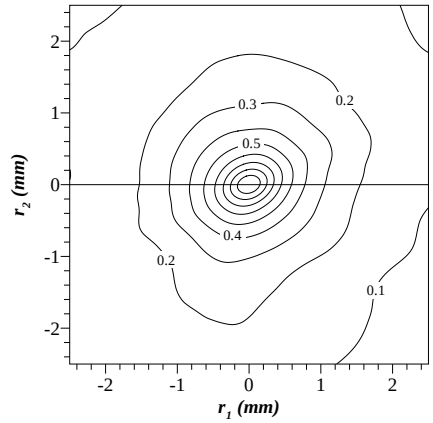

(c) $x = 0.5\ m$

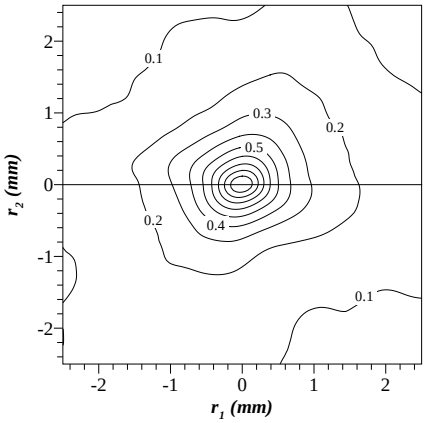

(d) $x = 1.0\ m$

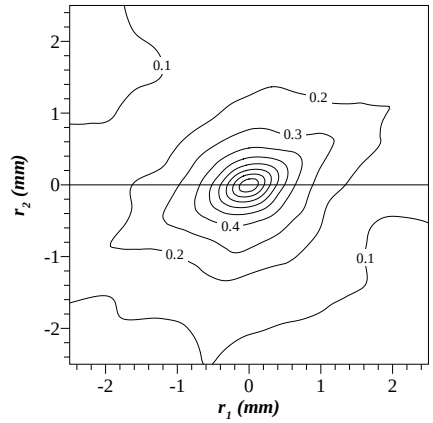

(e) $x = 2.0\ m$

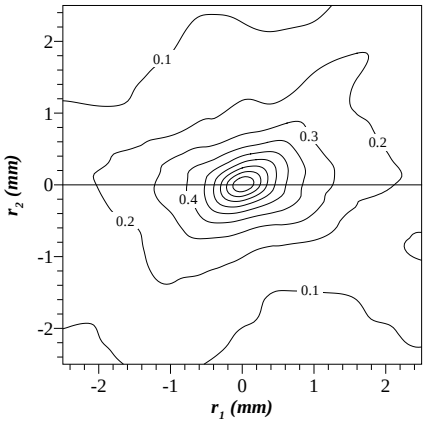

(f) $x = 4.0\ m$

Figure 4.8: Two-point correlation contours of the fluctuating scalar field for $Re = 5000$ and nozzle diameter $D = 4.7\ mm$ at the indicated distances downstream from the point release.

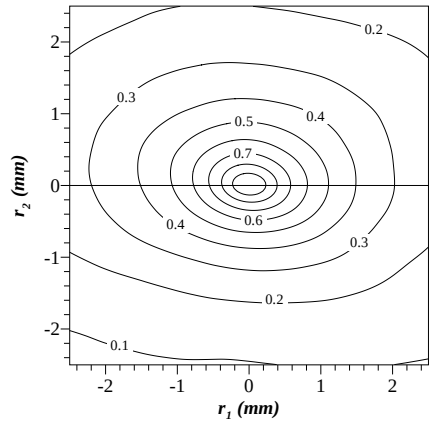

(a) $x = 0.1\ m$

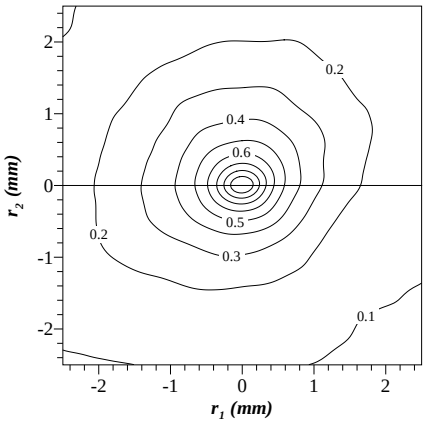

(b) $x = 0.25\ m$

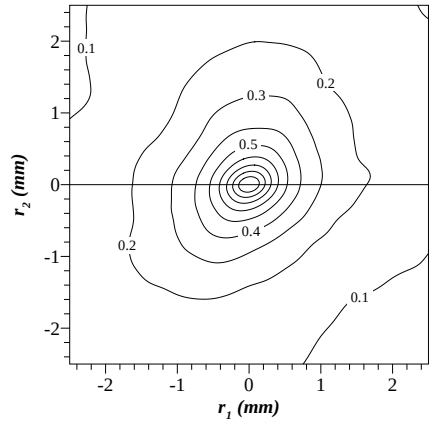

(c) $x = 0.5\ m$

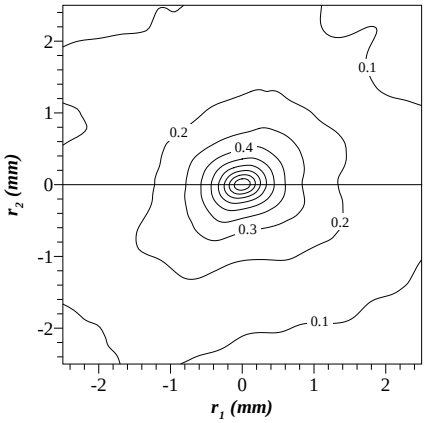

(d) $x = 1.0\ m$

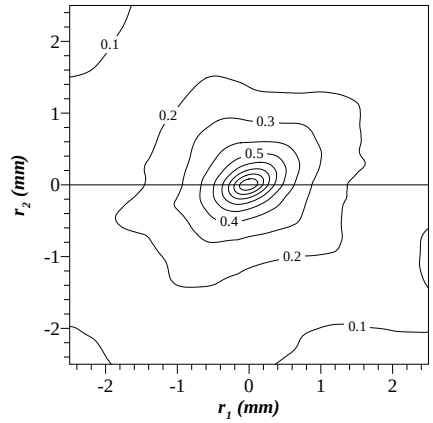

(e) $x = 2.0\ m$

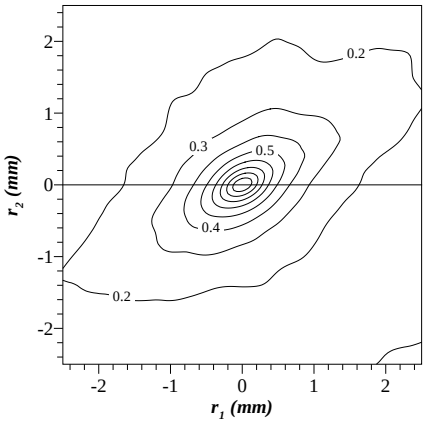

(f) $x = 4.0\ m$

Figure 4.9: Two-point correlation contours of the fluctuating scalar field for $Re = 10000$ and nozzle diameter $D = 4.7\ mm$ at the indicated distances downstream from the point release.

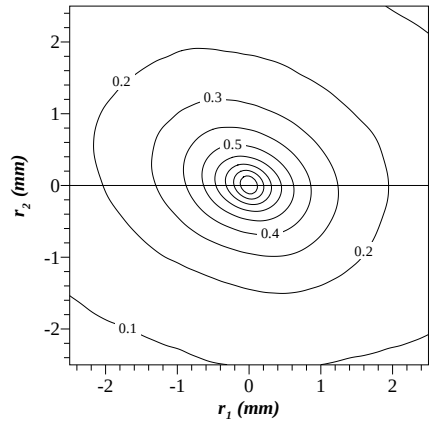

(a) $x = 0.1\ m$

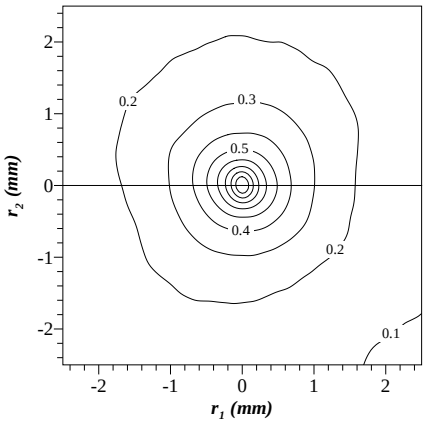

(b) $x = 0.25\ m$

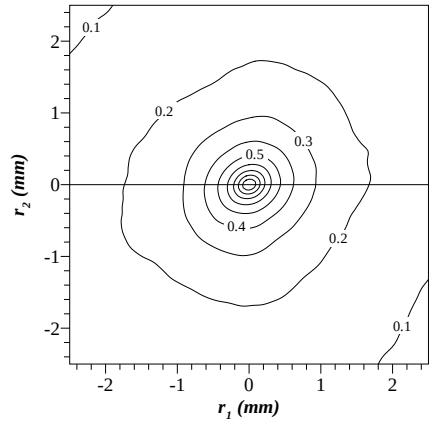

(c) $x = 0.5\ m$

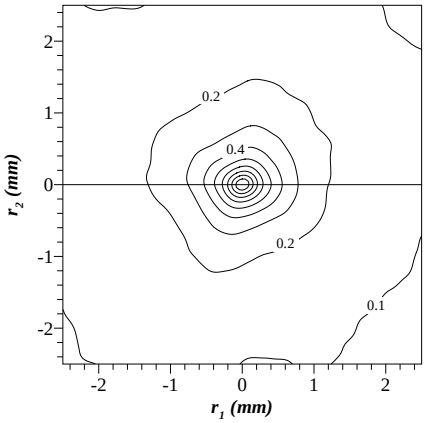

(d) $x = 1.0\ m$

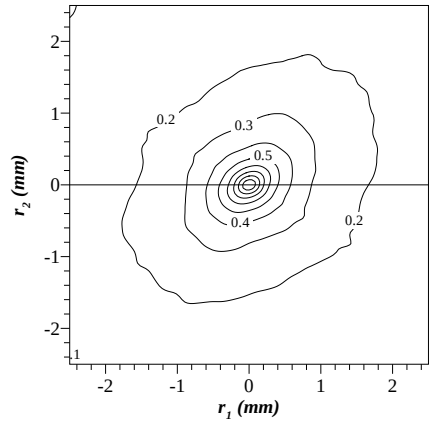

(e) $x = 2.0\ m$

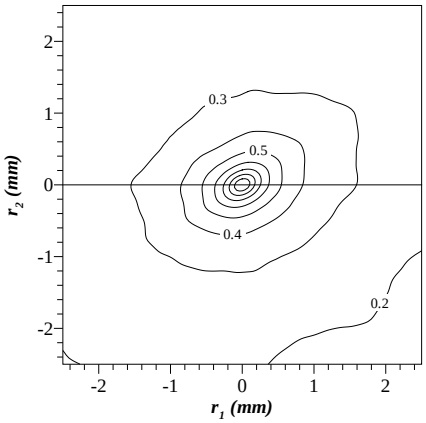

(f) $x = 4.0\ m$

Figure 4.10: Two-point correlation contours of the fluctuating scalar field for $Re = 20000$ and nozzle diameter $D = 4.7\ mm$ at the indicated distances downstream from the point release.

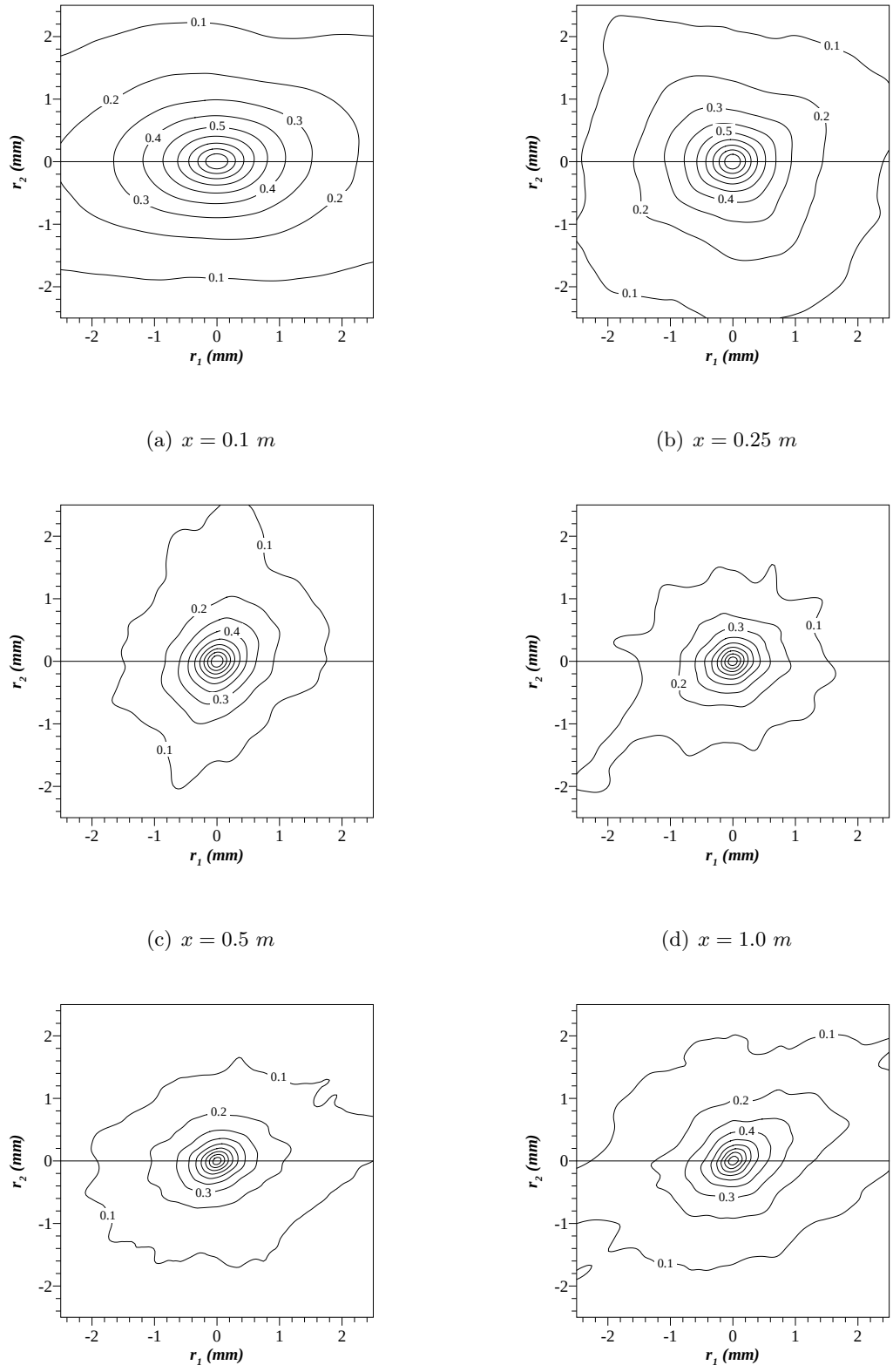

(a) $x = 0.1\ m$

(b) $x = 0.25\ m$

(c) $x = 0.5\ m$

(d) $x = 1.0\ m$

(e) $x = 2.0\ m$

(f) $x = 4.0\ m$

Figure 4.11: Two-point correlation contours of the fluctuating scalar field for $Re = 10000$ and nozzle diameter $D = 2.2\ mm$ at the indicated distances downstream from the point release.

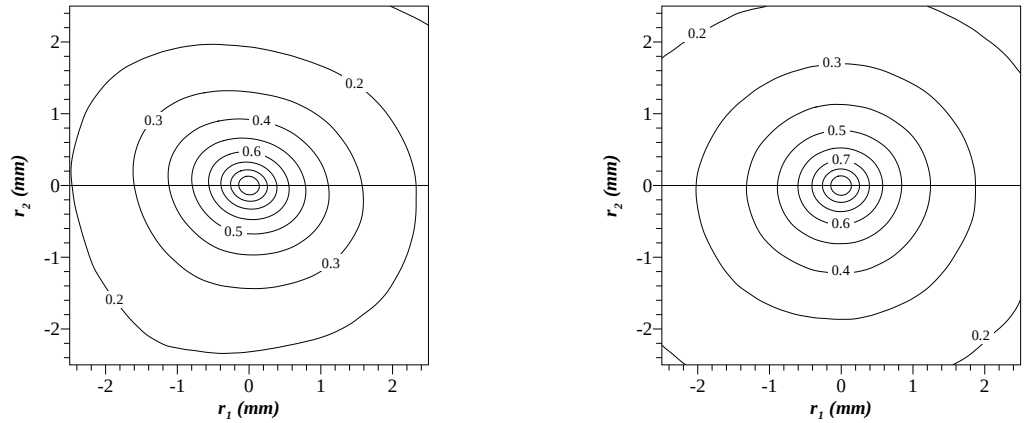

(a) $x = 0.1\ m$

(b) $x = 0.25\ m$

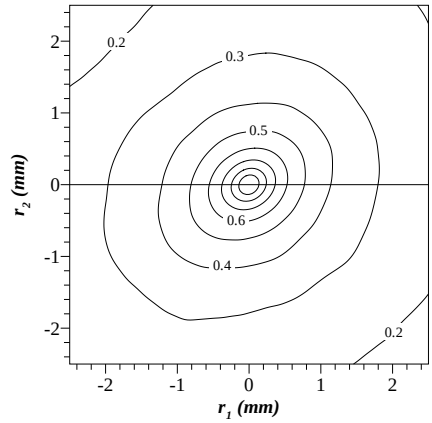

(c) $x = 0.5\ m$

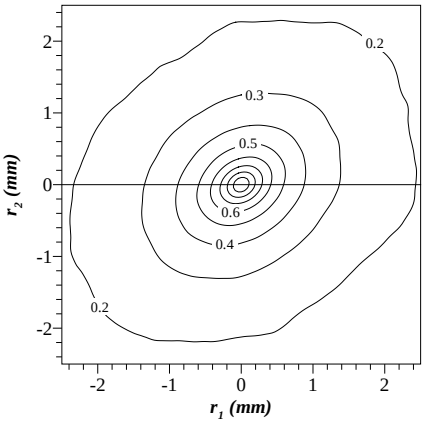

(d) $x = 1.0\ m$

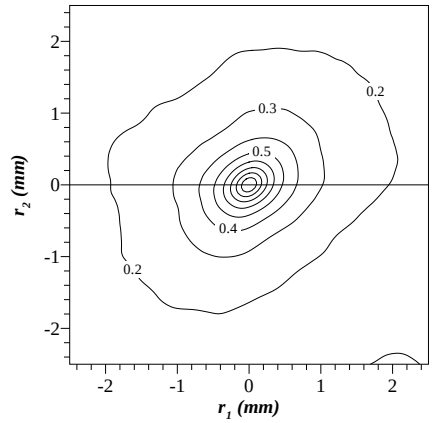

(e) $x = 2.0\ m$

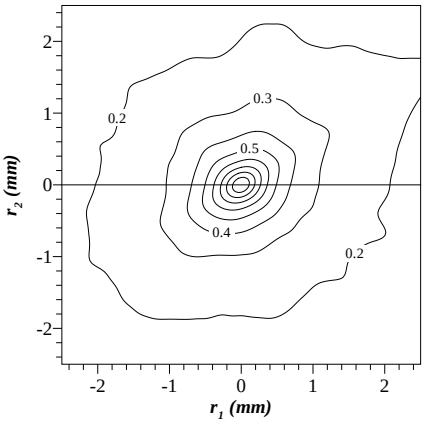

(f) $x = 4.0\ m$

Figure 4.12: Two-point correlation contours of the fluctuating scalar field for $Re = 10000$ and nozzle diameter $D = 9.4\ mm$ at the indicated distances downstream from the point release.

boundary layers.

The characteristic elliptical shape exhibited by the two-point correlation contours indicates anisotropic behavior. Although less severe anisotropic conditions exist near the point release in select instances (high Reynolds numbers and large injection length scales), the distinct characteristic shape develops for low Reynolds numbers and small injection length scales. The anisotropic conditions that exist close to the point release appear to be a result of the tracer injection method and not mean velocity shear. The iso-kinetic release of the tracer preferentially aligns the scalar filaments in the streamwise direction. As a result, the major axis of the elliptical shape is aligned in the streamwise direction and the minor axis is aligned in the wall-normal direction. As the scalar field is advected downstream, the effects of the injection method diminish and the behavior of the scalar field is dominated by the mean velocity shear. The scalar filaments begin aligning with the mean velocity gradient and the characteristic oval shape tilts in the direction of the mean velocity shear. The one-dimensional analysis cannot capture this anisotropic condition because the behavior is not oriented along the streamwise or wall-normal directions. The results of the two-point correlation contours indicate that anisotropic conditions (i.e. the tilted asymmetric elliptical shape) develop as a consequence of the mean velocity shear as reported by Tavoularis & Corrsin (1981).

4.2 Three-Point Correlations of the Concentration Fluctuations

4.2.1 Configuration of Mydlarski & Warhaft (1998)

The three-point correlation contours of the fluctuating scalar field are calculated using the spatial configuration developed by Mydlarski & Warhaft (1998) (refer to section 3.3.1 and Figure 3.5). The appropriate separation distance, Y, associated with this geometry was selected based on the integral length scale such that $Y/l_L \simeq 0.05$. Mydlarski & Warhaft (1998) report data for $Y/l_L = 0.043$, 0.051, and 0.13. In general, the streamwise and wall-normal integral length scales were the same order of magnitude (see Table 4.1). However, for significant differences in each direction, the lower value of l_L was selected to calculate the

appropriate separation distance. Table 4.2 summarizes the separation distance associated with each case analyzed in the current study.

Table 4.2: The separation distance associated with the three-point correlation of the concentration fluctuations.

$x(m)$	$Re = 5000$ $D = 4.7\ mm$ $Y(mm)$	$Re = 10000$ $D = 2.2\ mm$ $Y(mm)$	$Re = 10000$ $D = 4.7\ mm$ $Y(mm)$	$Re = 10000$ $D = 9.4\ mm$ $Y(mm)$	$Re = 20000$ $D = 4.7\ mm$ $Y(mm)$
0.1	0.078	0.052	0.065	0.065	0.052
0.25	0.078	0.052	0.065	0.065	0.065
0.5	0.065	0.039	0.052	0.065	0.065
1.0	0.065	0.039	0.052	0.065	0.052
2.0	0.065	0.039	0.065	0.065	0.078
4.0	0.052	0.052	0.078	0.065	0.104

The three-point correlation contours are illustrated in Figures 4.13 through 4.17. The three-point correlation, $\langle \theta_A \theta_B \theta_C \rangle$, is normalized by the negative correlation evaluated at $x_1' = x_2' = 0$ (i.e. the contours represent $-\frac{\langle \theta_A \theta_B \theta_C \rangle}{\langle \theta_A \theta_C^2 \rangle}$). The normalized correlation contour values less than -0.6 (the innermost contours) are represented in each figure as symmetric, concentric, circular shapes. This symmetric shape suggests universal behavior of the fluctuating scalar field for well-correlated points. The size of the circular pattern appears to be a function of the Reynolds number and the downstream distance. Note that the concentric circular pattern constricts as the Reynolds number and the downstream distance increases. This behavior indicates that smaller separation distances are required to maintain a significant correlation between points A, B, and C. Similar trends were noted for the two-point correlation function. There is no discernable trend associated with the size of the symmetric circular pattern and the injection length scale.

For normalized correlation contours greater than -0.6, the circular shape changes. Close to the point release ($x \leq 0.25\ m$), these outermost contours develop a new symmetric shape (note the reflect symmetry relative to $x_1' = 0$ and also relative to $x_2' = 0$). Figures 4.13 (a) &

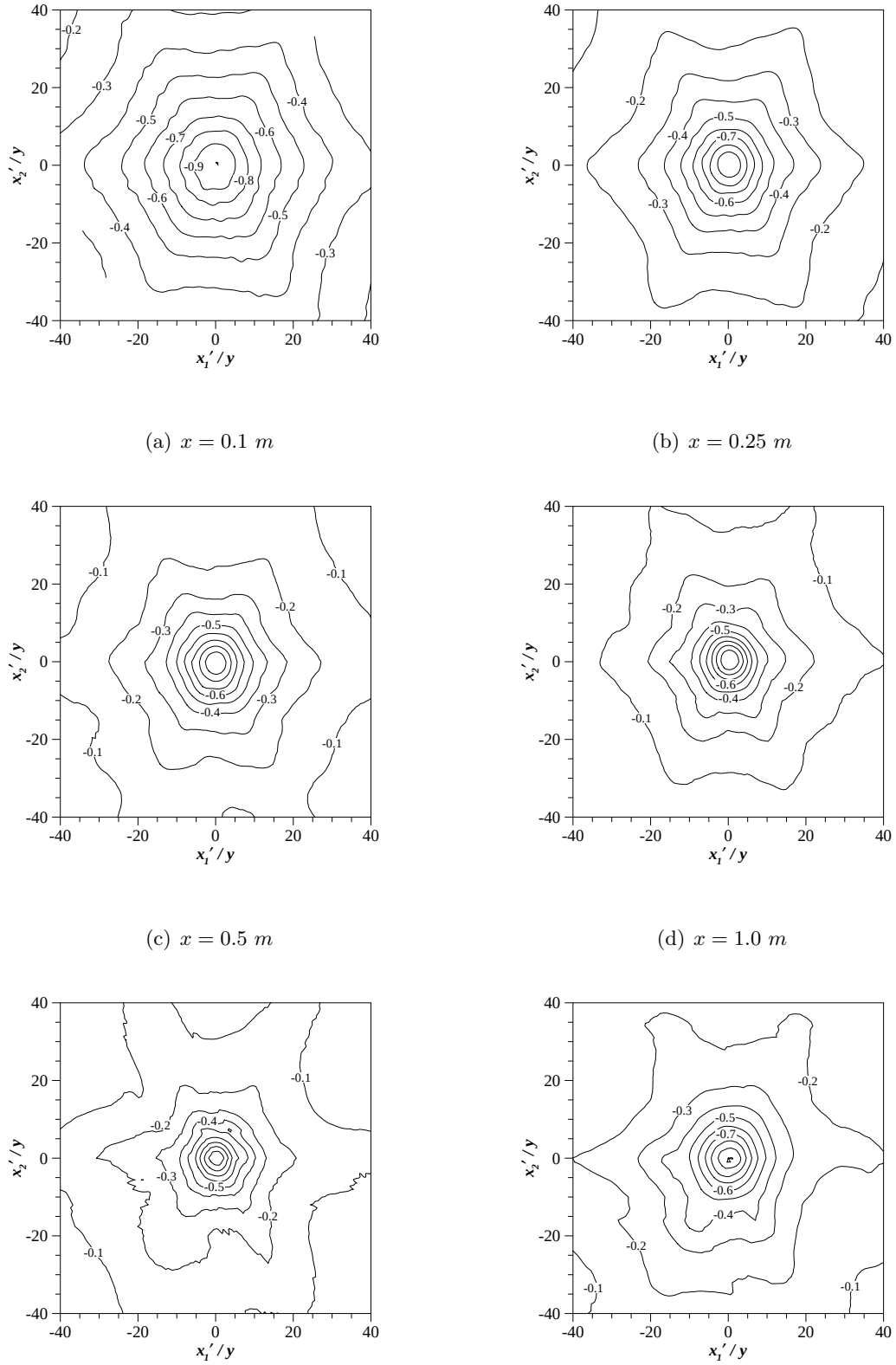

(a) $x = 0.1\ m$

(b) $x = 0.25\ m$

(c) $x = 0.5\ m$

(d) $x = 1.0\ m$

(e) $x = 2.0\ m$

(f) $x = 4.0\ m$

Figure 4.13: Three-point correlation contours of the fluctuating scalar field for $Re = 5000$ and nozzle diameter $D = 4.7\ mm$ at the indicated distances downstream from the point release. Correlation geometry shown in Figure 3.5.

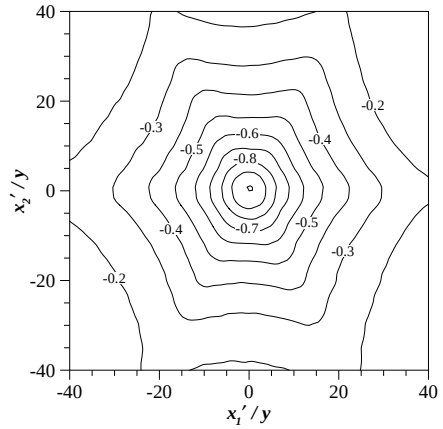

(a) $x = 0.1\ m$

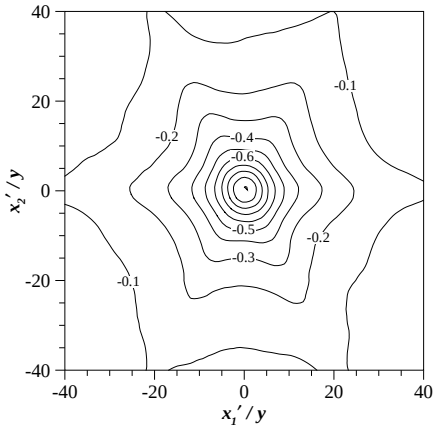

(b) $x = 0.25\ m$

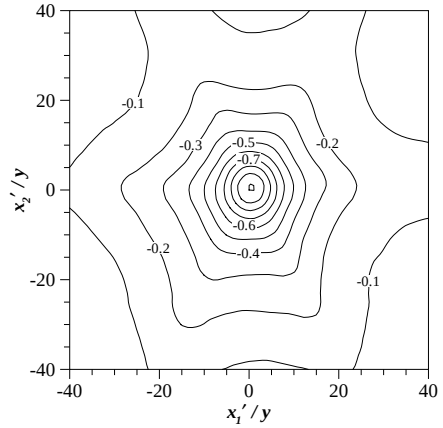

(c) $x = 0.5\ m$

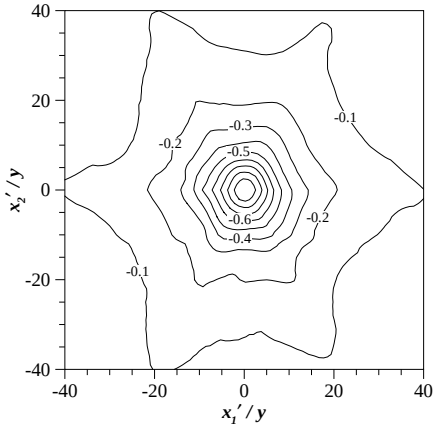

(d) $x = 1.0\ m$

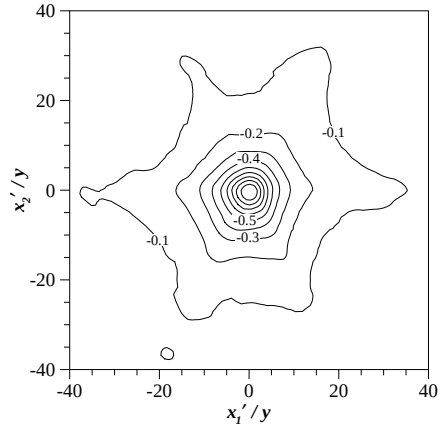

(e) $x = 2.0\ m$

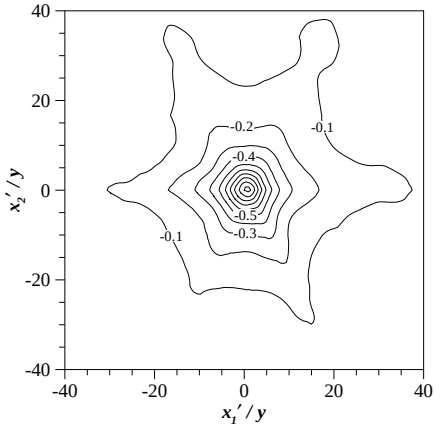

(f) $x = 4.0\ m$

Figure 4.14: Three-point correlation contours of the fluctuating scalar field for $Re = 10000$ and nozzle diameter $D = 4.7\ mm$ at the indicated distances downstream from the point release. Correlation geometry shown in Figure 3.5.

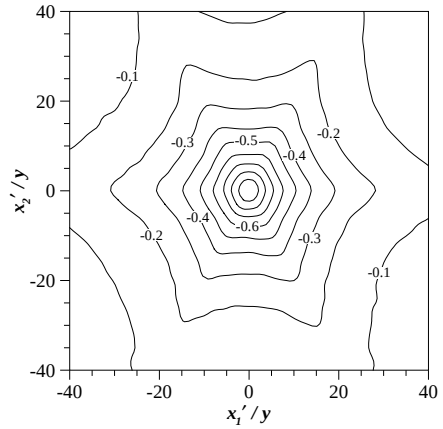

(a) $x = 0.1\ m$

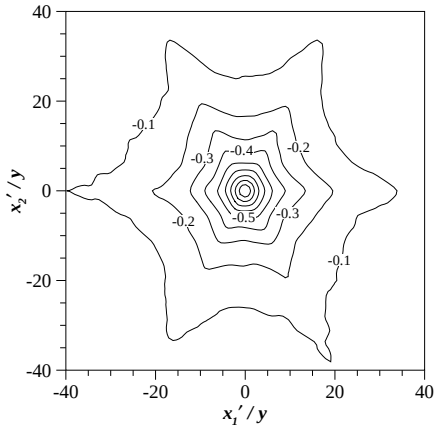

(b) $x = 0.25\ m$

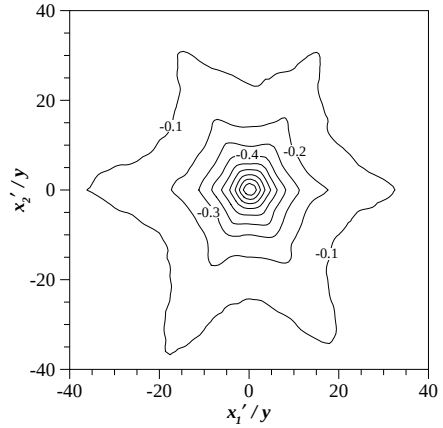

(c) $x = 0.5\ m$

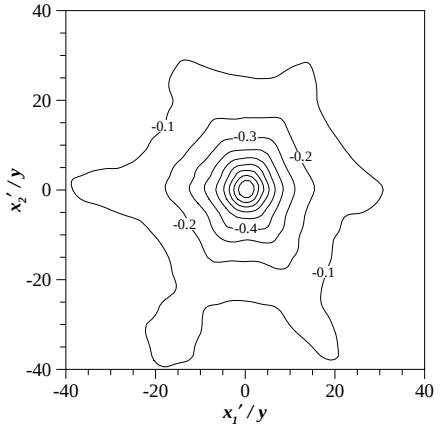

(d) $x = 1.0\ m$

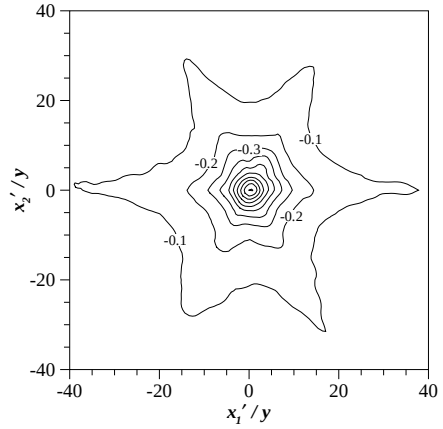

(e) $x = 2.0\ m$

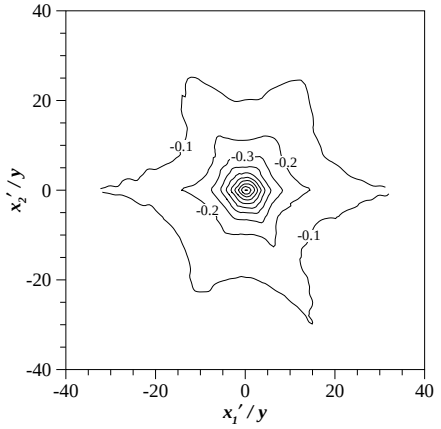

(f) $x = 4.0\ m$

Figure 4.15: Three-point correlation contours of the fluctuating scalar field for $Re = 20000$ and nozzle diameter $D = 4.7\ mm$ at the indicated distances downstream from the point release. Correlation geometry shown in Figure 3.5.

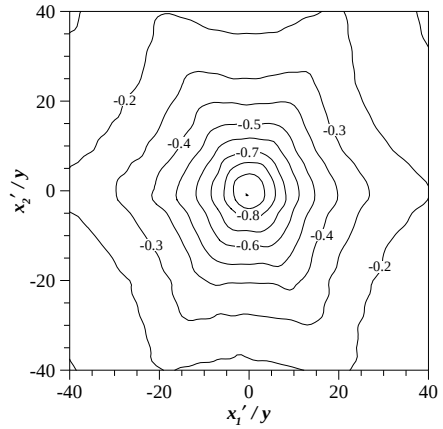

(a) $x = 0.1\ m$

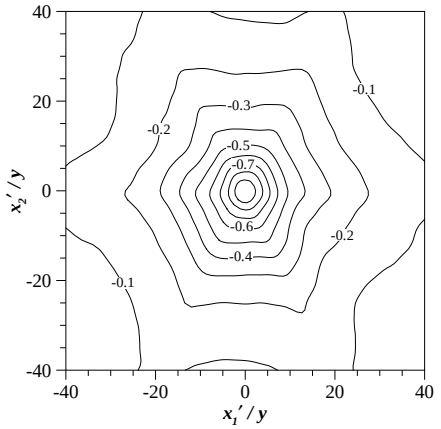

(b) $x = 0.25\ m$

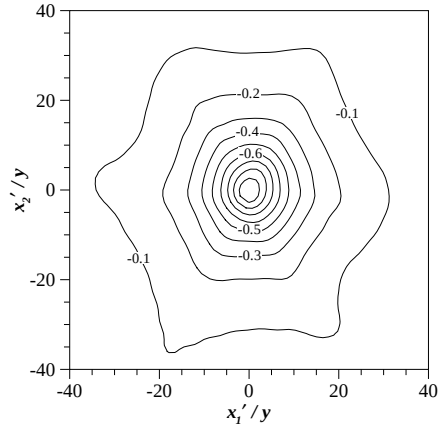

(c) $x = 0.5\ m$

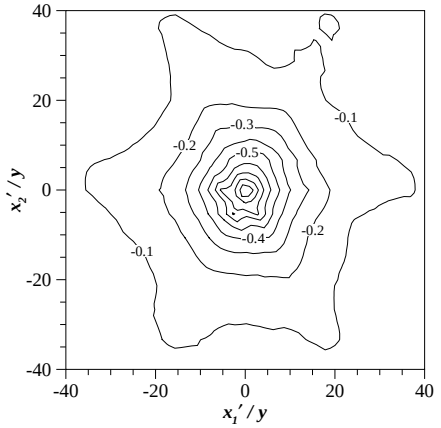

(d) $x = 1.0\ m$

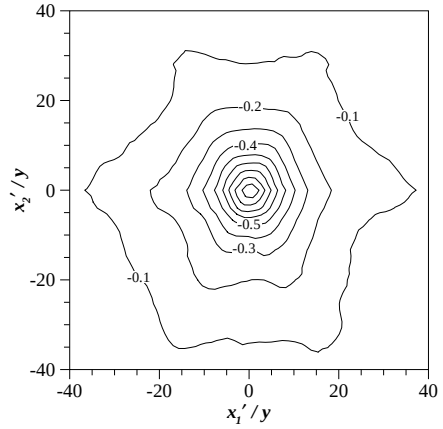

(e) $x = 2.0\ m$

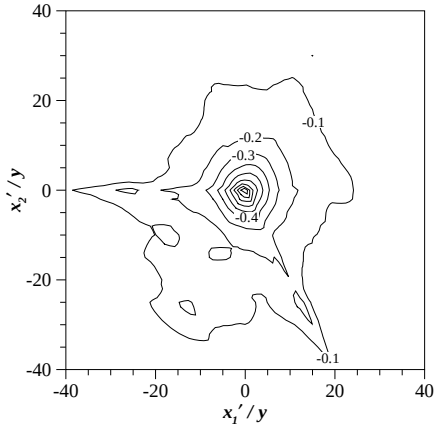

(f) $x = 4.0\ m$

Figure 4.16: Three-point correlation contours of the fluctuating scalar field for $Re = 10000$ and nozzle diameter $D = 2.2\ mm$ at the indicated distances downstream from the point release. Correlation geometry shown in Figure 3.5.

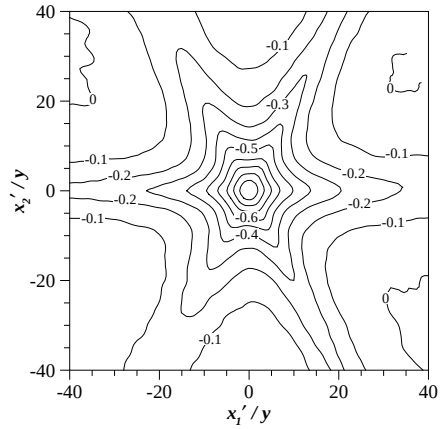

(a) $x = 0.1\ m$

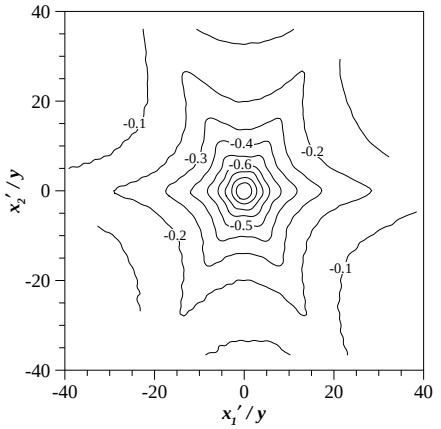

(b) $x = 0.25\ m$

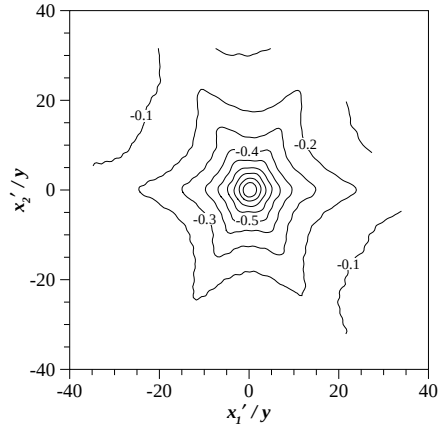

(c) $x = 0.5\ m$

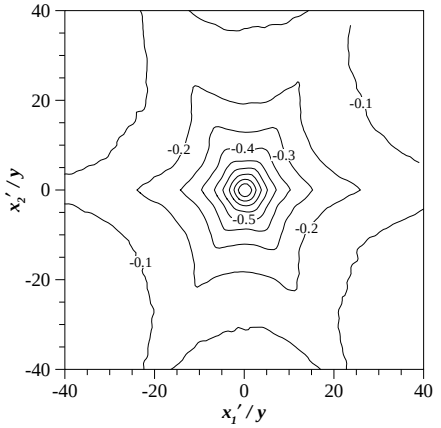

(d) $x = 1.0\ m$

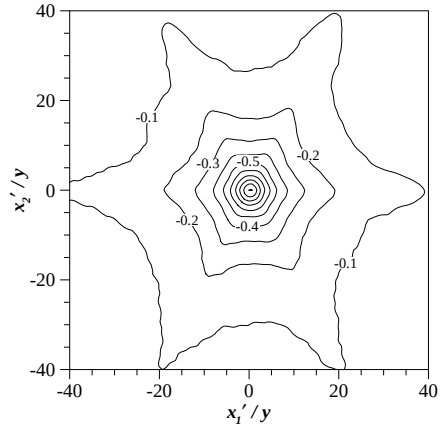

(e) $x = 2.0\ m$

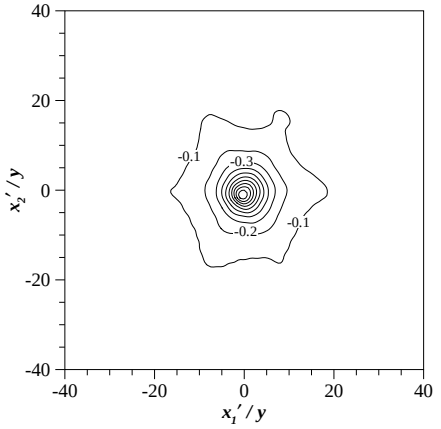

(f) $x = 4.0\ m$

Figure 4.17: Three-point correlation contours of the fluctuating scalar field for $Re = 10000$ and nozzle diameter $D = 9.4\ mm$ at the indicated distances downstream from the point release. Correlation geometry shown in Figure 3.5.

(b) and 4.16 (a) & (b) illustrate that this symmetric shape resembles a hexagon under more severe anisotropic conditions (lower Reynolds number and smaller nozzle diameter). Under less severe anisotropic conditions (higher Reynolds numbers and larger nozzle diameter), the sides of the hexagon develop a concave shape that resembles a symmetric V-shape pattern (refer to Figures 4.15 (a) & (b) and 4.17 (a) & (b)). In agreement with Mydlarski & Warhaft (1998), symmetry exists about the line $x_2 = 2x_1$ (note that the contours are plotted in a rotated coordinate system that transforms the symmetry to the vertical axis (refer to section 2.3.2 and Figure 2.5)). Also, the characteristic V-shape emerges when the less severe anisotropic conditions are a result of the tracer injection method (compare Figures 4.17 (a) and 2.6). As the mean velocity shear acts on the scalar field (i.e. $x > 0.25$ m), the outermost contours become distorted but the symmetry remains intact. Mydlarski & Warhaft (1998) reported that the characteristic V-shape is a consequence of ramp-cliff structures. Since these structures exist in shear flows, as well as shear-free flows, they inferred that the characteristic V-shape will also be observed in both types of flow. The results of the current study indicate that the V-shape emerges but does not exhibit all the properties reported by Mydlarski & Warhaft (1998).

Mydlarski & Warhaft (1998) concluded that the three-point correlation function should become zero when points A, B, and C form an equilateral triangle. The current results do not reflect this condition. In order to remove the slow drifts associated with cold wire probes in the wind tunnel, the experimental data collected by Mydlarski & Warhaft (1998) was obtained in terms of scalar differences between points A, B, and C. As a result, the following structure function was defined to deduce the three-point correlation function:

$$S = \frac{1}{16}\langle 3(\theta_B + \theta_C - 2\theta_A)(\theta_B - \theta_C)^2 - \frac{1}{3}(\theta_B + \theta_C - 2\theta_A)^3 \rangle \tag{4.1}$$

The following form of the structure function can be obtained by expanding the polynomials in equation 4.1:

$$S = \langle \theta_A \theta_B \theta_C \rangle + \frac{1}{3}\langle \theta_A^3 + \theta_B^3 + \theta_C^3 \rangle - \frac{1}{12}\langle (\theta_A + \theta_B)^2 + (\theta_A + \theta_C)^2 + (\theta_C + \theta_B)^2 \rangle \tag{4.2}$$

Note that equation 4.2 is permutationally symmetric because points A, B, and C can be

arbitrarily exchanged and the structure function remains unaltered. In addition, by assuming even symmetry in x (due to Taylor's frozen turbulence hypothesis) and odd symmetry in y (due to the nearly isotropic velocity field), equation 4.2 reduces to:

$$S = \langle \theta_A \theta_B \theta_C \rangle + \frac{1}{6} \langle \theta_A^3 + \theta_B^3 + \theta_C^3 \rangle \tag{4.3}$$

where $\frac{1}{6} \langle \theta_A^3 + \theta_B^3 + \theta_C^3 \rangle$ represents the scalar skewness, which should be zero for the data collected by Mydlarski & Warhaft (1998). Thus, they measured the terms on the R.H.S. of equation 4.1 to equivalently determine the three-point correlation function. The symmetries that were imposed on the structure function to derive the three-point correlation function dictate that $\langle \theta_A \theta_B \theta_C \rangle = 0$ when points A, B, and C form an equilateral triangle. This condition is an artifact of the imposed symmetry required to derive the three-point correlation function. In the current study, the scalar fluctuations at each point were directly measured using the PLIF technique described in section 3.1.2. Therefore, it was unnecessary to enforce symmetry to derive the three-point correlation function (i.e. the three-point correlation function was measured directly). Furthermore, odd symmetry in the y direction does not exist in the current data set. If the scalar gradient is flipped, the magnitude of the third-order statistics will change (due to the mean velocity gradient). In addition, the scalar field in the current study is more intermittent than the temperature gradient analyzed by Mydlarski & Warhaft (1998). Dasi (2004) reported that the scalar skewness associated with the data in the current study is not zero, which is not the case for Mydlarski & Warhaft (1998). Hence, the effects of scalar skewness and intermittency may explain the "less distinct" V-shape. Additional studies examining the effects of scalar skewness and intermittency on the behavior of the characteristic V-shape may provide insight to the different observations.

4.2.2 Configuration Based on the Shape Function

The three-point correlation of the fluctuating scalar field is calculated based on the geometric configurations described by Celani & Vergassola (2001) (refer to section 3.3.2). Equation 3.4 indicates that the three-point correlation function depends on the size, shape, and orientation of the triangle defined by the three points. This study analyzes an isosceles

and a collinear geometric configuration (refer to Figures 3.6 and 3.7). The shape factor, $f(\chi, w)$, varies depending on the geometric configuration of the three points. However, the shape factor remains constant for a specified three-point geometry. Thus, the shape factor parameters, w and χ, remain constant as the specified configuration is rotated, translated, and dilated. The constant shape factor parameters associated with the isosceles geometric configuration are $w = 0.866$ and $\chi = 0$. The constant shape factor parameters for the collinear configuration are $w = 0$ and $\chi = \frac{\pi}{6}$. The effects of the size and orientation of the three-point correlation function can be evaluated because the shape factor remains constant for a specified geometric configuration. The analysis focuses on the inertial-convective range, which is defined as $l_L \gg R \gg \eta$. An average integral length scale of 1.5 mm was used to approximate the inertial-convective range associated with each Reynolds number. Table 4.3 contains the appropriate range of values that describe the inertial-convective regime.

Table 4.3: The inertial-convective range for each Reynolds number.

Reynolds number	Inertial-Convective Range
5000	$2 > R/\eta > 1$
10000	$3.6 > R/\eta > 1$
20000	$5.2 > R/\eta > 1$

4.2.2.1 Isosceles Configuration

The calculation methods used to produce the following results are illustrated in Figure 3.8 (a). The three-point correlation function associated with the isosceles geometric configuration is illustrated in Figures 4.18 through 4.22. The three-point correlation function is normalized by the correlation evaluated at $R = 0$ (i.e. $\langle \theta_A \theta_B \theta_C \rangle|_{R=0}$). For any specified Reynolds number, nozzle diameter, and downstream distance, the three-point correlation function is approximately equal for each rotation angle. This indicates that the three-point correlation function is independent of the angle between the three-point geometry and the mean scalar gradient.

The three-point correlation function can also be examined in terms of the scaling exponent associated with the global size variable in the inertial-convective regime. The scaling

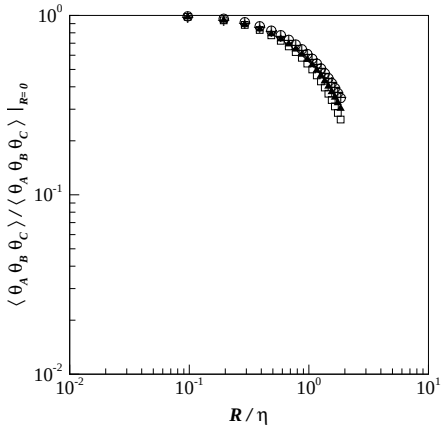

(a) $x = 0.1\ m$

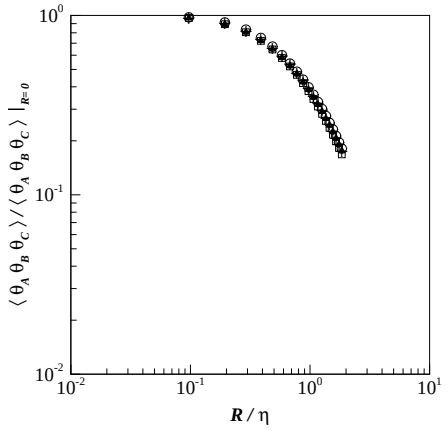

(b) $x = 0.25\ m$

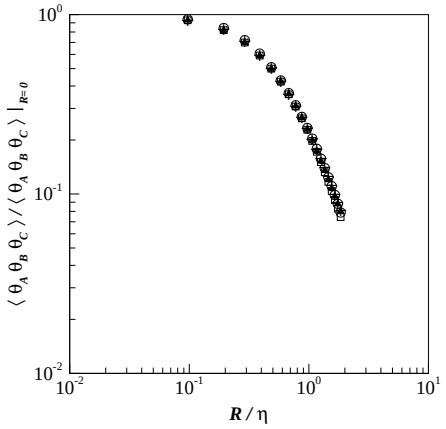

(c) $x = 0.5\ m$

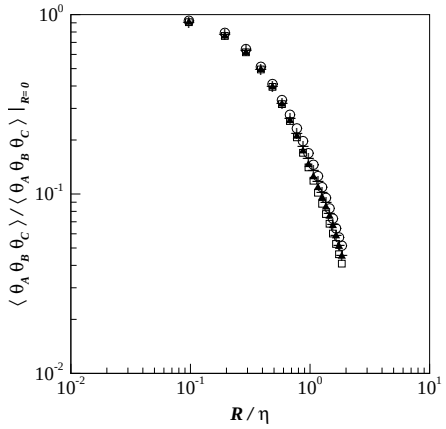

(d) $x = 1.0\ m$

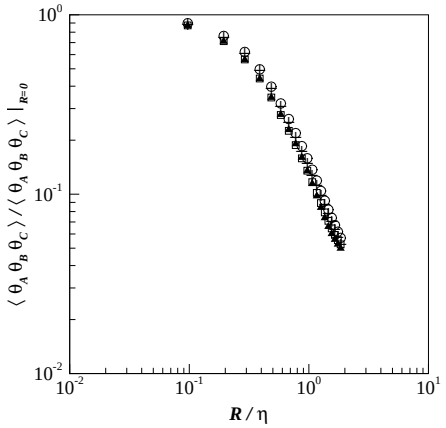

(e) $x = 2.0\ m$

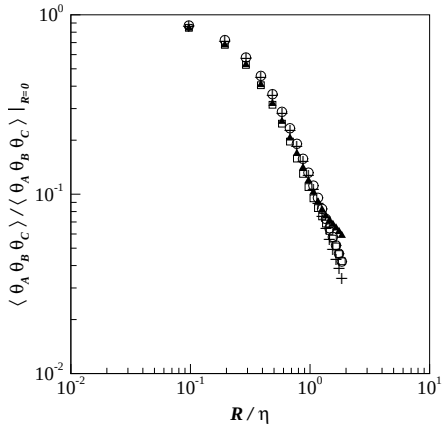

(f) $x = 4.0\ m$

Figure 4.18: Three-point correlation function of the fluctuating scalar field calculated using an isosceles geometric configuration for $Re = 5000$ and nozzle diameter $D = 4.7\ mm$. Data shown for 0° rotation (▲), 90° rotation (○), 180° rotation (□), and 270° rotation (+), at the indicated distances downstream from the point release.

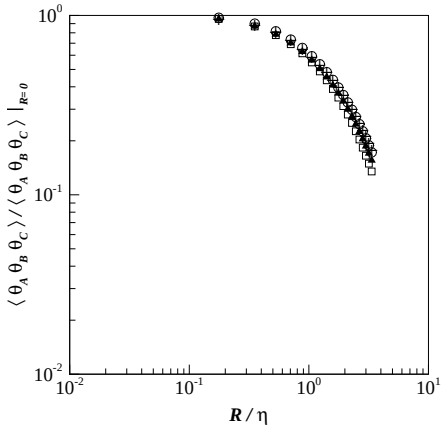

(a) $x = 0.1\ m$

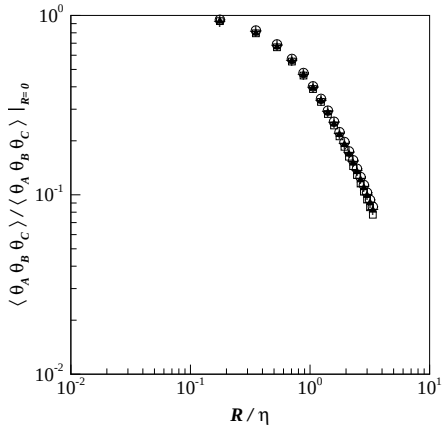

(b) $x = 0.25\ m$

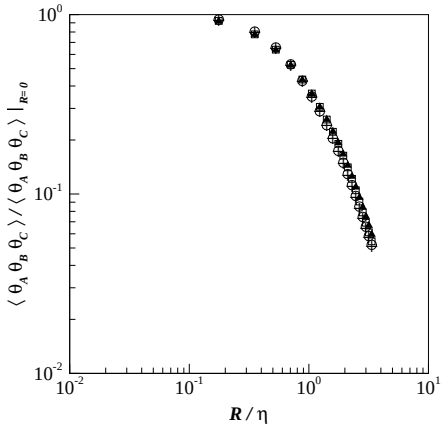

(c) $x = 0.5\ m$

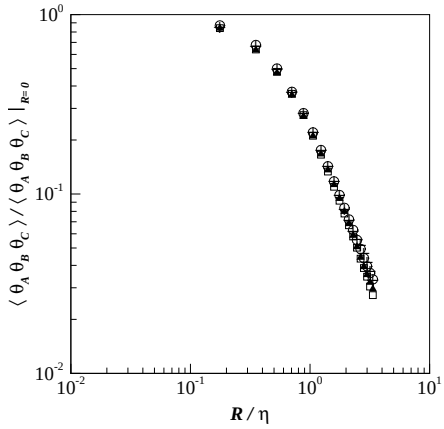

(d) $x = 1.0\ m$

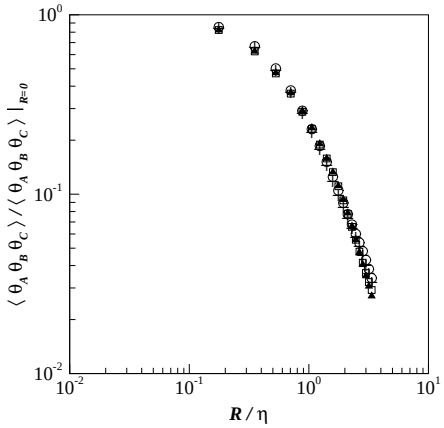

(e) $x = 2.0\ m$

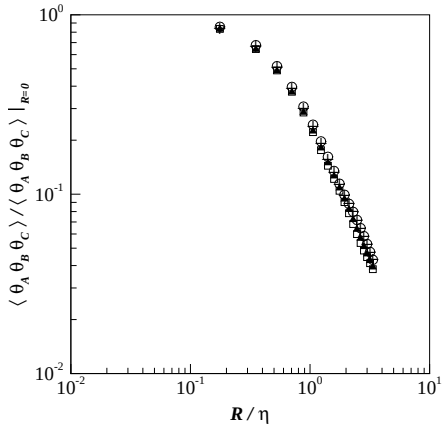

(f) $x = 4.0\ m$

Figure 4.19: Three-point correlation function of the fluctuating scalar field calculated using an isosceles geometric configuration for $Re = 10000$ and nozzle diameter $D = 4.7\ mm$. Data shown for 0° rotation (▲), 90° rotation (○), 180° rotation (□), and 270° rotation (+), at the indicated distances downstream from the point release.

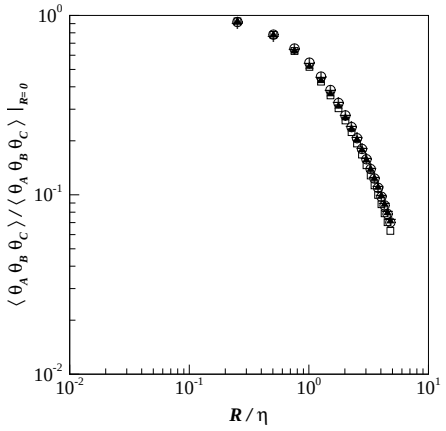

(a) $x = 0.1\ m$

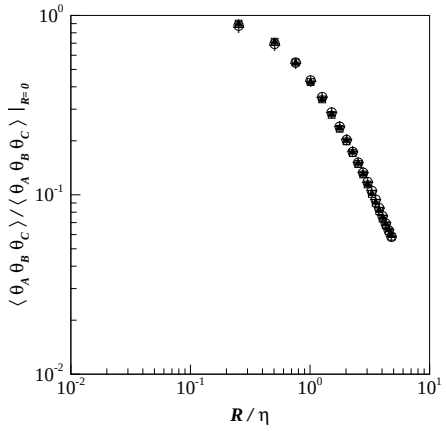

(b) $x = 0.25\ m$

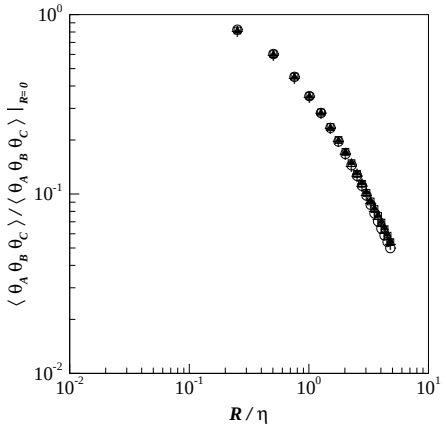

(c) $x = 0.5\ m$

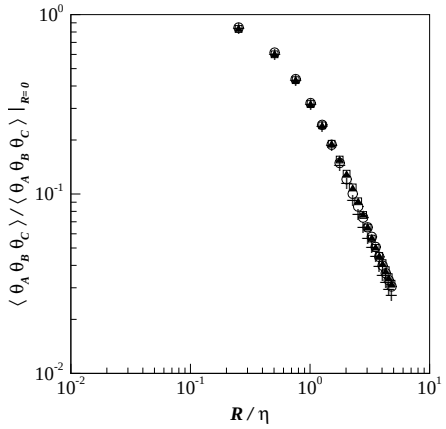

(d) $x = 1.0\ m$

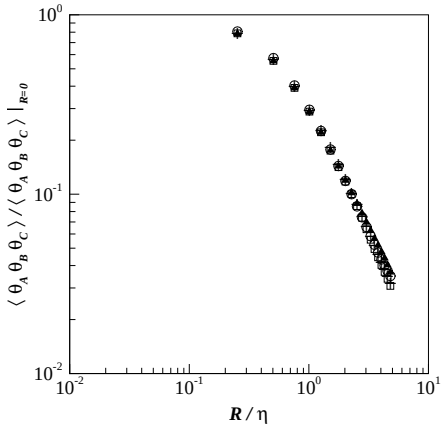

(e) $x = 2.0\ m$

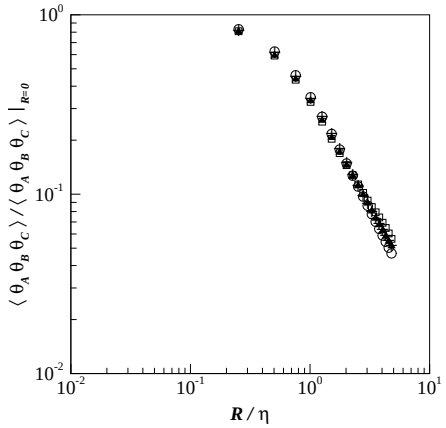

(f) $x = 4.0\ m$

Figure 4.20: Three-point correlation function of the fluctuating scalar field calculated using an isosceles geometric configuration for $Re = 20000$ and nozzle diameter $D = 4.7\ mm$. Data shown for 0° rotation (▲), 90° rotation (○), 180° rotation (□), and 270° rotation (+), at the indicated distances downstream from the point release.

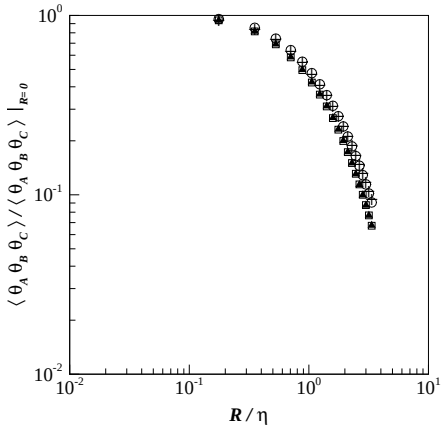

(a) $x = 0.1\ m$

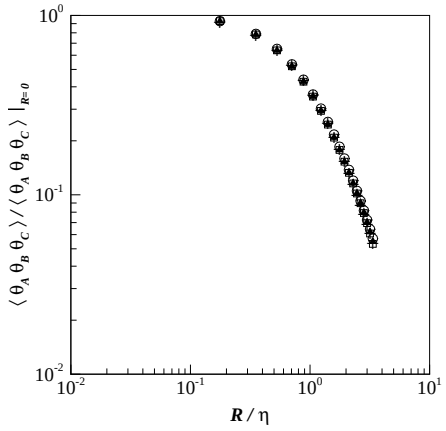

(b) $x = 0.25\ m$

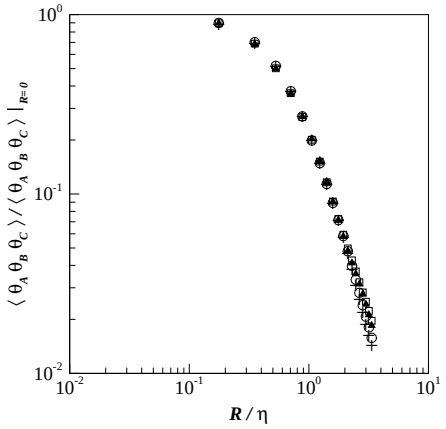

(c) $x = 0.5\ m$

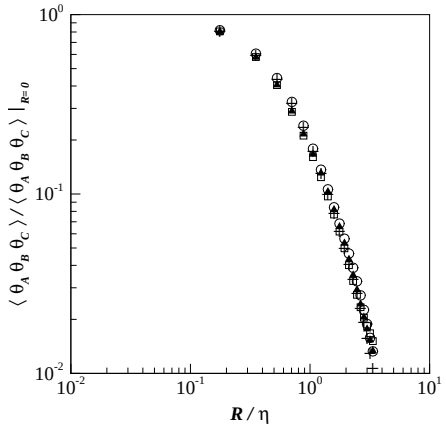

(d) $x = 1.0\ m$

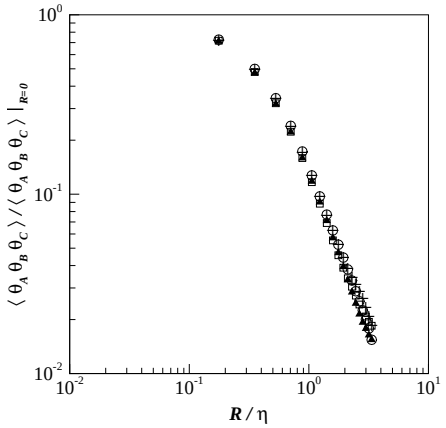

(e) $x = 2.0\ m$

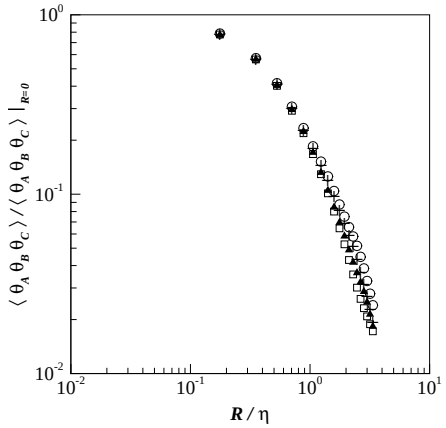

(f) $x = 4.0\ m$

Figure 4.21: Three-point correlation function of the fluctuating scalar field calculated using an isosceles geometric configuration for $Re = 10000$ and nozzle diameter $D = 2.2\ mm$. Data shown for 0° rotation (▲), 90° rotation (○), 180° rotation (□), and 270° rotation (+), at the indicated distances downstream from the point release.

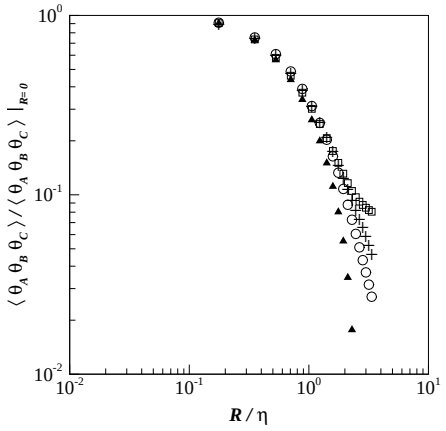

(a) $x = 0.1\ m$

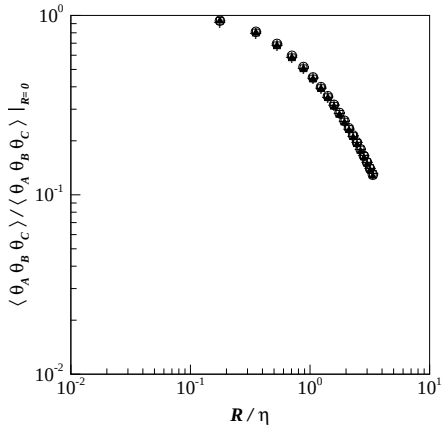

(b) $x = 0.25\ m$

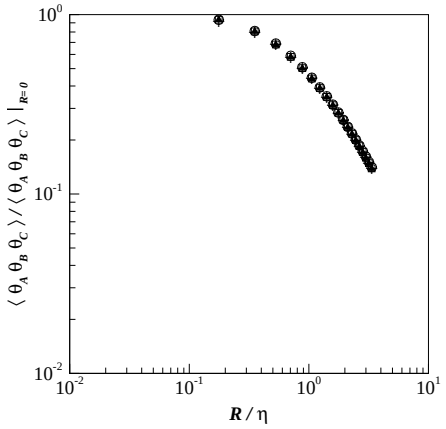

(c) $x = 0.5\ m$

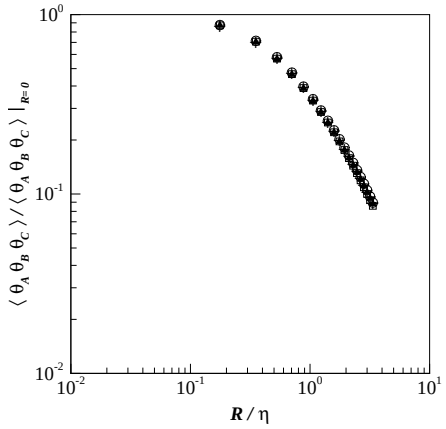

(d) $x = 1.0\ m$

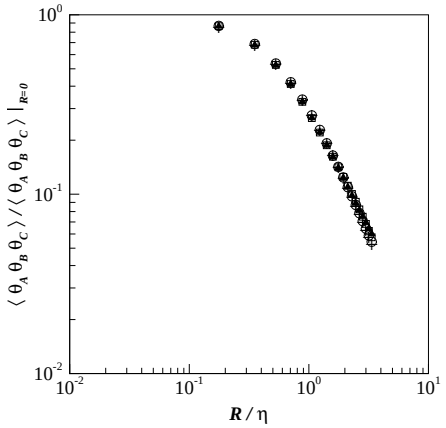

(e) $x = 2.0\ m$

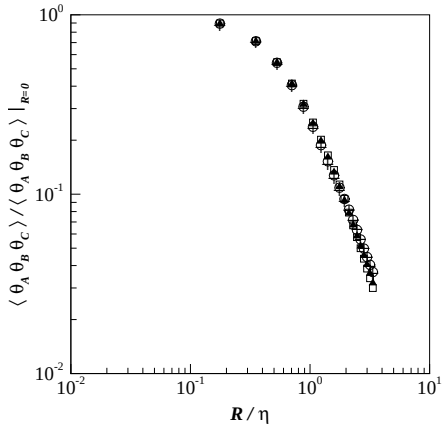

(f) $x = 4.0\ m$

Figure 4.22: Three-point correlation function of the fluctuating scalar field calculated using an isosceles geometric configuration for $Re = 10000$ and nozzle diameter $D = 9.4\ mm$. Data shown for 0° rotation (▲), 90° rotation (○), 180° rotation (□), and 270° rotation (+), at the indicated distances downstream from the point release.

exponents associated with the isosceles geometric configuration are illustrated in Table 4.4. Although the scaling exponents are similar in magnitude, there is no discernable trend suggesting a unique value. Figure 4.23 illustrates the behavior of the scaling exponent at specified downstream distances as a function of the orientation angle, Reynolds number, and injection length scale. For downstream distances close to the point release ($x < 2.0\ m$), the scaling exponent appears independent of the orientation angle. Note that the scaling exponents remain approximately constant as the orientation angle varies (although some dependence is exhibited at $x = 0.1\ m$ for $Re = 10000$ and $D = 9.4\ mm$). A trend emerges that indicates the scaling exponent is independent of the Reynolds number and dependent on the injection length scale at intermediate downstream distances ($0.25\ m \leq x \leq 1.0\ m$) (refer to Figure 4.23 (b), (c), and (d)). Note that the scaling exponent associated with the different Reynolds numbers remains approximately equal. However, the scaling exponents associated with the different injection length scales are distinctly different. As the injection length scale increases, the magnitude of the scaling exponent decreases. Dasi (2004) reported a similar trend regarding the behavior of the scaling exponent associated with an equilateral geometric configuration. At downstream distances farthest from the point release ($x \geq 2.0\ m$), the previously noted trends dissolve. Although the scaling exponents no longer remain constant with respect to the orientation angle, the values remain similar in magnitude.

4.2.2.2 Collinear Configuration

The calculation methods used to produce the following results are illustrated in Figure 3.8 (b). The three-point correlation function associated with the collinear geometric configuration is illustrated in Figures 4.24 through 4.28. The three-point correlation function is normalized by the correlation evaluated at $R = 0$ (i.e. $\langle \theta_A \theta_B \theta_C \rangle|_{R=0}$). The magnitude of the three-point correlation function appears sensitive to the rotation angle of the collinear configuration. In general, the lowest value of the correlation function is associated with the $-45°$ rotation angle and the $90°$ rotation angle. Although there is no clear relationship between the value of the correlation function and the orientation angle, several trends

Table 4.4: Scaling exponent in the inertial-convective range associated with the isosceles geometric configuration.

Description	Rotation	Downstream Distance, x					
		0.1 m	0.25 m	0.5 m	1.0 m	2.0 m	4.0 m
	0°	-1.02	-1.25	-1.67	-1.85	-1.53	-0.99
$Re = 5000$	90°	-0.92	-1.27	-1.73	-1.91	-1.61	-1.77
$D = 4.7\ mm$	180°	-1.17	-1.30	-1.79	-1.93	-1.48	-1.46
	270°	-0.89	-1.29	-1.67	-2.00	-1.63	-2.07
	0°	-1.21	-1.43	-1.71	-1.83	-2.08	-1.58
$Re = 10000$	90°	-1.16	-1.42	-1.76	-1.71	-1.66	-1.44
$D = 4.7\ mm$	180°	-1.32	-1.49	-1.81	-1.82	-2.03	-1.61
	270°	-1.12	-1.43	-1.79	-1.62	-1.66	-1.41
	0°	-1.50	-1.46	-1.31	-1.69	-1.32	-1.23
$Re = 20000$	90°	-1.56	-1.44	-1.42	-1.60	-1.45	-1.34
$D = 4.7\ mm$	180°	-1.62	-1.47	-1.33	-1.69	-1.59	-1.06
	270°	-1.54	-1.43	-1.35	-1.65	-1.55	-1.22
	0°	-1.74	-1.68	-2.06	-2.41	-1.88	-1.90
$Re = 10000$	90°	-1.56	-1.71	-2.29	-2.30	-1.79	-1.73
$D = 2.2\ mm$	180°	-1.73	-1.70	-2.01	-2.31	-1.55	-2.17
	270°	-1.52	-1.75	-2.44	-2.45	-1.52	-1.98
	0°	-4.49	-1.15	-1.06	-1.19	-1.33	-1.86
$Re = 10000$	90°	-2.33	-1.15	-1.04	-1.20	-1.47	-1.64
$D = 9.4\ mm$	180°	-1.19	-1.13	-1.05	-1.23	-1.34	-1.99
	270°	-1.70	-1.12	-1.05	-1.21	-1.49	-1.58

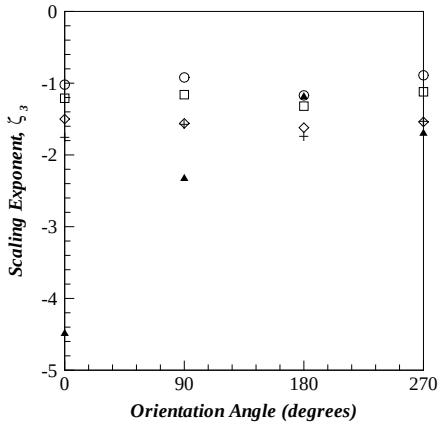

(a) $x = 0.1\ m$

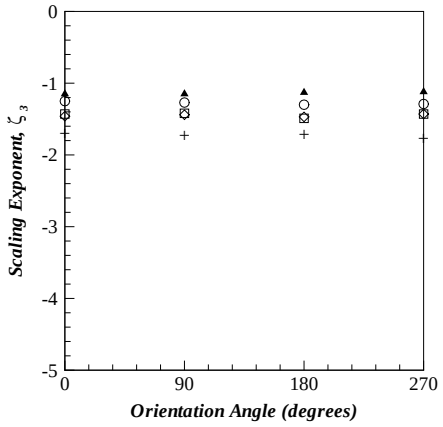

(b) $x = 0.25\ m$

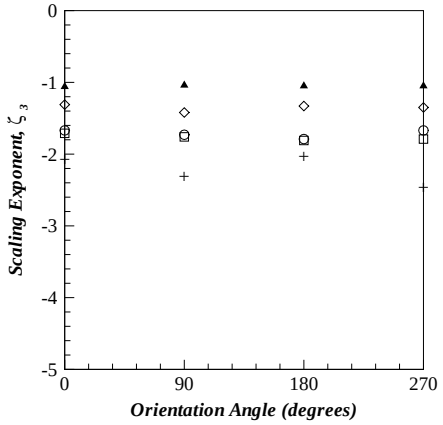

(c) $x = 0.5\ m$

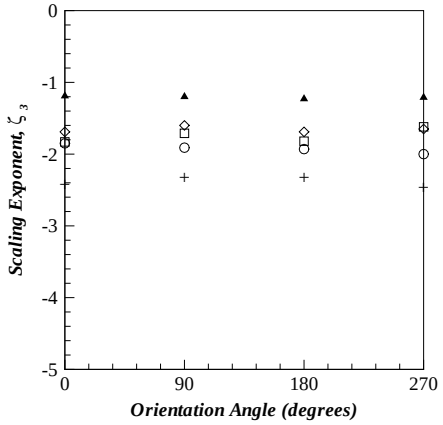

(d) $x = 1.0\ m$

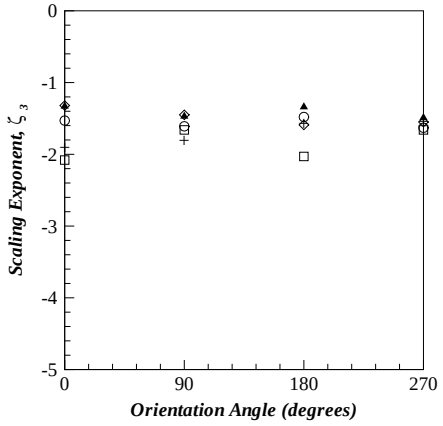

(e) $x = 2.0\ m$

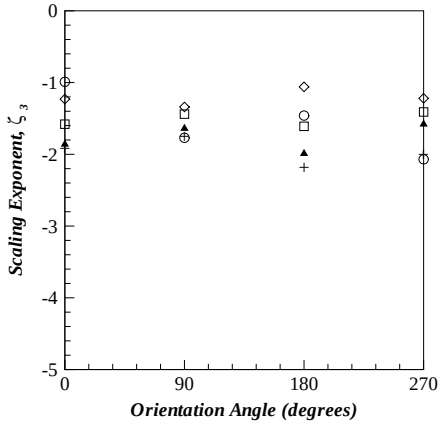

(f) $x = 4.0\ m$

Figure 4.23: The scaling exponent in the inertial-convective range of the three-point correlation of the fluctuating scalar field calculated using an isosceles geometric configuration. Data shown for $Re = 5000$, $D = 4.7\ mm$ (○); $Re = 10000$, $D = 4.7\ mm$ (□); $Re = 20000$, $D = 4.7\ mm$ (◊); $Re = 10000$, $D = 2.2\ mm$ (+); and $Re = 10000$, $D = 9.4\ mm$ (▲) at the indicated distances downstream from the point release.

exist. Close to the point release ($x = 0.1\ m$), the largest correlation values are associated with the 0° rotation angle and the lowest correlation values correspond to the 90° rotation angle. This condition is a result of the tracer injection method. The iso-kinetic release of the tracer preferentially aligns the scalar filaments in the streamwise direction. As a result, the collinear configuration that is aligned in the streamwise direction leads to the largest correlation values. As the scalar field evolves downstream, the effects of the injection method diminish, and the behavior of the scalar field is dominated by the mean velocity shear. The three-point correlation function is approximately equal for each rotation angle at intermediate downstream distances ($0.25\ m \leq x \leq 1.0\ m$). This trend is best illustrated for the highest Reynolds number and the largest injection length scale (refer to Figures 4.26 (b), (c), & (d) and 4.28 (b), (c), & (d)). Therefore, the correlation function is relatively independent of the orientation angle at intermediate downstream distances. The orientation angle affects the value of the three-point correlation function at the farthest downstream distances ($x \geq 2.0\ m$). The affects of the orientation angle appear to have less influence on the correlation values corresponding to the highest Reynolds number and the largest injection length scale. Note that the correlation function curves remain closest in Figures 4.26 (e) & (f) and 4.28 (e) & (f). Additional trends can be examined in terms of the scaling exponent associated with the global size variable.

The scaling exponents associated with the collinear geometric configuration are illustrated in Table 4.5. Although the scaling exponents are similar in magnitude, there is no discernable trend suggesting convergence to a unique value. Figure 4.29 illustrates the behavior of the scaling exponents for the inertial-convective regime at specified downstream distances as a function of the orientation angle, Reynolds number, and injection length scale. For downstream distances close to the point release ($x < 2.0\ m$), the scaling exponent appears independent of the orientation angle. Note that the scaling exponents remain approximately constant as the orientation angle varies (although some dependence is exhibited at $x = 0.1\ m$ for $Re = 10000$ and $D = 9.4\ mm$). At a downstream distance of $x = 0.5\ m$, the data suggests that the scaling exponent is independent of the Reynolds

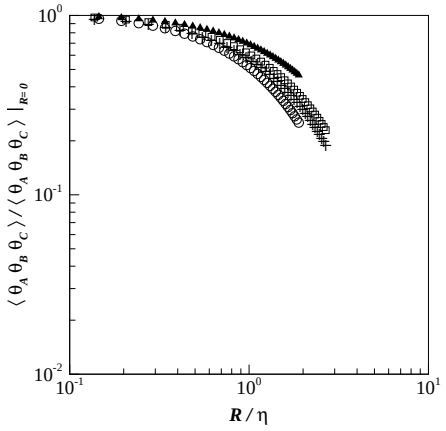

(a) $x = 0.1\ m$

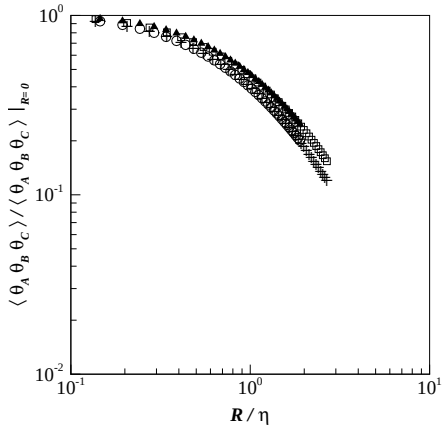

(b) $x = 0.25\ m$

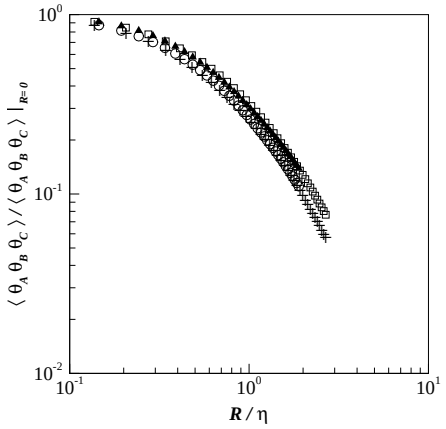

(c) $x = 0.5\ m$

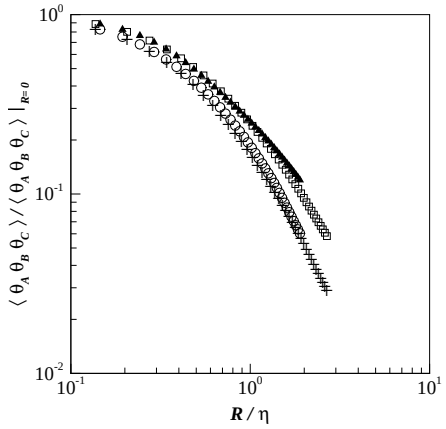

(d) $x = 1.0\ m$

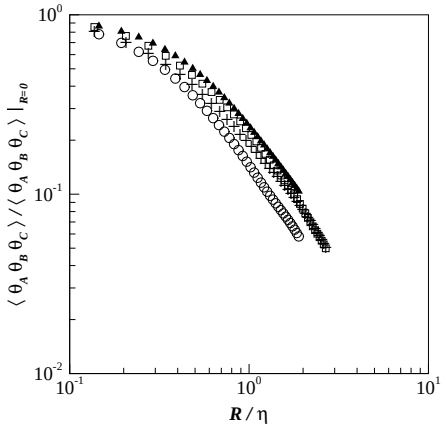

(e) $x = 2.0\ m$

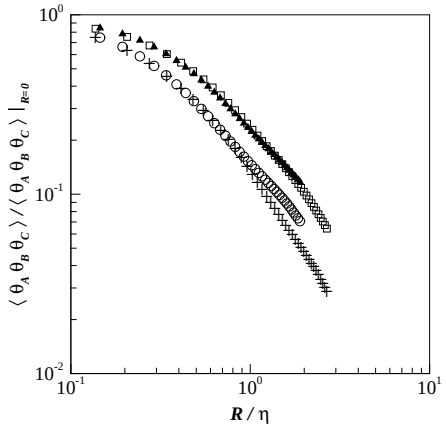

(f) $x = 4.0\ m$

Figure 4.24: Three-point correlation function of the fluctuating scalar field calculated using a collinear geometric configuration for $Re = 5000$ and nozzle diameter $D = 4.7\ mm$. Data shown for $-45°$ rotation (+), $0°$ rotation (▲), $45°$ rotation (□), and $90°$ rotation (○), at the indicated distances downstream from the point release.

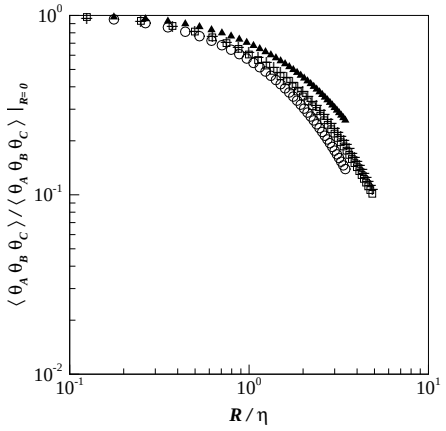

(a) $x = 0.1\ m$

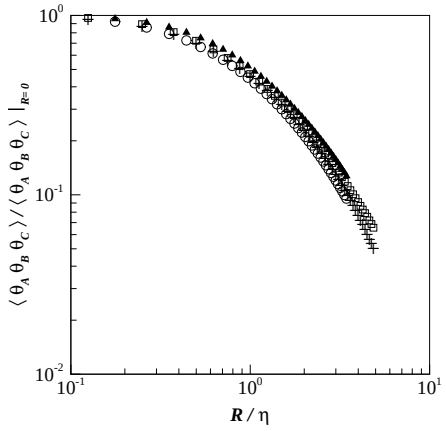

(b) $x = 0.25\ m$

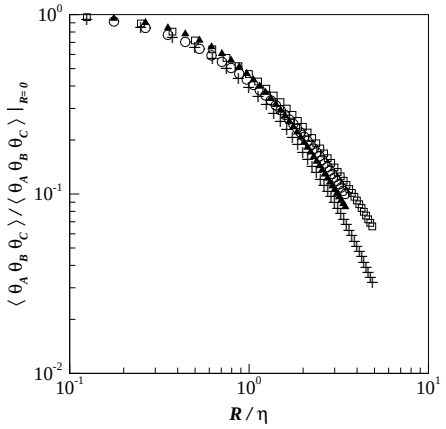

(c) $x = 0.5\ m$

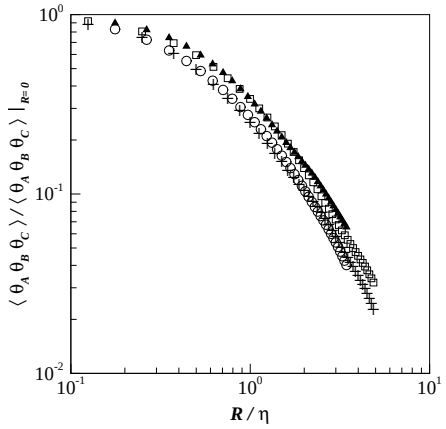

(d) $x = 1.0\ m$

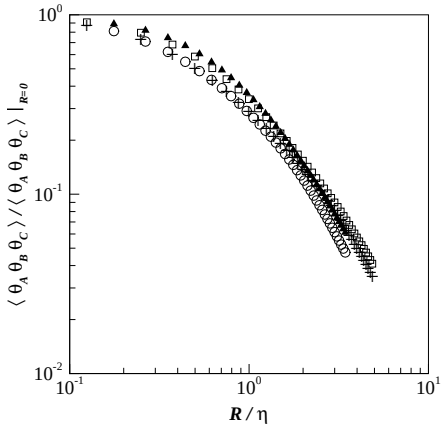

(e) $x = 2.0\ m$

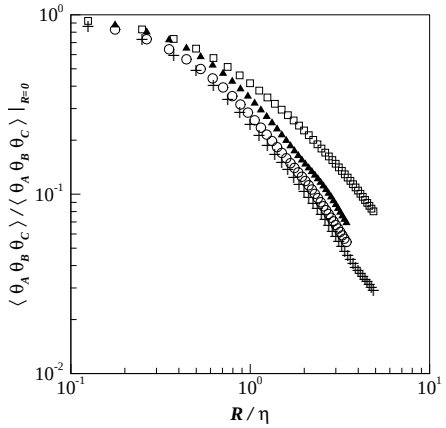

(f) $x = 4.0\ m$

Figure 4.25: Three-point correlation function of the fluctuating scalar field calculated using a collinear geometric configuration for $Re = 10000$ and nozzle diameter $D = 4.7\ mm$. Data shown for $-45°$ rotation (+), $0°$ rotation (▲), $45°$ rotation (□), and $90°$ rotation (○), at the indicated distances downstream from the point release.

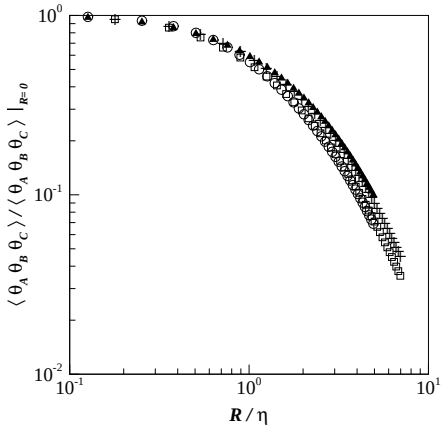

(a) $x = 0.1\ m$

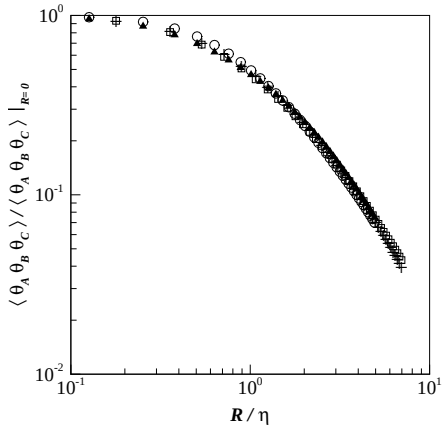

(b) $x = 0.25\ m$

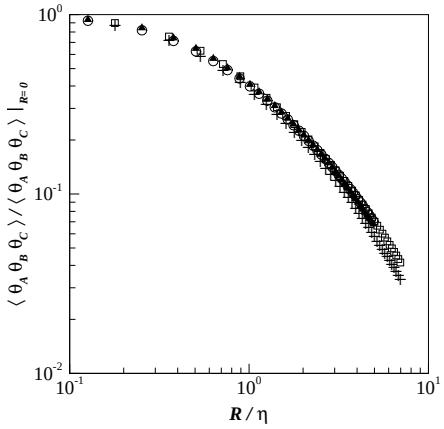

(c) $x = 0.5\ m$

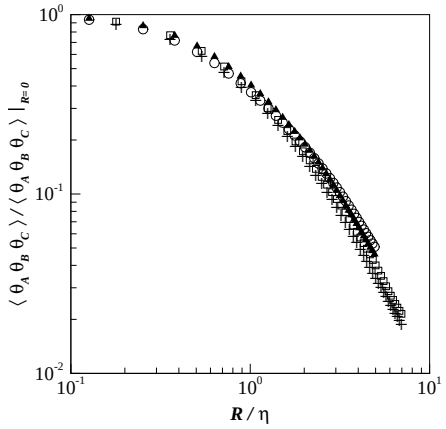

(d) $x = 1.0\ m$

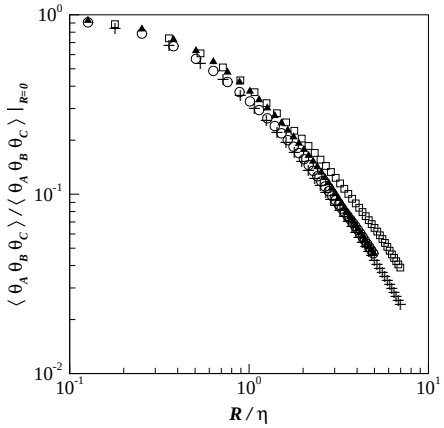

(e) $x = 2.0\ m$

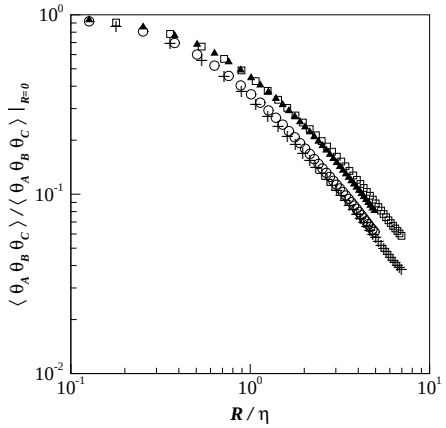

(f) $x = 4.0\ m$

Figure 4.26: Three-point correlation function of the fluctuating scalar field calculated using a collinear geometric configuration for $Re = 20000$ and nozzle diameter $D = 4.7\ mm$. Data shown for $-45°$ rotation (+), $0°$ rotation (▲), $45°$ rotation (□), and $90°$ rotation (○), at the indicated distances downstream from the point release.

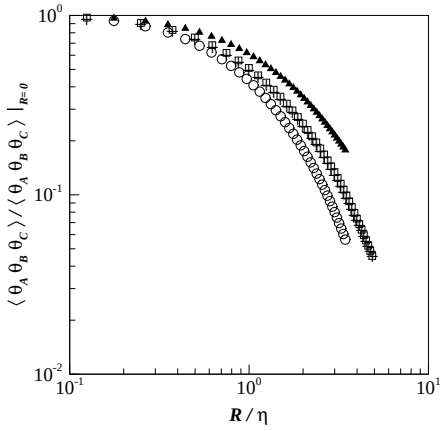

(a) $x = 0.1\ m$

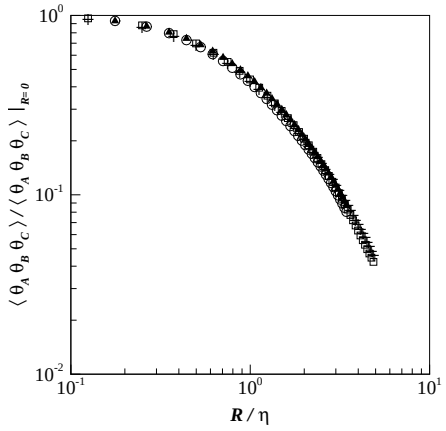

(b) $x = 0.25\ m$

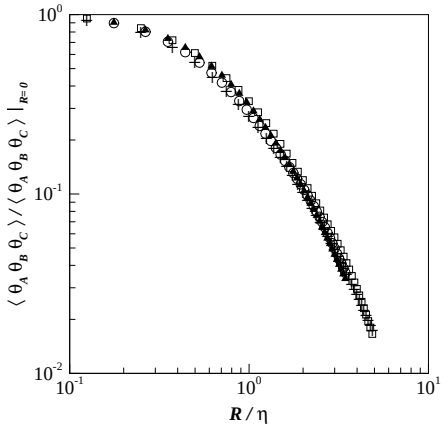

(c) $x = 0.5\ m$

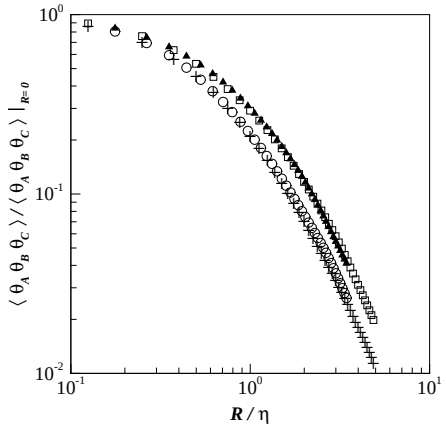

(d) $x = 1.0\ m$

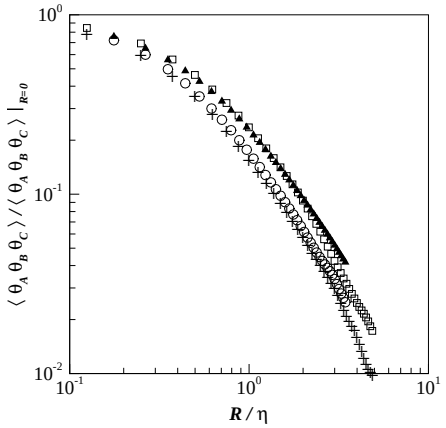

(e) $x = 2.0\ m$

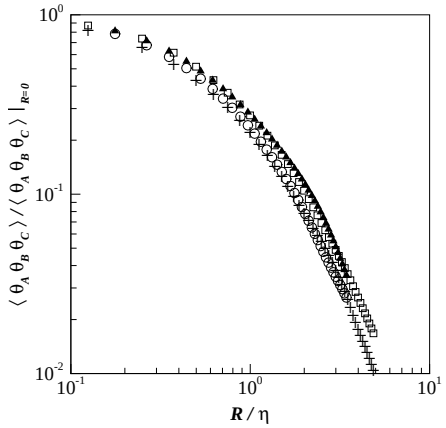

(f) $x = 4.0\ m$

Figure 4.27: Three-point correlation function of the fluctuating scalar field calculated using a collinear geometric configuration for $Re = 10000$ and nozzle diameter $D = 2.2\ mm$. Data shown for $-45°$ rotation (+), $0°$ rotation (▲), $45°$ rotation (□), and $90°$ rotation (○), at the indicated distances downstream from the point release.

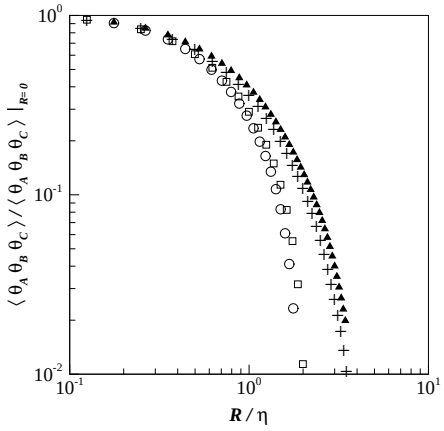

(a) $x = 0.1\ m$

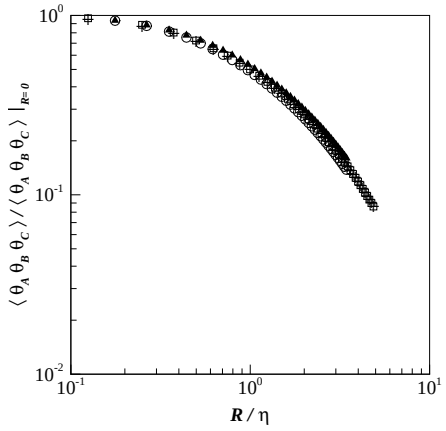

(b) $x = 0.25\ m$

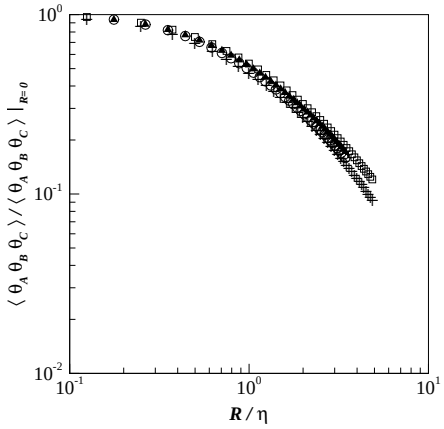

(c) $x = 0.5\ m$

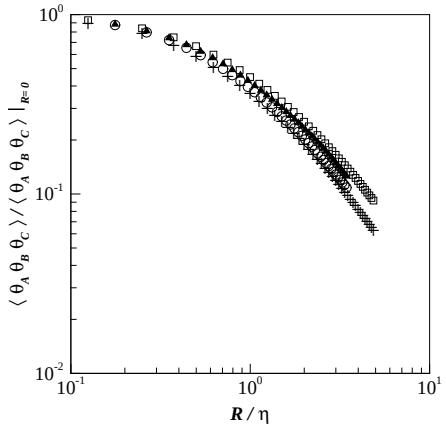

(d) $x = 1.0\ m$

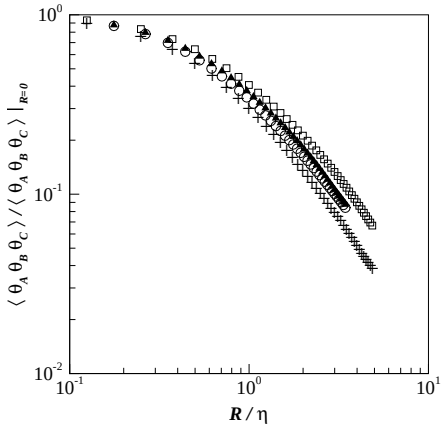

(e) $x = 2.0\ m$

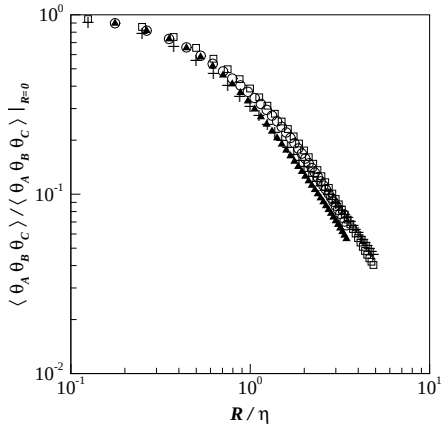

(f) $x = 4.0\ m$

Figure 4.28: Three-point correlation function of the fluctuating scalar field calculated using a collinear geometric configuration for $Re = 10000$ and nozzle diameter $D = 9.4\ mm$. Data shown for $-45°$ rotation (+), $0°$ rotation (▲), $45°$ rotation (□), and $90°$ rotation (○), at the indicated distances downstream from the point release.

number and dependent on the injection length scale (refer to Figure 4.29 (c)). As the injection length scale increases, the magnitude of the scaling exponent decreases. This trend was also observed for the isosceles geometric configuration. The scaling exponents of the collinear configuration remain relatively constant with respect to the orientation angle at the farthest downstream distances. In addition, the values of the scaling exponents remain similar in magnitude.

Table 4.5: Scaling exponent in the inertial-convective range associated with the collinear geometric configuration.

Description	Rotation	Downstream Distance, x					
		0.1 m	0.25 m	0.5 m	1.0 m	2.0 m	4.0 m
	$-45°$	-0.96	-1.13	-1.42	-1.68	-1.20	-1.50
$Re = 5000$	$0°$	-0.63	-1.01	-1.24	-1.19	-1.32	-1.04
$D = 4.7\ mm$	$45°$	-0.85	-1.01	-1.35	-1.41	-1.42	-1.19
	$90°$	-1.14	-1.09	-1.39	-1.81	-1.40	-1.15
	$-45°$	-1.03	-1.30	-1.51	-1.35	-1.23	-1.36
$Re = 10000$	$0°$	-0.87	-1.20	-1.49	-1.33	-1.51	-1.26
$D = 4.7\ mm$	$45°$	-1.07	-1.21	-1.22	-1.59	-1.28	-1.01
	$90°$	-1.24	-1.32	-1.25	-1.61	-1.56	-1.34
	$-45°$	-1.40	-1.38	-1.31	-1.66	-1.31	-1.15
$Re = 20000$	$0°$	-1.37	-1.36	-1.29	-1.61	-1.52	-1.21
$D = 4.7\ mm$	$45°$	-1.50	-1.28	-1.20	-1.54	-1.23	-1.09
	$90°$	-1.54	-1.37	-1.20	-1.43	-1.32	-1.18
	$-45°$	-1.41	-1.35	-1.71	-1.81	-1.59	-1.70
$Re = 10000$	$0°$	-1.10	-1.41	-1.93	-1.78	-1.42	-1.76
$D = 2.2\ mm$	$45°$	-1.40	-1.43	-1.73	-1.63	-1.75	-1.79
	$90°$	-1.78	-1.39	-1.73	-1.73	-1.56	-2.00
	$-45°$	-2.91	-1.05	-0.99	-1.10	-1.31	-1.15
$Re = 10000$	$0°$	-2.48	-1.02	-0.93	-1.02	-1.24	-1.41
$D = 9.4\ mm$	$45°$	-7.42	-1.06	-0.91	-0.99	-1.09	-1.45
	$90°$	-8.74	-1.08	-0.97	-1.09	-1.17	-1.47

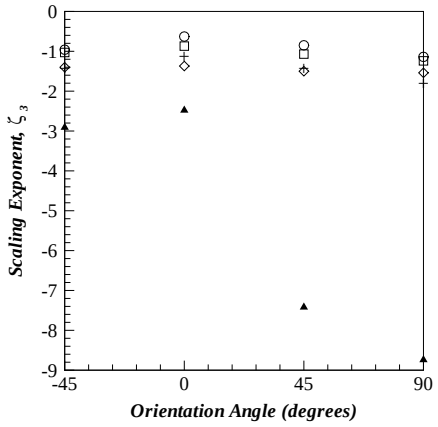

(a) $x = 0.1\ m$

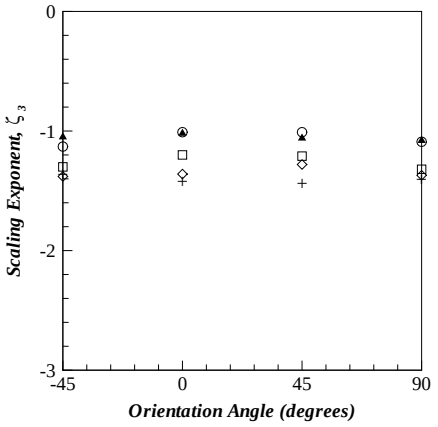

(b) $x = 0.25\ m$

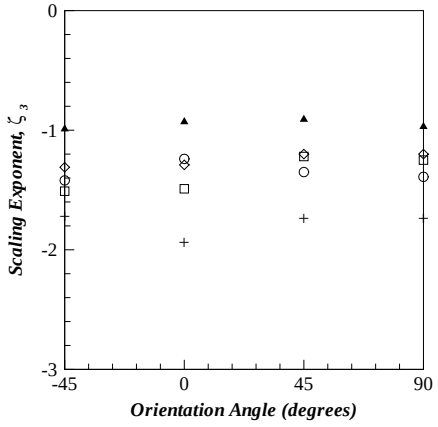

(c) $x = 0.5\ m$

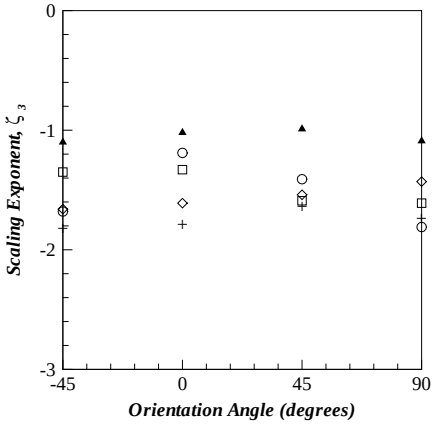

(d) $x = 1.0\ m$

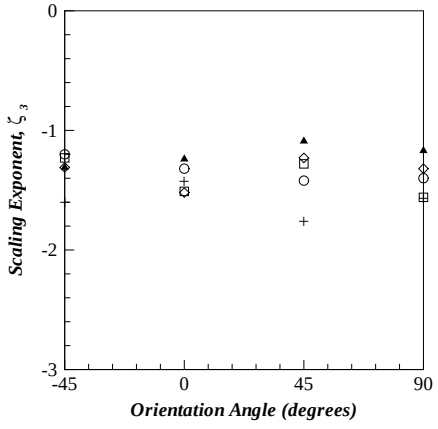

(e) $x = 2.0\ m$

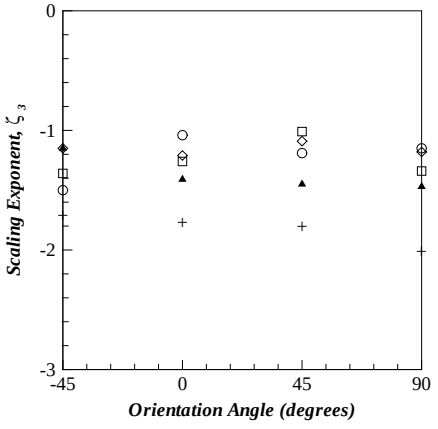

(f) $x = 4.0\ m$

Figure 4.29: The scaling exponent in the inertial-convective range of the three-point correlation of the fluctuating scalar field calculated using a collinear geometric configuration. Data shown for $Re = 5000$, $D = 4.7\ mm$ (○); $Re = 10000$, $D = 4.7\ mm$ (□); $Re = 20000$, $D = 4.7\ mm$ (◊); $Re = 10000$, $D = 2.2\ mm$ (+); and $Re = 10000$, $D = 9.4\ mm$ (▲) at the indicated distances downstream from the point release.

CHAPTER V

CONCLUSIONS

The current study analyzed two- and three-point correlation functions for a passive scalar field in a turbulent shear flow. The field corresponds to the plume downstream of a point release in a fully developed open channel turbulent boundary layer. Instantaneous images of the fluctuating scalar field were previously collected by Dasi (2004). In the current study, the data was analyzed by measuring the concentration fluctuations of several multi-point configurations. Statistical averages are calculated by ensemble-averaging over the length of the record and also by spatially-averaging over a region of the field in which the mean concentration gradient is constant. The two-point correlations of the fluctuating scalar field were calculated in the streamwise and wall-normal directions to estimate the integral length scale in each direction. Contours of the two-point correlations of the fluctuating scalar field were analyzed to determine the behavior of the scalar field in the plane parallel to the mean velocity gradient. Three-point configurations were examined to determine the scaling exponent properties and to extract geometric relationships of the scalar filaments. The three-point configuration of Mydlarski & Warhaft (1998) employs two measurement points separated in the streamwise direction and one measurement point separated in the wall-normal direction. The three-point configurations based on the shape function include an isosceles and collinear geometry. These configurations are rotated, translated, and dilated to investigate the influence on the orientation angle and the distance between the measurement points.

5.1 Two-Point Correlations of the Concentration Fluctuations

The two-point correlation function was analyzed to evaluate the current data set, verify the calculation methods, and calculate the integral length scale. Experimental results associated with two-point statistics previously were reported by Tavoularis & Corrsin (1981). Their analysis provides a foundation to ensure that the current data set and calculation methods are consistent with previous results. Close to the point release, the two-point correlation function in the streamwise direction is greater than the correlation function in the wall-normal direction. A similar trend was reported by Tavoularis & Corrsin (1981). In an isotropic scalar field, the two-point correlation function in each direction would be equal. The current results indicate that the streamwise-aligned and wall-normal-aligned two-point correlation functions become approximately equal as the scalar field evolves downstream, which suggests isotropic behavior. This trend is observed for each Reynolds number and each injection length scale.

In contrast, the two-point correlation contours illustrate the anisotropic conditions that persist to the smallest scales. The two-point correlation contours contain more details about the fluctuating scalar field because the contours provide information throughout the entire $x - y$ plane (i.e. the analysis is not restricted to a specific direction). In an isotropic scalar field, the two-point correlation contours would be symmetric, concentric circles. Tavoularis & Corrsin (1981) reported that the contours develop a tilted, asymmetric elliptical shape as a result of the mean velocity shear. The two-point correlation contours in the current study also exhibit the tilted, asymmetric elliptical shape. This characteristic contour shape develops for each Reynolds number and each injection length scale. Therefore, the current study agrees with the experimental results presented by Tavoularis & Corrsin (1981) and illustrates the inherent anisotropic behavior of the scalar field.

The current study also employed the two-point correlation function to calculate the integral length scale. The integral length scale describes the separation distance beyond which the autocorrelation of the concentration fluctuations is poor. The integral length scale provides a characteristic size of the scalar filaments because samples collected from

within the same filament would be well-correlated. The two-point correlation functions are calculated for the streamwise and wall-normal directions. As a result, an integral length scale is calculated for each direction. Close to the point release, the integral length scale in the streamwise direction is greater than the integral length scale in the wall-normal direction. At intermediate downstream distances, the integral length scale associated with the streamwise and wall-normal directions approach equivalent values. At these downstream distances, the integral length scale is independent of the Reynolds number, but dependent on the injection length scale. As the scalar field evolves further downstream, the integral length scale associated with each direction begins to increase. The integral length scale is used for subsequent three-point correlation calculations.

5.2 Three-Point Correlations of the Concentration Fluctuations

5.2.1 Configuration of Mydlarski & Warhaft (1998)

The three-point correlation function is calculated using the spatial configuration developed by Mydlarski & Warhaft (1998). The appropriate wall-normal separation distance, Y, associated with this geometry was selected based on the integral length scale, l_L, such that $Y/l_L \simeq 0.05$ (Mydlarski & Warhaft (1998) report data for $Y/l_L \simeq 0.043$, 0.051, and 0.13). The results of the current analysis indicate that the contours of the three-point correlation function are indeed symmetric. The symmetry associated with well-correlated points is represented by concentric, circular contours, which suggests universal behavior of the fluctuating scalar field for these points. The outermost contours maintain symmetric properties but evolve into a concave-sided hexagonal shape that resembles the characteristic V-shape reported by Mydlarski & Warhaft (1998). Therefore, the current results corroborate the symmetric observations reported by Mydlarski & Warhaft (1998). However, they reported that the correlation function should be zero when the three points form an equilateral triangle. This condition is an artifact of the imposed symmetry required to derive the three-point correlation function based on the structure function (equation 4.1). Mydlarski & Warhaft (1998) calculated the structure function as a surrogate for the correlation function because

of concerns regarding measurement drift. Another difference is that the scalar field in the current study is more intermittent than the temperature field analyzed by Mydlarski & Warhaft (1998). Further, Dasi (2004) reported that the scalar skewness associated with the data in the current study is not zero; whereas, the probability density function of the temperature fluctuations was symmetric for Mydlarski & Warhaft (1998) and the skewness was zero in that case. The effects of scalar skewness and intermittency also may explain the "less distinct" V-shape pattern observed in the current study.

5.2.2 Configuration Based on the Shape Function

Celani & Vergassola (2001) reported that the three-point correlation function depends on the size, shape, and orientation of the triangle defined by the three points. Accordingly, the three-point correlation function takes the following form:

$$C_3 = R^{\zeta_3} f(\chi, w) cos\varphi + \text{subdominant higher order terms} \tag{5.4}$$

where R is the global size variable, $f(\chi, w)$ represents the affects of different triangular shapes, φ describes the orientation of the triangle with respect to the mean scalar gradient and ζ_3 is the scaling exponent. The shape factor is defined such that its value remains constant as a specific configuration is rotated, translated, and dilated throughout the measurement region. The current study analyzes isosceles and collinear configurations. The effects of the size and orientation of the three-point template can be evaluated because the shape factor remains constant for a specified geometric configuration. In the inertial-convective range, the orientation angle affects the value of the correlation function for the collinear configuration, but does not affect the value associated with the isosceles configuration. For both configurations, the value of the scaling exponent appears independent of the orientation angle for downstream distances greater than $x = 0.1\ m$ (i.e. when the scalar field is no longer dominated by the tracer injection method). The scaling exponent appears to be independent of the Reynolds number and dependent on the injection length scale at intermediate downstream distances.

5.3 Future Directions

The current study provides a starting point to analyze the passive scalar field using multipoint correlators in a turbulent boundary layer. Although similarities exist between this study (shear flow) and previous research (non-shear flow), additional work is required to explain the subtle differences. Additional studies evaluating the effects of intermittency may explain the behavior of the characteristic V-shape pattern of the contours of the correlation function. The effects of scalar skewness are inherently included in the three-point correlation function of the current study. The ability to extract the effects of scalar skewness from the three-point correlation function provides a method to evaluate the dependency of the contour shape on the scalar skewness. Additional analyses related to the size, shape, and orientation of the three-point geometry will also be beneficial. These insights can be obtained by simultaneously analyzing the effects of several orientation angles in the presence of a constant shape function. This provides the ability to derive a relationship between the orientation angle and the value of the correlation function. Additional insights can be determined by evaluating the effects of various shape parameters, which can significantly affect the value of the three-point correlation function.

Bibliography

Anselmet, F., Y. Gagne, E. J. Hopfinger, and R. A. Antonia (1984). High-order velocity structure functions in turbulent shear flows. *Journal of Fluid Mechanics 140*, 63–89.

Batchelor, G. K. (1959). Small-scale variation of convected quantities like temperature in turbulent fluid. 1. general discussion and the case of small conductivity. *Journal of Fluid Mechanics 5*(1), 113–133.

Celani, A. and M. Vergassola (2001). Statistical geometry in scalar turbulence. *Physical Review Letters 86*(3), 424–427.

Coles, D. (1956). The law of the wake in the turbulent boundary layer. *Journal of Fluid Mechanics 1*(2), 191–226.

Corrsin, S. (1951). On the spectrum of isotropic temperature fluctuations in an isotropic turbulence. *Journal of Applied Physics 22*(4), 469–473.

Dasi, L. P. (2004). *The small-scale structure of passive scalar mixing in turbulent boundary layers*. Ph. D. thesis, Georgia Institute of Technology.

Holzer, M. and E. D. Siggia (1994). Turbulent mixing of a passive scalar. *Physics of Fluids 6*(5), 1820–1837.

Kolmogorov, A. N. (1941). The local structure of turbulence in incompressible viscous fluid for very large reynolds numbers. *Dokl. Akad. Nauk. SSSR 30*, 299–303.

Kolmogorov, A. N. (1962). A refinement of previous hypotheses concerning the local structure of turbulence in a viscous incompressible fluid at high reynolds number. *Journal of Fluid Mechanics 13*, 82–85.

Kraichnan, R. H. (1968). Small-scale structure of a scalar field convected by turbulence. *Physics of Fluids 11*(5), 945–953.

Kundu, P. K. and I. M. Cohen (2004). *Fluid Mechanics* (Third ed.). San Diego, California: Elsevier Academic Press.

Munson, B. R., D. F. Young, and T. H. Okiishi (1998). *Fundamentals of Fluid Mechanics* (Third ed.). New York, New York: John Wiley & Sons, Inc.

Mydlarski, L., A. Pumir, B. I. Shraiman, E. D. Siggia, and Z. Warhaft (1998). Structures and multipoint correlators for turbulent advection: predictions and experiments. *Physical Review Letters 81*(20), 4373–4376.

Mydlarski, L. and Z. Warhaft (1998). Three-point statistics and the anisotropy of a turbulent passive scalar. *Physics of Fluids 10*(11), 2885–2894.

Obukhov, A. M. (1949). Structure of the temperature field in turbulent flows. *Isv. Geogr. Geophys. Ser 13*(1), 58–69.

Obukhov, A. M. (1962). Some specific features of atmospheric turbulence. *Journal of Fluid Mechanics 13*, 77–81.

Pope, S. B. (2000). *Turbulent Flows*. Cambridge, United Kingdom: Cambridge University Press.

Rahman, S. (2002). *Effect of bed roughness on scalar mixing in turbulent boundary layers*. Ph. D. thesis, Georgia Institute of Technology.

Rahman, S. and D. R. Webster (2005). The effect of bed roughness on scalar fluctuations in turbulent boundary layers. *Experiments in Fluids 38*, 372–384.

Reynolds, O. (1883). An experimental investigation of the circumstances which determine whether the motion of water shall be direct or sinuous, and of the law of resistance in parallel channels. *Proceedings of the Royal Society of London 35*, 84–99.

Richardson, L. F. (1922). *Weather prediction by numerical process.* London: Cambridge University Press.

Roberts, P. and D. Webster (2002). Turbulent diffusion. *Environmental fluid mechanics - Theories and application*, edited by H. Shen, A. Cheng, K.–H. Wang, M.H. Teng, and C. Liu, ASCE Press, Reston, Virginia.

Shraiman, B. I. and E. D. Siggia (1995). Anomalous scaling of a passive scalar in turbulent flow. *C. R. Acad. Sci. Paris, Serie II b 321*, 279–284.

Shraiman, B. I. and E. D. Siggia (1996a). High rayleigh number convection and passive scalar mixing. *Physica D 97*, 286–290.

Shraiman, B. I. and E. D. Siggia (1996b). Symmetry and scaling of turbulent mixing. *Physical Review Letters 77*(12), 2463–2466.

Shraiman, B. I. and E. D. Siggia (2000). Scalar turbulence. *Nature 405*(6787), 639–646.

Sreenivasan, K. R., R. A. Antonia, and D. Britz (1979). Local isotropy and large structures in a heated turbulent jet. *Journal of Fluid Mechanics 94*, 745–775.

Tavoularis, S. and S. Corrsin (1981). Experiments in nearly homogeneous turbulent shear flow with a uniform mean temperature gradient. Part 1. *Journal of Fluid Mechanics 104*, 311–347.

Warhaft, Z. (2000). Passive scalars in turbulent flows. *Annual Review of Fluid Mechanics 32*, 203–240.

Webster, D. R., S. Rahman, and L. P. Dasi (2003). Laser-induced fluorescence measurements of a turbulent plume. *Journal of Engineering Mechanics 129*(10), 1130–1137.